UNIVERSITÀ DEGLI STUDI DI PADOVA

DIPARTIMENTO DI INGEGNERIA INDUSTRIALE

TESI DI LAUREA MAGISTRALE IN INGEGNERIA DEI MATERIALI

RESEARCH ABOUT PRESSURELESS SINTERING OF MILLED POWDER ZrB$_2$ BASED CERAMIC WITH CARBON

Relatore: Dott. Paolo Colombo
Correlatore: Dott. Angel Luis Ortiz Seco

Laureando: CRISTIAN MURRU

ANNO ACCADEMICO 2011 – 2012

To my family.

ABSTRACT

This study was about Zirconium diboride powders with a 2 wt% of graphite, the mixture was grounded at different time in Argon atmosphere, with high energy ball milling. The as-purchased powder was milled from micrometer size, until nanoparticles. Then were product specimens with uniaxial press and after with isostatic press. The green bodies were sintered without external pressure at different temperatures, from 1800°C until 2100°C. The effects of initial particle size and carbon on densification, microstructure were investigated. Submicrometer porous agglomerates contain nanometre-sized single crystals and nanopores were obtained after hebm. Even if the operating conditions were not totally developed in controlled atmosphere, so there were problem of oxidation due to high reactivity of nanoparticles. Graphite is an effective process control agent for the milling of ZrB2 because promotes the formation of finer particles (i.e. 50 vs. 120 nm) and evens out the average size of agglomerates (i.e., 122 vs. 143 nm). It is a PCA of sintering of ZrB_2 too, because does not alter the structure and at this concentration does not form new phases. Besides graphite removes the oxides present in the specimens, to promote with vacuum, the sintering at lower temperature. Relative density increased from ~71% for not milled powders at 1800°C, to 98% for 180 minutes milled powders at 2100°C.

INDEX

INTRODUCTION

Advanced ceramic materials play a key role in the progress of many fields of modern technologies, such as communication and information technology, energy and environmental technology, transportation and production technology, as well as the life sciences. Based on unique dielectric, ferroelectric, piezoelectric, pyroelectric, ferromagnetic, magnetoresistive, ionical, electronical, superconducting, and electro-optical properties, functional ceramics have found a wide range of applications.

An increasing demand for engineering ceramic materials that are tougher, stronger, and more reliable compared to the current industrial ceramic materials has driven the interest in ceramic composites for high-performance brake systems, light-weight spacecraft structures operating at temperatures up to 1600 °C, thermal barrier coatings for gas turbine components, high temperature oxidation and thermal shock resistant cellular ceramics for exhaust particle filters, as well as low emission porous burner systems, are examples of current product development activities in the automobile, spacecraft, energy, and environmental industries [18].

Ultra-high temperature ceramics (UHTCs) are a family of compounds which are chemically and physically stable at high temperatures and in oxidation atmospheres. UHTCs with melting temperatures in excess of 3000 K are usually made up of the refractory borides, carbides, nitrides and oxides of early transition metals [15], [27].

Structural materials for use in high-temperature oxidizing environments are presently limited to SiC, Si_3N_4, oxide ceramics, and composites of these materials. Silicon-based ceramics are oxidation resistant up to ~1600 °C, due to the formation of a protective SiO_2 surface film. Although SiO_2 is an excellent oxidation barrier at temperatures below 1600 °C, and above this temperature it begins to soften dramatically and develops substantial vapour pressure. Therefore, the use temperature of the silicon-based ceramics is limited to 1600 °C by their thermal stability in an oxidizing atmosphere. In addition, there are a relatively few refractory oxides that are stable in an oxidizing environment at or above 2000 °C. Among these oxides, zirconia (ZrO_2) and hafnia (HfO_2) typically have the highest melting points, ~2700 °C and ~2800 °C, respectively. Although they are inert chemically, they appear to remain susceptible to thermal shock, and exhibit high creep rates and phase transition at higher temperatures. Therefore, the development of structural materials for use in oxidizing environments at temperatures above 1600 °C is of great engineering importance.

The objectives of the present study are to understand the effects of sintering additions on the densification of ZrB_2, to characterize the densification behaviour, and to understand the mechanism of enhanced densification, without the assistance of an external pressure. Thermodynamic considerations will be presented to understand the role of impurities and atmosphere on oxygen content.

Research at Unex

The Materials Specialist Group University of Extremadura (UEX GEMA) has acquired extensive experience in mechanical and microstructural characterization and processing of advanced ceramics since 1986. The Group's projects in many R & D competitive grant national, regional, Integrated Activities, ERDF, etc.. (totalling over 1.2 million Euros in the period 2003-2006), has brought multiple (around 60 in the period 2003-2006) scientific publications in prestigious international journals (Science, Acta Materialia, Materials Science Engineering, Journal of the American Ceramic Society, Journal of Materials Research, Journal of Applied Crystallography, etc..) and conference papers. Over the last years were created new laboratory tests, treatment, processing and characterization of materials available to the group. The significant improvement in scientific infrastructure and personnel that has accompanied this introduction, has expanded and diversified the group's activity, and increase their scientific and technical productivity. Today in addition to developing a number of lines of research are being conducted regularly consulting and analysis services for regional companies and public administrations.

The Specialized Group Materials UEX has four laboratories dedicated to research and School of Industrial Engineering:
- Mechanical testing laboratory with equipment available to mechanically characterize nanoscale materials from macroscale, both at room temperature to 1400°C.
- The laboratory processing and treatment of materials is equipped with everything needed for sample preparation from powder green, for the sintering of these samples with or without pressure, in different atmospheres, etc.., And the subsequent preparation of samples and sintered for characterization.
- In the materials synthesis laboratory are made suspensions or solutions, are analyzed starting powders and suspensions, and there are deposited by moulding robot.
- The microscopy and microstructural characterization laboratory is dedicated to characterize of materials by microscopy, gas adsorption porosimetry, elemental analysis and electrical measurements.

The research about manufacture of advanced ceramic materials consist in designing and processing of advanced ceramic materials (carbides, nitrides, oxides, etc.) for both structural and functional applications in the form of massive blocks or coatings, preparation of submicron and nanopowders by reactive milling synthesis or high energy, mass sintering with or without pressure at high temperatures and under controlled atmosphere and manufacture of sol-gel coatings.

Topics in literature

There are a few topics in literature about this theme; the reasons are the technological difficulties to produce this UHTC material. In fact the temperature parameter (typically greater than 2000°C) plays a fundamental role about the intrinsic sinterability of the compounds ($T_{sint} > 0,7T_m$). The difficult to control the microstructure is linked to the choice of the sintering agents, which allow obtaining compounds of high bulk density and controlled particle size. Generally, the additives to promote the densification are transition metals (Fe, Ni, Co, Cr, Pt, Pd from 1 to 5 wt %), those with impact modifier and reinforcing role in nature are composed of ceramic (SiC, TiB_2, B_4C, Si_3N_4). Its applications in different technological areas permitted the development of new research with these powders [21].

Thesis structure

The first chapter will give some hints about the general properties of nanopowders, guiding the conversation toward the ceramic materials.

In the second chapter will be addressed in a broad way, the characteristics of ZrB_2 and its composites, whereas above all the effect of a carbon as alloying and oxygen as an impurity.

The third chapter deals with the various existing production methods related to advanced ceramic materials, with the influence of various additives in different cases.

The fourth chapter describes the experimental method used for this study, equipment and materials used, the motivations of their choice, assessing the advantage and shortcomings, and propose development.

The results are reported in Chapter 5, which there are observations and data analysis.

In the last chapter there are present the conclusions of the study, considering the entire production cycle, from grinding to a first materials characterization.

Chapter 1

NANOSTRUCTURED CERAMIC MATERIALS

1.1 INTRODUCTION

The term nanotechnology refers to the set of methods and techniques that allow the manipulation of matter at atomic and molecular scale and whose target is to build materials and products with chemical and physic-mechanical quite peculiar. Nanotechnology is now one of the most active areas in the field of scientific research. Since the end of the XX century the number of publications in scientific journals and in conference proceedings is ongoing and unbroken growth.

They are an interdisciplinary thematic and extremely wide, whose applications range from the fields of materials science than chemistry, physics until arriving to biology and medicine.

The nanomaterials or nanostructure materials are solids consist of structural elements (particles, grains), with characteristic dimension, in at least one of three directions, of a few nanometres, generally from 1 to 100. Were classified according to various criteria date.

According to the scheme in figure 1.1, nanomaterials can be classified both as a function of the chemical composition and according to the shape of the constituents microstructural (crystallite and grain boundary regions). Based on the shape of crystallites, nanomaterials can be classified: layer-shape, rod-shape, equiaxed crystallites.

Based on their chemical composition, the crystallites are divided into four different families: the first consists of the nanomaterials in which the crystallites have the same chemical composition of the regions at grain boundaries, in the second those in which the crystallites are different between their chemical composition, in the third those where the composition differs from the zones of the crystallites at grain boundaries and finally, in the fourth, the materials for which the crystallites are immersed in a matrix of different nature.

Another effective and immediate classification, distinguishes nanomaterials based on their characteristics in four different size classes:

- dimensionless, 0-D (clusters and nanoparticles);
- One-dimensional, 1-D (nanotubes and metal nanowires);

- two-dimensional, 2-D (thin films);
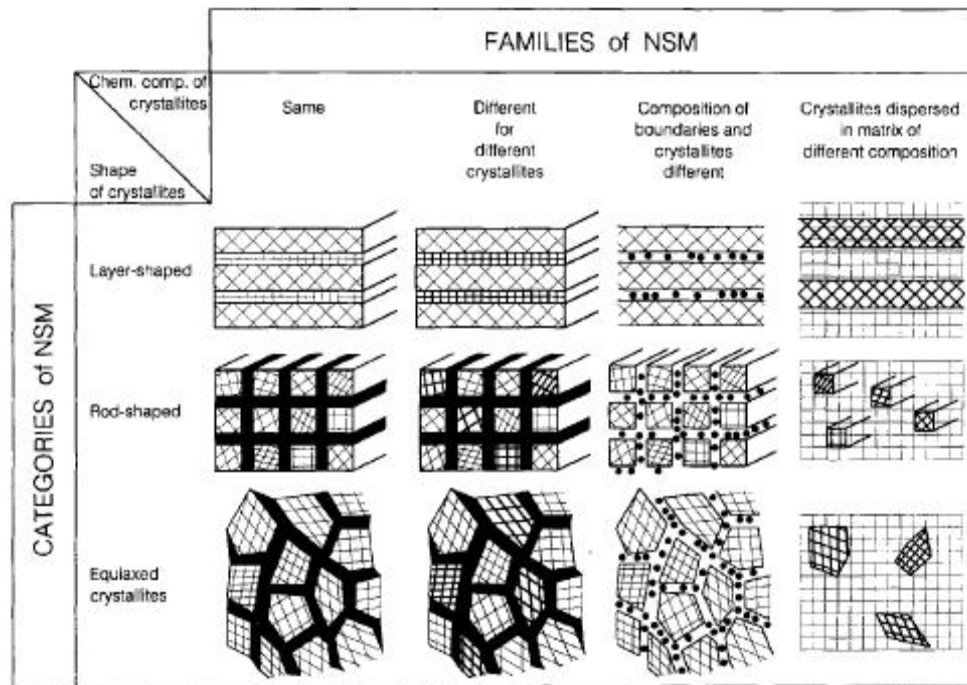- three-dimensional, 3-D (nanostructured materials consisting of nanoparticles as building blocks).

Fig. 1.1 Classification of nanomaterials as a function of the microstructural constituents morphology and of the chemical composition [24];

1.2   RESEARCH AND NANOSTRUCTURES

The nanostructured ceramic materials can be defined as ceramic materials in which at least one of the phase constituents is characterized by microstructural elements whose dimensions (in at least one of three directions) are of the order of nanometre.

Nanostructured ceramic materials can be classified into three main categories (Fig.1.2), based on the distribution, the type and number of phases present:
- nano type, in which there is a single phase of nanometre dimensions;
- type nano-nano in which there are two or more phases, all nanosized;
- type micro-nano, nanomaterials consist of a nanometre phase dispersed in a matrix micrometer (the phase nanometre can be distributed at grain boundaries or even inside the grains).
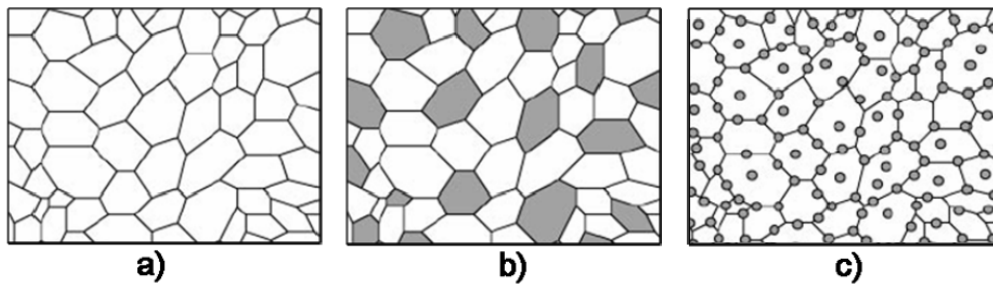
Fig. 1.2 Types of nanostructures: a) all nano of a single phase, b) all nano, two phases, c) micro-nano, the nanophase is dispersed inside the grains and along the grain boundaries;

As for nanomaterials in general, even for the ceramics specifically, the microstructure is significantly different from that of the corresponding micrometer. This is due to the large amount of atoms localized at the surface and along the grain boundaries zones. In figure 1.3 is shown a two-dimensional representation of a nano material, from which it is possible to understand what is the relationship between the atoms located inside the grain and those present at the board. As can be seen the two components, crystal and board, are comparable in terms of volume ratio. This makes that nanomaterials can be considered as heterogeneous materials, in which become predominant the surface properties compared to those of bulk.

The production of nanostructured ceramic materials involves a complete review of procedures and modalities of processing (synthesis, forming and sintering) than traditional ceramic materials. The characteristics of the raw materials, particularly the size of the particles of nanometre powders of departure, can be the basis of some problems, associated with their production.

The effect of the extremely small size and large surface area, in fact promotes, on the one hand, the processes of oxidation and the possibility of contamination of the powders and secondly, in a significant way, the formation of agglomerates in the powders (caused of an easy formation of bonds between particles of very small size, by virtue of their high reactivity). The formation of agglomerates in the powders is the main cause of low density in the final products obtained from nanoscale powders.
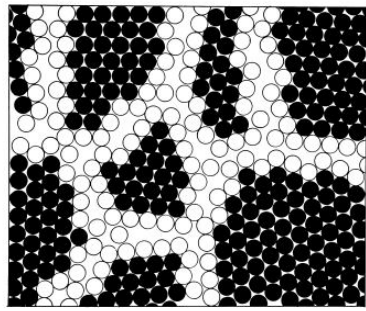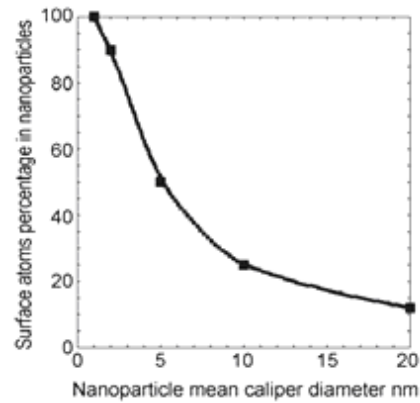
(a)	(b)

Fig. 1.3 (a) Two-dimensional representation of a nanomaterial. The atoms inside the grains are represented in black. Those areas of the grain boundary in white [8]; (b) Percentage of atoms to the surface in function of the average size of the nanoparticles;

1.3 MATERIAL PROPERTIES AT NANOSCALED SIZES

Numerous studies shown that the properties of the nanocrystalline ceramic materials are significantly different, and generally increased, compared with ceramic or conventional micrometre materials. This is due basically to two typical characteristics of nano materials:

- the occurrence of the quantum confinement effect size, that happen when the size of the microstructural elements that constitute a material become comparable with the same order of magnitude of some physical phenomena (i.e. with the average free paths of electrons and phonons);

- the wide distribution of atoms to the surface and along the grain boundaries, with the consequent presence of many unsatisfied valences and defective coordinations.

On the first point, the size of the structural elements that constitute a material is a key to decide its properties and its final characteristics. The effect of quantum confinement, typical of nanostructured materials, causes a noticeable change in the materials properties, especially the physical and optical properties. This depends on the correlation between the size factors with the variation of the electron energy levels that characterize a material.

More specifically, the continuity of the energy bands, typical of macroscopic solids, is changed by the manifestation of discrete energy levels (a phenomenon called quantization) when switch to nanosize; moreover the spaces between the energy levels grow with decreasing size, as illustrated in detail in figure 1.4
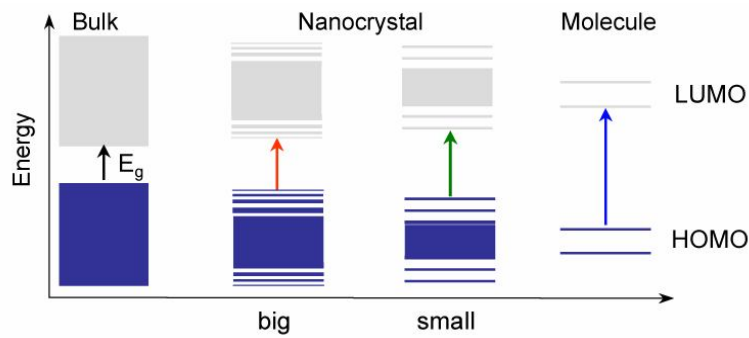
Figure 1.4 Schematic diagram about the quantization of energy levels, getting from a bulk solid to a nanocrystal and to a molecule;

This variation can be easily understood by reference to the model of the "particle in a box", which describes the behaviour of a free particle to move in a space surrounded by impenetrable barriers. When the space in which the particle is free to move, is significantly reduced, also the movement of the particle is strongly confined in that space. In this case the particle can occupy only a few definite positions.

For example, in a large sample of metallic material are present many electrons which, as the particles of a gas that fills a room, are free to move in any direction. Under these conditions a particle (electron) can take any value in energy. If the space of movement of the electrons (or particle) is significantly reduced, the wave nature of the electron starts to become determinant. In these conditions, according to the laws of quantum mechanics, the electron energy can only take on discrete values. Depending on whether the "box" of potential is limited in one, two or three dimensions.

Regarding the second point, nanomaterials are characterized by a high value of surface/volume ratio, which means that a large amount of the atoms is localized at the surface or along the grain boundaries, with the consequent presence of numerous unsatisfied valences. This ratio is inversely proportional to the size of the particle, then as a result, the surface area increases with decreasing particle size.

The significant presence of unsatisfied valences strongly influences the reactivity of nanomaterials. For example, this results in the ability to absorb more easily gas or in the diminution of the sintering temperatures, of at least 200 °C as the case of the alumina or again, in the great ease with which nanoparticles tend to create bonds together to form agglomerates.

It is estimated that a nanoparticle has about 90, 40 and 10% of atoms localized at the surface, if its size is respectively 1, 5 or 20 nm.

Summarizing the properties of nanoscale materials depend strongly on the following factors:

- quantum-mechanical effects;

- great amount of atoms localized at the surface and in grain boundary areas;

- presence of unsatisfied valences and sites available for chemical reactions;

- difference in behaviour between crystal and grain boundary.

Chapter 2

ZIRCONIUM DIBORIDE AND ITS COMPOSITES

2.1 INTRODUCTION ABOUT UHTC

Ultra-High-Temperature Ceramics (UHTCs) can be defined as ceramic materials with melting points ~3000°C. Compounds considered UHTCs include ZrB_2, ZrC, HfB_2, HfC, and TaC. Because of their high melting points, oxidation resistance, and chemical attack resistance, UHTCs have been investigated for applications that include thermal protection materials for advanced re-entry vehicles, molten-metal crucibles, and high-temperature electrodes. The strong covalent bonding in non-oxide UHTCs gives them high melting temperatures, but makes them difficult to densify. The densification of pure ZrB_2 is complicated by two characteristics of this compound, similar to other transition metal borides: the high melting point and the comparatively high vapour pressure of the constituents. As a result, UHTCs are usually consolidated by hot pressing at temperatures higher than 1900 °C. As for TiB_2 materials, the introduction of sintering aids like Fe, Ni, Co, W, C, and WC improves the final density and allows lowering the densification temperature [28]. The impurities concentrate in the grain boundaries and decrease the high-temperature strength. Alternative processing routes, such as reactive hot pressing, self-propagating high-temperature synthesis, and polymer precursors have been investigated to improve the purity and densification behaviour of UHTCs. From the larger family of UHTCs, refractory metal diborides have been identified as candidates for ultra-high-temperature aerospace applications. In particular, ZrB_2-based ceramics have been investigated because of a unique combination of thermal shock resistance, strength at high temperature, and low density [27].

2.2 ZrB₂ AND ITS COMPOSITES

Zirconium diboride is an important member of UHTCs family. The highly covalent nature of ZrB_2 leads to a high melting temperature (3250°C), high Vickers' hardness (23 GPa), and a high four-point flexural strength (565 MPa) [7].
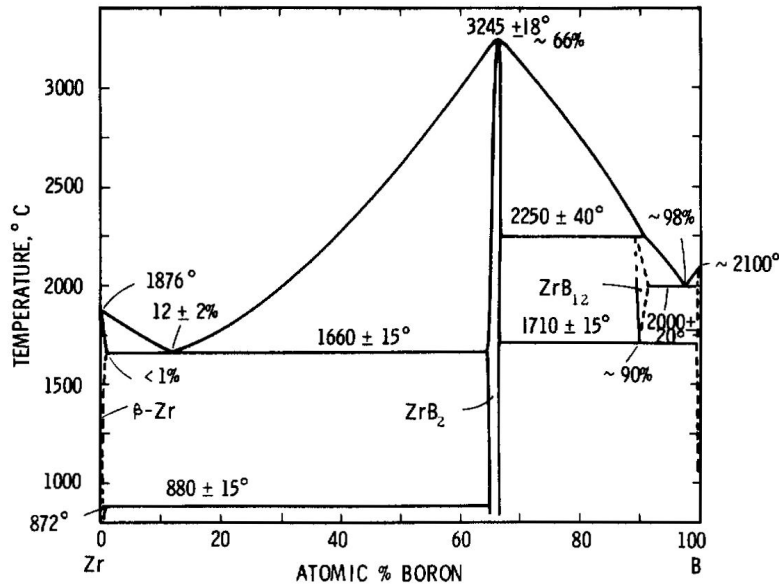
Fig. 2.1 Zirconium diboride phase diagram. It melts congruently at 3245°C at the stoichiometric composition;

Young's modulus can be described by a mixture rule and it decreased with porosity. Fracture toughness displayed in the ZrB_2-based composites is in the range of 2–6 MPa m$^{1/2}$.

Since the discovery of superconductivity at Tc = 39 K in MgB_2, the physical properties of the group IV transition metal diborides with simple hexagonal AlB_2-type structure have attracted significant interest. The crystal structure of ZrB_2 is designated as AlB_2-type transition metal diborides with the space group symmetry P6/mmm. It is simply a hexagonal lattice in which close packed TM (transition metal) layers are present alternative with graphite-like B layers. Choosing appropriate primitive lattice vectors, the atoms are positioned at TM (0,0,0), B (1/3, 2/3, 1/2), in the unit cell. It is noted that the most stable structure of the ZrB_2 corresponds to the axial ratio c/a = 1.120, where a = 3.1768 Å, c = 3.5590 Å [13].

12

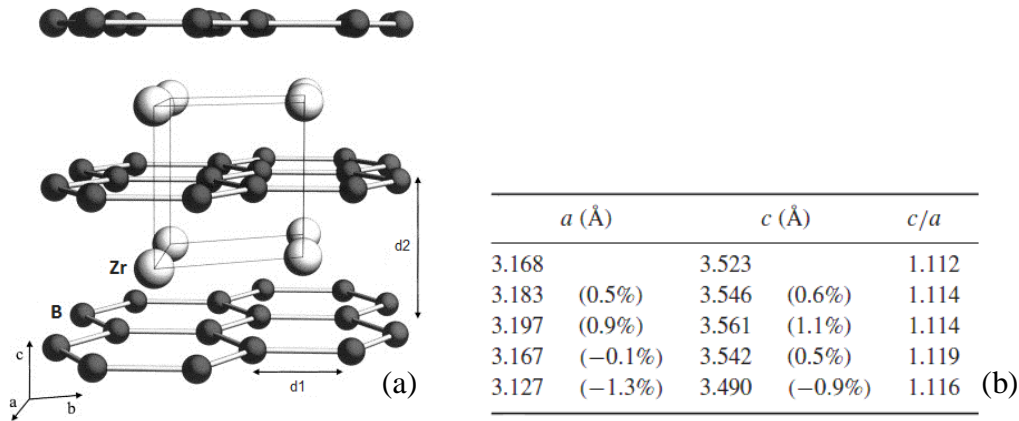| a (Å)		c (Å)		c/a
3.168		3.523		1.112
3.183	(0.5%)	3.546	(0.6%)	1.114
3.197	(0.9%)	3.561	(1.1%)	1.114
3.167	(−0.1%)	3.542	(0.5%)	1.119
3.127	(−1.3%)	3.490	(−0.9%)	1.116

(a)   (b)

Fig. 2.2 Crystal structure of ZrB_2 (a), with different lattice parameters measured (b) [6];

The XPS spectra for B $1s$ and Zr $3d$ core-levels of ZrB_2 are shown in figure 2.3. The B $1s$ spectrum is a single peak at a binding energy of 187.81 eV, very similar to that of MgB_2 (187.82eV). The Zr $3d$ levels consist of the spin-orbit split $3d5/2$ and $3d3/2$ in the correct intensity ratio (3:2) and are also single asymmetric peaks at a binding energy of 178.89 and 181.30 eV, respectively.

(a)

(b)
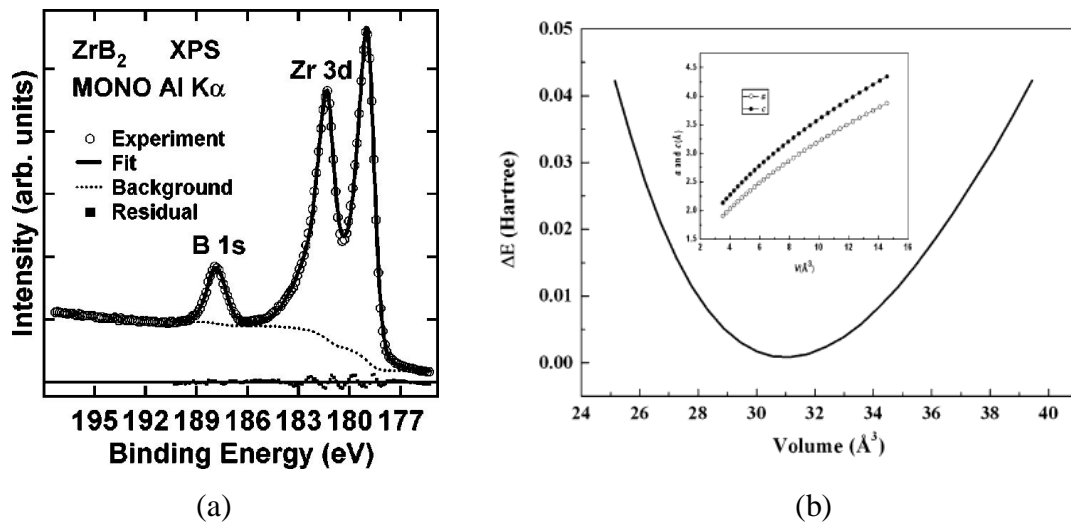
Fig. 2.3 (a) The Boron $1s$ and Zr $3d_{3/2}$ and $3d_{5/2}$ core-levels in ZrB_2 obtained using a monochromatic Al Ka source (hn51486.6 eV) [10]; (b) The energy $\Delta E(=E-E_0)$ as a function of the primitive cell volume of ZrB_2. The solid curve is the resulting fit of the Murnaghan equation of state. Inset c/a ratio versus V;

For each volume, was determined the corresponding equilibrium ratio *c/a* of ZrB_2 by performing total energy calculations on a series of different *c/a* ratios and minimize the energy as function of *c/a*.

Through these calculations, it could obtain the equilibrium parameters a and c and the corresponding equilibrium ratio c/a of ZrB_2 under arbitrary pressures. The calculated values of ΔE (=$E-E_0$, E_0 = minimum energy) have been plotted as a function of volume in figure 2.3 (b). It was plotted ratios a/a_0, c/c_0, and V/V_0, vary with pressure in figure 2.4 [13]
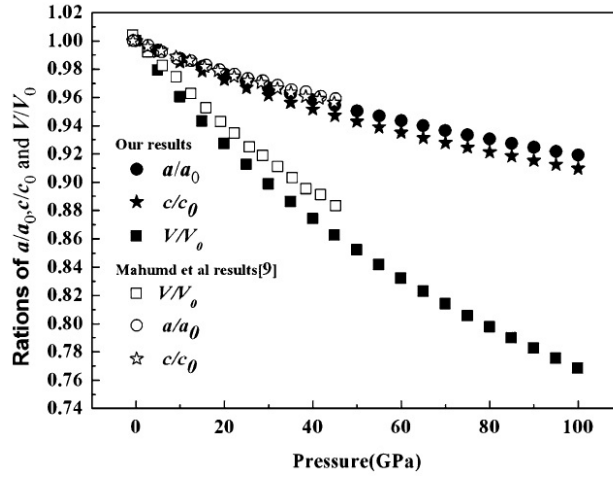
Fig. 2.4 The normalized volume V/V_0, a/a_0, and c/c_0 as a function of pressure at T = 0 °C where the dark rectangles, circles, and asterisks represent Hongzhi Fu results [13] obtained V/V_0, a/a_0, and c/c_0, respectively, and the blank ones are the results reported to compare;

Although it is possible to determine the cell parameters, with different methods, the theoretical density of the material obviously depends on the way in which the atoms or ions occupy the available space and by the involved atoms/ions weight. Therefore, knowing the structure type of crystal structure, the cell parameters (or atomics/ionics radii) and the weights in play, the density is derived from the relationship (2.1);

$$\rho = \frac{n' \, (\Sigma A_C + \Sigma A_A)}{V_C N_A} \qquad (2.1)$$

with n' = number of formula units within the unit cell;

ΣA_C = sum of the atomic weight of all cations in the formula unit;

ΣA_A = sum of the atomic weight of the anions in the formula unit;

V_C = unit cell volume;

N_A = Avogadro's number, 6,023 x 10^{23} formula units/mol.

Applications

Other ceramics based on the transition metal borides, nitrides, and carbides have extremely high melting points (>2500 °C) and are referred to as ultra-high temperature ceramics. Within the family of transition metal ultra-high temperature ceramics, diborides such as ZrB_2 and HfB_2 have unique combinations of mechanical and physical properties, including high melting points (>3000 °C), high thermal and electrical conductivities, chemical inertness against molten metals, and great thermal shock resistance. Thus, although carbides typically have the highest melting points (>3500 °C), the diborides ZrB_2 and HfB_2 are more attractive candidates for high-temperature thermomechanical structural applications at a temperature ≥2000 °C [4].

Based on its corrosion resistance and a high wetting angle in contact with molten metals, ZrB_2 has been used for molten metal crucibles, Hall–Heroult cell cathodes, submerged nozzles in continuous steel casting, and plasma-arc electrodes. Zirconium diboride is also resistant to thermal shock and oxidation, which makes it a candidate for thermal protection systems, leading edges, and propulsion systems in future hypersonic flight vehicles and reusable launch vehicles [7]. In particular, ZrB_2 has the lowest theoretical density among the ultra-high temperature ceramics, which makes it an attractive material for aerospace applications [4].

Traditional applications of such materials are based on their interesting combination of mechanical and transport properties: high melting temperature, high stiffness, and hardness, high thermal and electrical conductivity. The knowledge of such basic characteristics as stiffness and thermal expansion coefficient is obviously important for applications of ZrB_2 as a refractory material, either on its own or as a matrix of a reinforced composite [13]. Zirconium diboride is thought to have a low intrinsic sinterability due to its strong covalent bonds, low bulk and grain boundary diffusivities, and the presence of surface oxide impurities [16].

The composite approach has been successfully adopted in order to improve the densification, mechanical properties, physical properties, as well as the oxidation and ablation resistance of the ZrB_2 ceramics. For example, the addition of 20 vol% fine SiC (d ≈ 0.5 μm) increased the strength of ZrB_2 to over 1 GPa. The ZrB_2–$MoSi_2$ composites consolidated by spark plasma sintering (SPS) can retain their room temperature strength (~650 MPa) to at least 1200 °C. The addition of $ZrSi_2$ reduced the densification temperature of ZrB_2 to below 1550 °C, as well as increasing its thermal and electrical conductivities [17]. Obviously, the mechanical and physical properties of the ZrB_2-based composites are closely linked with the densification process, compositions, starting powder, microstructure, and intergranular second phase. Therefore, it is necessary to understand the relation of performance to processing, compositions, and microstructure in order to produce an ultra-high temperature ZrB_2-based composite with superior performance [4].

Tailoring the structure at the nano or even molecular level, however, can only be a successful approach to materials processing when the homogeneity and the structural information of the small volume element can be scaled up to a macroscopic component dimensions. The wide range of length scale of macro, micro, and even nanoscale dimensions, extending over 8-10 orders of magnitude (from nm to m), however, is a great challenge in order to establish effective and affordable multiscale processing and manufacturing technologies. Hence, there is a great need for the development of corresponding multiscale modelling and simulation tools to support advanced multiscale materials and processing design [18].

2.3 INFLUENCE OF C ADDITIONS

The poor sinterability of ZrB_2 is due to its strong covalent bonding and low bulk and grain-boundary diffusivities which impose serious kinetic restrictions and the presence oxide impurities from the synthesis process (i.e., ZrO_2 and B_2O_3) that favour coarsening over densification. One of the approaches currently being used to promote solid-state pressureless sinterability of ZrB_2 is to add carbon to ball-milled ZrB_2 powders. The comminution via ball-milling refines the size of particles shortening the diffusion distance of the Zr and B species during sintering, whereas the carbon addition removes the undesirable surface oxides via the carbothermal reaction (2.2) [5].

$$ZrO_2 + B_2O_3(l) + 5C \rightarrow ZrB_2 + 5CO(g) \qquad (2.2)$$
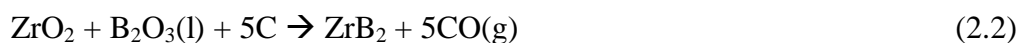
And the reaction (2.3) [5]

$$ZrO_2 + 3C \rightarrow ZrC + 2CO(g) \qquad (2.3)$$

if excess ZrO_2. The success of this combined approach become evident when one considers, for example, that the ball-milled ZrB_2 powder with particle sizes of ~0,5 μm reaches 100% density at 1900 °C with 2% carbon addition, whereas the as-received powder with particle sizes of ~2 μm and the same carbon amount only reaches 95% density [5] and the pure powder practically does not densify (i.e., densities of 61% and 68% for the as-received and ball-milled powders, respectively) [5]. Satisfactory results have been obtained by comminution via ball milling with subsequent addition of carbon, followed by sintering without pressure of ZrB_2 powders. It can be expected a

further improvement if the distribution of the carbon added is performed in a uniform manner as nanosized powders. Recently it was showed that high energy ball milling of pure ZrB_2 powder using shaker mills can produce submicrometer agglomerates of many cold welded nanoparticles. The High Energy Ball Milling is able to achieve a smaller particle size compared to the traditional ball-milling. This is because the high energy ball-milling generate stresses high enough to fracture fine particles, whereas conventional ball milling (e.g., operation with a low ball-to-powder ratio and a lower speed) cannot. The graphite has known lubricating properties that are exploited in the high energy ball milling process, when it is added to the powders. This generates two beneficial effects: first: as process control agent (PCA), limiting the cold welding among ZrB_2 nanoparticles and in the second place, especially if homogeneously distributed, as aid for the subsequent sintering. Nevertheless, had not yet proved in any studies that graphite was or not effective as PCA for the high Energy ball milling of ZrB_2 powder that are used to produce UHTCs. This was studied at University of Extremadura, in the department of mechanical, energetic and materials engineering of Badajoz [11].

Commercially available ZrB_2 (Grade B, H.C. Starck, Goslar, Germany) and graphite (Synthetic, Sigma-Aldrich, Madrid, Spain) powder were used as starting material. The as-purchased ZrB_2 powder has a purity of 99%, and consist of a single-crystal particles with an average size of 2-3 μm as indicate by the manufacturer and confirmed from the direct measurement by laser scattering (LS) and the absence of peak broadening in its X-ray diffraction (XRD) pattern. The corresponding values for the as-purchased powder are >99% and 5 μm. Two powder compositions were prepared, pure ZrB_2 and ZrB_2 + 2 wt% graphite. It has been chosen this percentage of carbon additive, with reference to a previous study [5] in which it was shown that the 2 wt % (i.e. a 5,12 vol%), was the optimal concentration for the pressureless sintering of ball milled ZrB_2 powders. This for tree reasons, first because the surface of undesired oxides are completely removed, second it prevents the grain coarsening during sintering and third, it will not have adverse effects on the hardness of the massive material due to the presence of Carbon-rich phase [5].

The high-energy ball milling of the pure ZrB_2 and ZrB_2 + 2 wt% graphite powders was performed using a shaker mill (Spex D8000, Spex CertiPrep, Metuchen, NJ) equipped with two cylindrical hardened steel containers under the following conditions: ball-to-powder weight ratio of 2, time in the range 3-180 minutes, room temperature.

The characterization of as-purchased and milled powders occurred using LS, XRD and Transmission Electron Microscope (TEM). The analysis with LS, used to determine particle size distribution, have been developed through red and blue light source (Mastersize 2000, Malvern Instruments, Worcestershire, UK), and were conducted in quintuplicate.

XRD was used to evaluate the average crystallite size and crystal lattice microstrain. The calculations were carried out by applying the variance method to the 101 peak of ZrB_2. Details of which has been reported elsewhere [11]. The XRD data were collected in step-scanning mode (range of 40°-43° 2θ step width 0.02° 2θ, and count time of 5s/step) with CuKα radiation (λ=1.54183 Å), using a laboratory diffractometer (Philips PW-1800, Eindhoven, the Netherlands). TEM was utilized to examine the particles morphology, and to validate the particles and crystallite sizes measured by LS and XRD, respectively. The observations were made at 200 kV in bright and dark field mode, using two conventional microscopes (Tecnai G2 20 Twin, FEI, Eindhoven, the Netherlands and JEM-2100, JEOL, Croissy-sur-Seine, France).

The LS, XRD, and TEM specimens were prepared using routine methods applicable to ceramics powders.
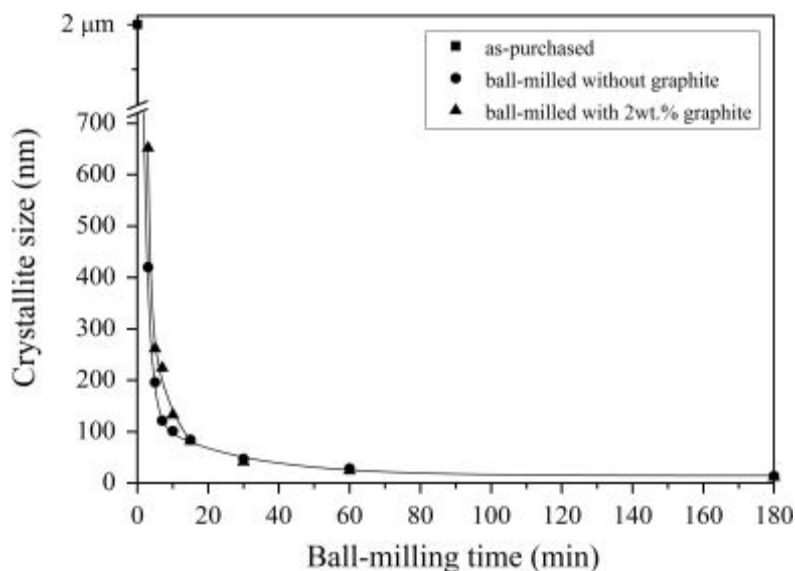
Fig 2.5 shows the evolution of the average crystallite size with ball-milling time for the ZrB_2 powders milled with and without graphite, determined from the peak broadening in the XRD patterns using the variance method [11].

It may be noted that both graphs have a general trend qualitatively similar, in that it has a rapid reduction of the crystal size, than more gradually passes to ~13nm after 180 minutes of ball milling. The final measurement may be the limiting crystallite size, which would be mainly determined by the comparable fracture strength of nano-ZrB_2 particles with the stresses created by the ball milling conditions applied. It is also noted that with graphite the crystallite size refinement is slower in the early stage of ball milling, with the formation of nanocrystallites (i.e., smaller than 100 nm) occurring approximately 1.5 times later (~15 vs. 10 min). The graphite addition however, did not

18

alter the kinetics of crystallite size refinement in the late stages of ball milling, because the two curves converge at ~15 minutes in a crystallite size of ~85 nm, and from then onwards the nanocrystallites have the same size within experimental error. Moreover these nanocrystallites are in both cases free of lattice microstrains and have the same lattice parameters as in the as-received condition (a=3.167 Å and c=3.524 Å). This was interfered from the analytical modelling of the XRD peaks by Voigt functions, which revealed that there is neither Gaussian peak broadening, nor peak shifting. These results show that a crystallite size refinement occurs, independently of the presence or absence of graphite, by brittle fracture, and therefore lattice microstrains, which were not observed in the XRD analysis.

Figure 2.6 compares the average particle size of Zirconium Diboride powders milled with and without graphite as a function of the ball-milling time, measured using LS.
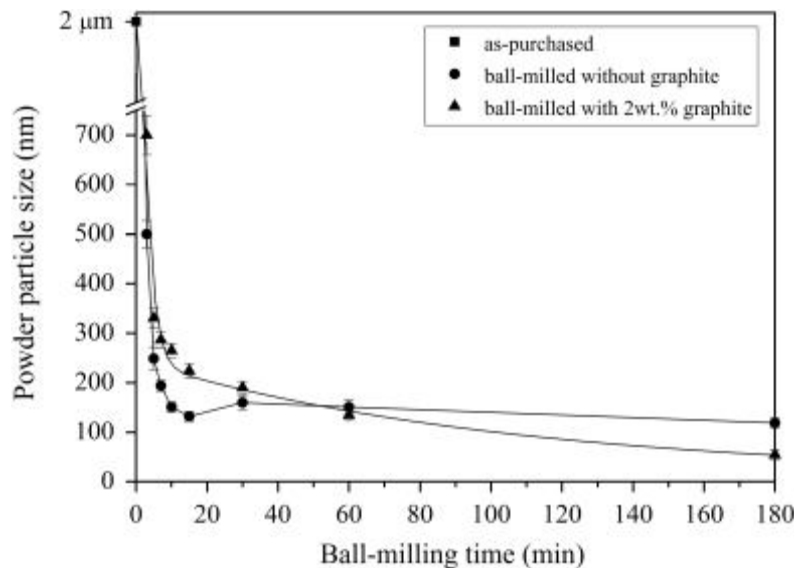
Fig. 2.6 Trend of the average particle size of ZrB_2 powder, respectively with and without graphite, in function of ball-milling time [11];

It is possible to obtain three interesting observations from this graph. In the case where there is not graphite, at the beginning there is a reduction of particle size, then gradually increases up to stabilize at sub micrometric dimensions close to the value of ~ 120 nm, while the graphite causes a different effect, obtaining a continuous reduction until the nanoscale (~ 50 nm). Second, the graphite leads to a decrease of the refinement speed in the initial phase of ball-milling, that take place with the formation of fine particles (with size less than 200 nm) at a time of ~ 30 rather than 7 minutes without graphite. Third, the powder particle sizes determined via LS are substantially greater than the crystallite sizes measured by XRD. Taken together, these results indicate that

during ball milling the ZrB_2 particles are repeatedly fractured and cold welded, and that the graphite addition minimizes this cold welding. Despite its brittleness, cold welding of ZrB_2 during ball milling is possible owing to the local temperature spike at the collision site (~300°-500°C) with the presence of high compressive stresses in a very short duration (of the order of 10^{-6} -10^{-7} s).

In both the case is possible confirm with TEM analysis, that cold welding occurs, but it shows to be less sever in the milled powder with graphite. In figure 2.7 could be seen that the particles of long term milled powder (180 minutes) are in fact agglomerates that contained finer particles, whose sizes (i.e., 5-15 nm) match the crystallite sizes determined by XRD.
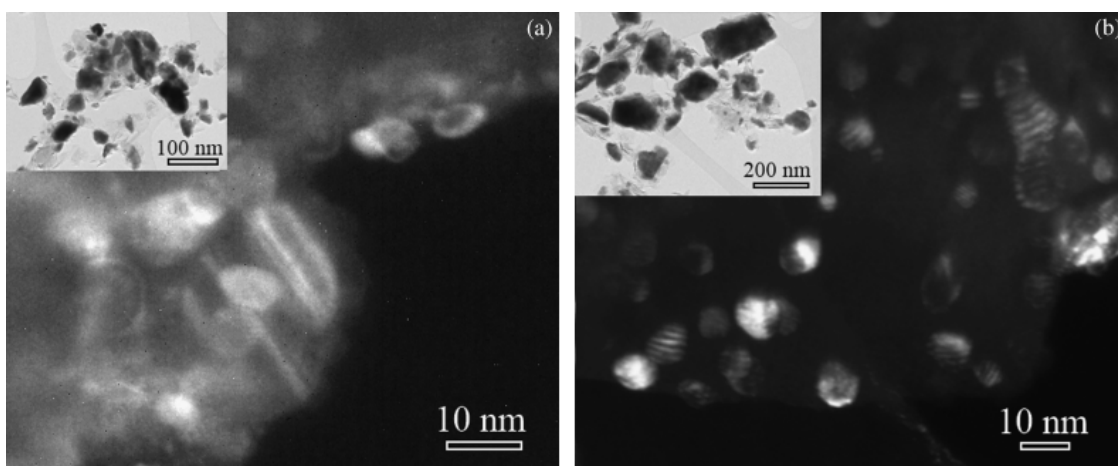
Fig. 2.7 Transmission electron microscopic dark-field image of the interior of zirconium diboride (ZrB_2) agglomerates ball-milled (a) with and (b) without graphite for 180 min. The inserts are low-magnification transmission electron microscopic bright-field images of the ZrB_2 powder particles [11];

Furthermore the TEM observations reveal that the agglomerates are smaller with graphite, which is consistent with the LS test. The addition of graphite promotes the formation of finer agglomerates and also uniforms their sizes. This conclusion was inferred during the extensive TEM observations and agree with the LS analysis results, that indicate a reduction from 143 to 122 nm if graphite is introduced in the ball milling (measured in term of the D_{90}-D_{10} difference), in the powders milled for 180 minutes [11].

An example of particles of pure ZrB2 powder and milled powder milled for long time could be seen in figure 2.8. One observes in figure 2.8 (a) that the particle size of the as-purchased powder (~2μm) was reduced to the sub-micrometer scale in less that 1 minute of high energy ball milling. The particles have faceted surfaces and some of those contain cracks.

After long-term HEBM (figure 2.8(b)) the morphology of the powder particles has evolved towards smooth-surfaced nano-particles (i.e., <20nm) that composed ultrafine (i.e., <200 nm) agglomerates. Also these last types of particles are crack-free.

Finally, the fact that these agglomerates are strong, because they have survived the ultrasonic bath, reveals the occurrence of cold-welding. Cold-welding during HEBM is a well-known phenomenon, and is typical but not exclusive of ductile compounds. Indeed, despite the brittleness of ZrB_2, cold-welding occurs for long HEBM times because particles behave in a more ductile fashion, and there is a local temperature spike at the collision site (~300÷500 °C) with the presence of high compressive stresses (~6 GPa) of very short duration (of the order of $10^{-6} \div 10^{-5}$ s) [8].
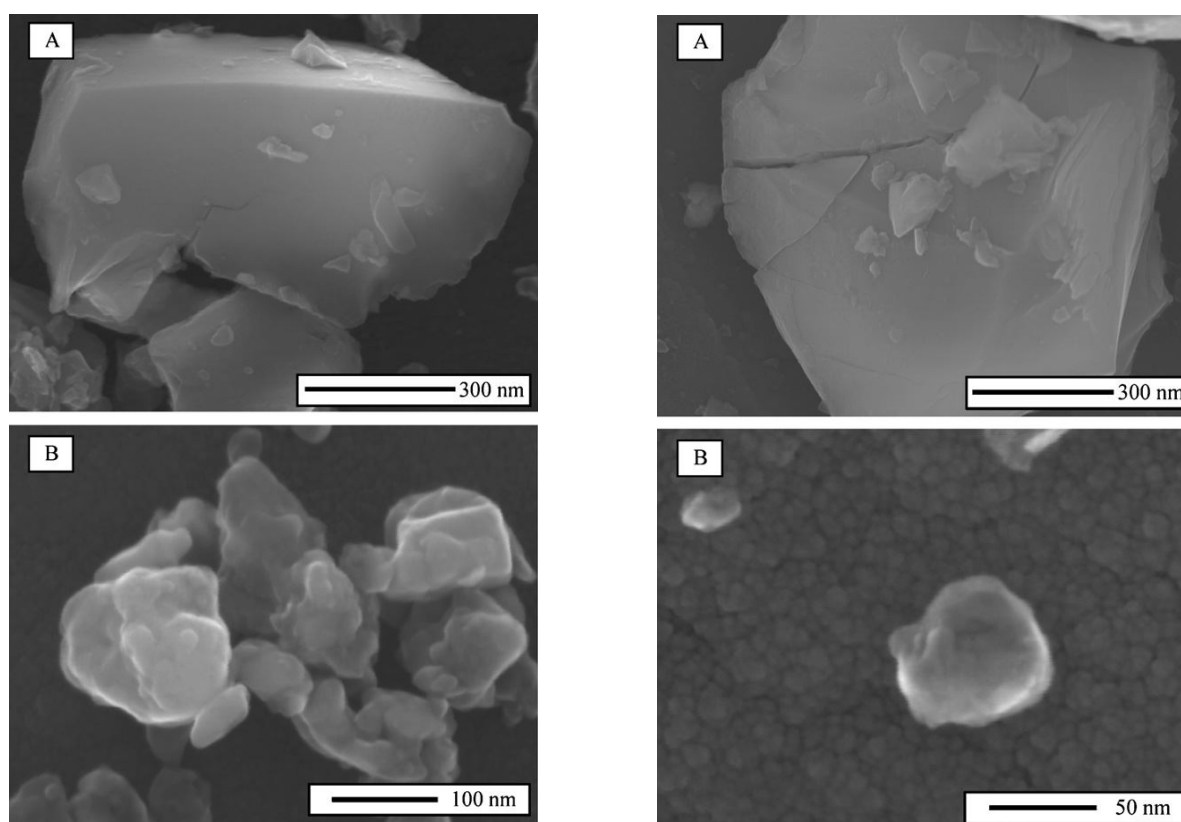
Fig. 2.8 FE-SEM images of the ZrB_2 powder particles after HEBM for (A) 1 min and (B) 180 min.;

The results presented above demonstrate that the ball milling with graphite addition, can reduce the range of the size distribution of ZrB_2 agglomerates, even if this also results in a slower refinement of agglomerates and primary particles. The experimental effect of graphite can be understood from its chemical inertness that reduces cold welding of the particles during ball milling. As a consequence, nanometre agglomerates are created, but without graphite, submicrometer agglomerates are formed instead. Graphite also possesses lubricating properties which could let the

fine agglomerates entrapped between two colliding balls to slide past each other, leading to the exposure of larger agglomerates to compression by the two colliding balls. Whatever the mechanism, the larger agglomerates continue to fracture until they reached a limited dimension.

It is well known that the compressive stress imparted to the solid in each collision, occur without laterals constraints during ball milling, and depends on the kinetics energy of the colliding balls and on the rigidity of the solid.

If the contact is lubricated and the particles or agglomerates can hence slide laterally with ease during collisions, only a little part of the collision energy is consumed in friction, and more to fracture them. How it was told, comminution becomes slower with the addiction of graphite. However graphite does not affect the ultimate size of the primary nanoparticles because this is mainly due to the fracture strength of ZrB_2 and the compressive stress at the collision site.

Based on these observations, two advantages are anticipated for the processing of ZrB_2 UHTCs.

First, it is well known that pore size in powder compacts is proportional with the agglomerate size in the powder. Thus the reduce agglomerate size (~50 nm) together with the still relative broad size distribution (~120 nm) of the ball milled ZrB_2 with graphite has the potential to improve the powder packing density and reduce the diffusion distance during sintering.

Second, ball milling can also mitigate the issue of dispersing the mixed graphite in the powder. The previous study of high energy ball milling [11] reveals that graphite does not dissolve in ZrB_2 to form solid solutions during ball milling, but is homogeneously dispersed at nanometre scales. Thus ball milling with graphite can reduce processing steps, for example the uniform dispersion of carbon, currently achieved by one additional processing of coating the individual powder particles with polymer resin [11].

It was found that carbon reacted with SiO_2 present on the surface of SiC before densification was initiated. Similar results were obtained for B_4C and TiB_2, where carbon facilitated densification by its reaction with surface oxides at elevated temperatures. Removal of the oxide impurities was essential to complete densification of these non-oxide ceramics. Oxide impurities promote rapid grain coarsening, which can lead to the formation of porosity trapped within grains and, therefore, limit the final densities. Previous studies have also discussed the effect of oxide impurities on sintering of ZrB_2 [7], [19]. Both B_4C and WC additions were found to promote removal of surface oxides from ZrB_2 and allow for pressureless sintering to near full density. Therefore, removal of surface oxides is critical for densification of ZrB_2 and other non-oxide ceramics. Because the oxide impurities are generally present as thin layers on particle surfaces, distribution of the sintering additive as a uniform coating on the surface of precursor powder particles may be more effective in

removing oxide impurities and promoting sintering of ZrB_2 as compared to the particle additions used in previous studies. [5]

2.4 OXIDATION OF ZrB_2

The idea of working in vacuum become subsequent to a study about oxidation of ZrB_2 milled particles. To produce massive Ultra High Temperature Ceramics from poorly sinterable powders such as those of ZrB_2, two of the key phases of processing to improve the sinterability at solid state, are the reduction of the fineness of the starting powders and the elimination of impurities oxide surface [1], [27],. The effect resulting from reduced particle size is to shorten the distance of the chemical species diffusion, significantly diminish the time required for densification. The phase of interparticle diffusion controlled sintering, is particularly relevant in ZrB_2, because of limitations in the kinetics due to strong covalent bond and a low self-diffusion coefficients [32]. It is not surprising therefore that the typical micrometer-sized ZrB_2 particles need to be refined to the submicrometer range before the sintering heat-treatment. In comparison of the surface oxide impurities in non-oxide ceramics, they are known to favour the evaporation–condensation mass transport mechanism, and this promotes coarsening thus reducing the driving force for densification and limiting the final density [7]. Hence, it is necessary to remove the surface oxides of ZrO_2 and B_2O_3 in ZrB_2 at temperatures below which coarsening is significant (1650–1850 °C) to thus retain the original particle size up to the temperatures where densification can proceed.

In most studies on ZrB_2 UHTCs, the starting powders are refined by wet attrition milling using some alcohol or inert organic solvent as liquid media [1].
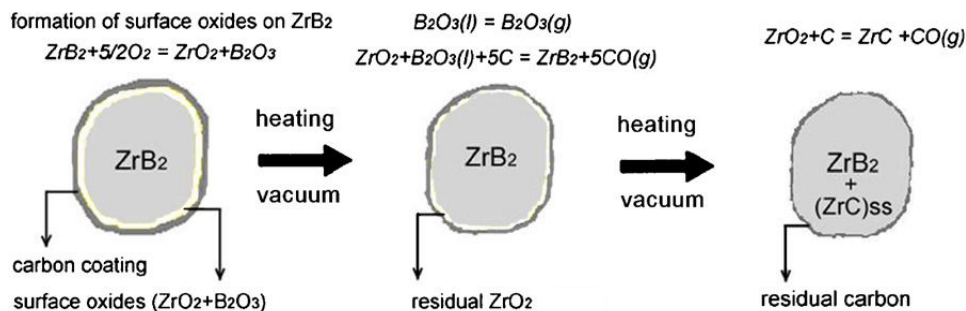

Fig. 2.9 Schematic diagram showing the reactions between the carbon coating and the surface oxides on ZrB_2 particles [5].

Under these wet operating conditions, attrition milling is actually conventional ball-milling because the liquid media reduces the milling intensity, so that its function is only comminution (i.e., particle size reduction). The typical ZrB_2 particles achieved by attrition milling have submicrometer sizes (between 0.6 and 0.2 μm), much smaller than the micrometer-sized particles (~2 μm) of the commonest commercially available ZrB_2 powders.

The current practice used to remove the surface oxides of ZrO_2 consists of adding additives with reducing power to the ZrB_2 powders sintering; the most widely used of which are C, B_4C, and WC [19] and [27]. The oxide B_2O_3 is removed at a temperature lower than 1650 °C from the surface of ZrB_2 through evaporation, keeping active the pump that generates the vacuum.

Apart from the intrinsic surface oxide layer in the ZrB_2 particles, further oxidation of the ZrB_2 powder occurs during the attrition milling. Typically, between 1 and 2 wt.% oxygen is introduced during attrition milling under flowing argon gas atmosphere, and a little bit more (i.e., ~2 wt.%) if the milling is conducted in air [1], [19], [27].

Before this study, the problem about ZrB_2 powder that occurs during high energy ball milling in air, had not received adequate attention, despite its importance.

Predicting this oxidation a priori is difficult because high-energy ball-milling times are fairly short (~3 h) relative to attrition milling times (~24 h), which contributes to minimizing the oxidation, whereas the milling intensity is much higher and the nano-particles are more air-sensitive, which factors have the opposite effect.

It was investigated the oxidation of ZrB_2 powders induced by their high-energy ball-milling in air, because milling in air would simplify the routine of powder preparation. In addition was determined the oxygen uptake, and the structural and chemical statuses of the captured oxygen. 2. The experimental procedure consists in: using a commercially available micrometer ZrB_2 powder with 99% purity and single-crystal particles of average size 2 μm, like starting powder. The as-purchased ZrB_2 powder was subjected to high-energy ball-milling using a shaker mill (Spex D8000, Spex CertiPrep, Metuchen, NJ, US) operated at about 1060 back-and-forth cycles per minute. The milling was carried out in a cylindrical hardened-steel container with WC balls (6.7 mm in diameter) at a ball-to-powder weight ratio of 4, for 180 min, in air. Subsequently, the ball-milled powder was analyzed using various characterization techniques: transmission electron microscopy (TEM) for the direct examination of the size and morphology of the powder particles and nano-crystals, inert gas fusion (IGF) for the determination of the oxygen uptake, X-ray diffractometry (XRD) for the identification of the amorphous or crystalline nature of the phases present, helium pycnometry for

the measurement of the density, and Fourier-transform infrared (FTIR), Raman, and X-ray photoemission (XPS) spectroscopy for the determination of the bonding environment or status.

The TEM observations were made at 200 kV in bright-field mode, using two conventional microscopes (Tecnai G2 20 Twin, FEI, Eindhoven, The Netherlands; and JEM-2100, JEOL, Croissy-sur-Seine, France). The oxygen content measurements were done with IGF determination (TC-136, Leco Instrument, St. Joseph, MI, US) using graphite crucibles, helium gas, and Ni as flux. The XRD data were collected in step-scanning mode (step width 0.02° 2θ, and count time 3 s/step) using a high-resolution laboratory diffractometer (D8 Advance, Bruker AXS, Karlsruhe, Germany) equipped with a primary monochromator that provides pure CuKα1 radiation (λ = 1.54183 Å) and a linear ultra-fast detector. Two measurement ranges were employed: 20–80°, and 20–55°. The phases present were identified with the aid of the PDF2 database, and were quantified using the Rietveld method (Topas 4.1, Bruker AXS, Karlsruhe, Germany). The density measurements were made by helium pycnometry (Stereopycnometer, Quantachrome Instruments, Hartley Wintney, UK). The FTIR spectra were recorded in the 4000–400 cm^{-1} range on a conventional spectrophotometer (Nicolet iS10, Thermo Scientific, East Grinstead, UK), using the KBr pellet method and an accumulation condition of 60 scans at 1 cm^{-1} resolution. The Raman spectra were measured in the 1000–125 cm^{-1} range using a micro-Raman spectrometer (Nicolet Almega XR, Thermo Scientific) equipped with a 633 nm He–Ne laser operated at 5.25 mW power, and were the result of 10 accumulations lasting 1 s. The XPS spectra of the Zr 3d and B 1s core lines were recorded in ultra-high vacuum (10^{-6} Pa) in the 176–194 eV range at 0.4 eV energy resolution using a high-resolution spectrometer (K-Alpha, Thermo Scientific) equipped with a monochromatic Al-Kα X-ray source (1486.6 eV). The C 1s peak was used to correct the binding energies in the XPS spectra. The protocol of sample preparation for each of these techniques followed standard procedures for ceramic powders. Figure 2.10 compares representative TEM images of the as-purchased ZrB_2 powder and of the ZrB_2 powder ball-milled for 180 min in air. Clearly, the high-energy ball-milling has reduced the particle size by one order of magnitude from the micrometre scale (~2–3 μm) to the nanometre scale (~120–200 nm).

Furthermore, higher-magnification TEM images such as that shown in figure 2.11 indicate that the powder particles after high-energy ball-milling are actually porous agglomerates consisting of many individual tiny single-crystals with an average size of ~10 nm. The oxygen contents determined by Inert Gas Fusion were 1.537 and 4.514 wt.% respectively for the as-purchased and ball-milled ZrB_2 powders, so that one can conclude that there is an oxygen uptake of ~3 wt.% during the high-energy ball-milling in air.

a)   b)
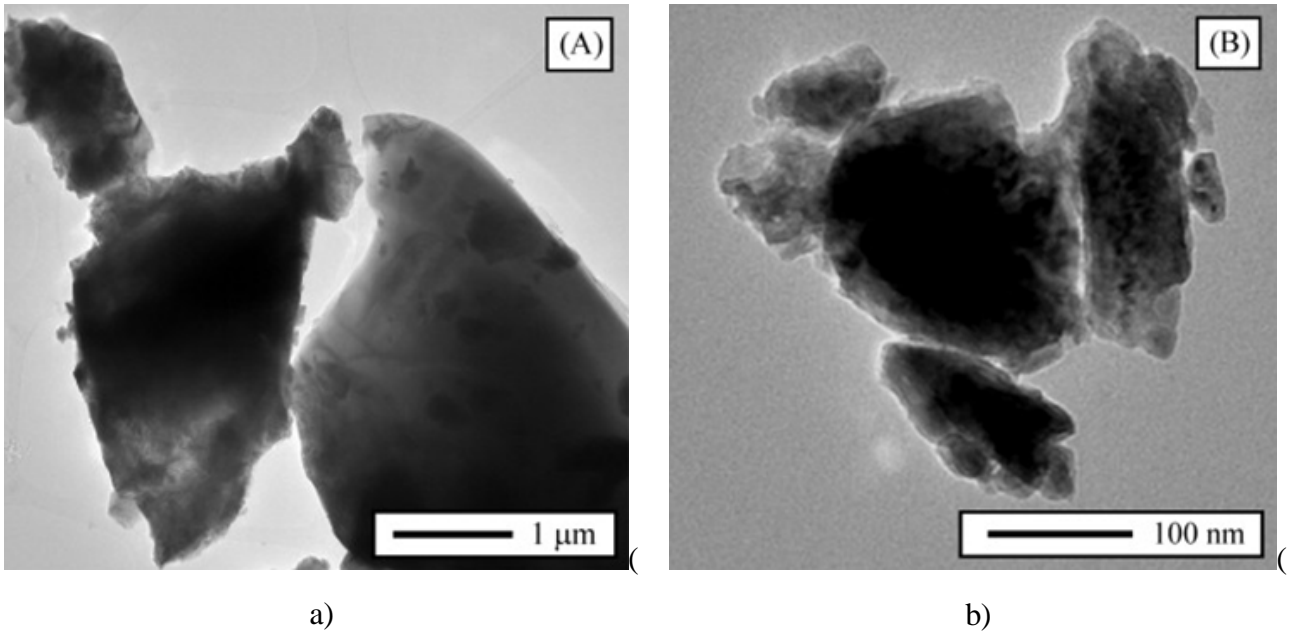
Fig. 2.10 TEM bright-field images of the ZrB_2 powder particles (a) in the as-purchased condition, and (b) after high-energy ball-milling for 180 min in air;
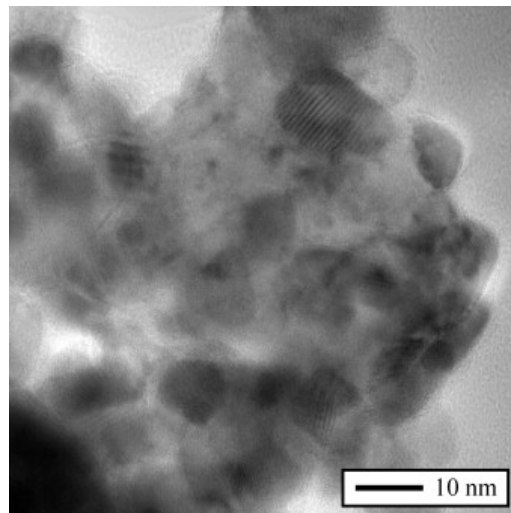
Fig. 2.11 TEM bright-field image of the interior of the ZrB_2 powder particles with 180 min of high-energy ball-milling in air, showing the agglomeration and cold-welding of individual primary nano-particles with 10 nm size;

This oxygen content is greater than typically reported for ZrB_2 powders prepared by attrition milling which are normally in the 2–3 wt.% range depending on the exact milling conditions [7], [19], [29]. To explore the structural and chemical statuses of the oxygen captured during the high-

energy ball-milling in air, an exhaustive characterization of the ball-milled powder was needed, that will be described after.

Figure 2.12 compares the XRD patterns of the ZrB_2 powder before and after the high-energy ball-milling for 180 min in air.
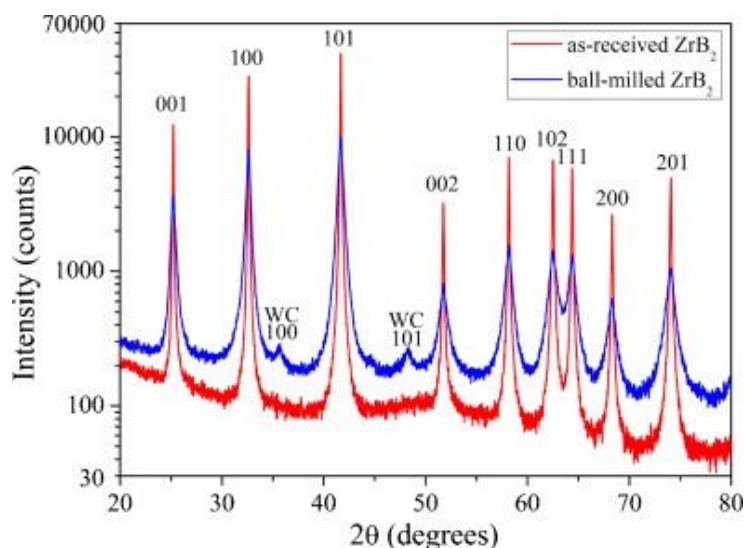
Fig. 2.12 XRD patterns of the ZrB_2 powders before and after high-energy ball-milling for 180 min in air. The WC peaks free of overlap with ZrB_2 peaks (which have been indexed) are marked. The logarithmic scale is to facilitate appreciation of the WC peaks;

Apart from the reduction in the peak intensity, the marked peak broadening, and the increase in the background after the high-energy ball-milling that together reflect the crystallite size refinement to the nanoscale (~10 nm), and the presence of additional peaks that reveal the introduction of 2.5 wt% of WC according to the corresponding Rietveld analysis, there are another two important features in the figure. The first is that the ZrB_2 peaks remain in place. Since the absence of peak shifting excludes the formation of solid-solutions with oxygen atoms as solutes in the ZrB_2 host, it can be concluded that the oxygen captured during the high-energy ball-milling in air has formed oxides. The second is the absence of ZrO_2 and/or B_2O_3 peaks in the XRD patterns of the ball-milled ZrB_2 powder. Taking this observation together with the previous one, one can conclude that these oxides are amorphous. One could nevertheless argue that it would be very difficult to detect B_2O_3 by XRD in the presence of ZrB_2 because the scattering factor of Zr will dominate the entire diffractogram. Nevertheless, ZrO_2 should be detected which would prove the oxidation via the reaction

$$ZrB_2 + 5/2 \ O_2(g) \rightarrow ZrO_2 + B_2O_3 \tag{2.4}$$

27

if this oxidation reaction had resulted in crystalline oxides. It could also be argued that crystalline ZrO_2 and B_2O_3 are formed during the high-energy ball-milling in air, but at amounts below the XRD detection limit. However, given the oxygen content determined by IGF and assuming equimolar formation of ZrO_2 and B_2O_3 as predicted by the preceding reaction, their concentrations is estimated to be 6.95 and 3.93 wt.%, respectively, which are clearly high enough to be detected by XRD. To show that this is in fact the case, two powder mixtures in which 1 wt.% crystalline ZrO_2 was added to ZrB_2 were prepared and analyzed by XRD. In one of these two mixtures the crystals had submicrometer sizes and in the other nanometre sizes, done so as to rule out any crystallite-size effect in the detection of crystalline ZrO_2 in ZrB_2-based powders.
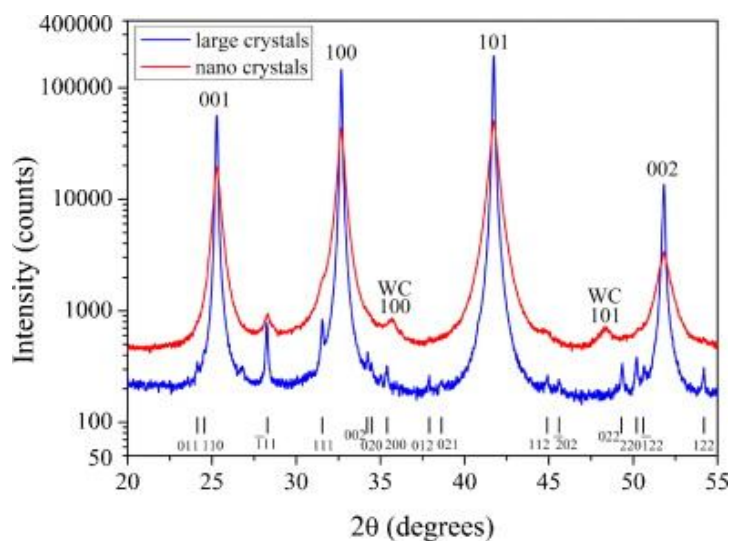
Fig. 2.13. XRD patterns of the ZrB_2 + 1 wt.% ZrO_2 powder mixtures with coarse crystals and with nano-crystals. The WC peaks free of overlap with ZrB_2 peaks (which have been indexed) are marked. The position of the ZrO_2 peaks is marked with short vertical lines. The logarithmic scale is to facilitate appreciation of the ZrO_2 and WC peaks;

It can be seen in figure 2.13 that, even though the low ZrO_2 concentration of only 1 wt.%, the XRD patterns of these mixtures exhibit clear peaks of this oxide. Hence, these observations confirm that the oxide concentration deduced from IGF is above the detection limit of the diffractometer, and therefore that the oxides formed during high-energy ball-milling in air are amorphous because otherwise they would have been detected.

Despite its non-crystalline nature, the amorphous-phase content in the ball-milled ZrB_2 powder can be estimated from its XRD pattern using the Rietveld method in conjunction with the spiking technique (known crystalline internal-standard method). In this case, 30 wt.% Al_2O_3 was used as the

spike phase because it provides a sufficient number of peaks in the XRD pattern with no overlap with the ZrB_2 peaks, and because its oxide nature rules out the presence of a passivating amorphous layer. With this XRD analysis, as shown in figure 2.14, the amorphous-phase content in the ball-milled ZrB_2 powder was calculated to be 12 wt.%, which is clearly consistent with the oxide concentration (i.e., $ZrO_2 + B_2O_3$) determined by IGF (~11 wt.%).
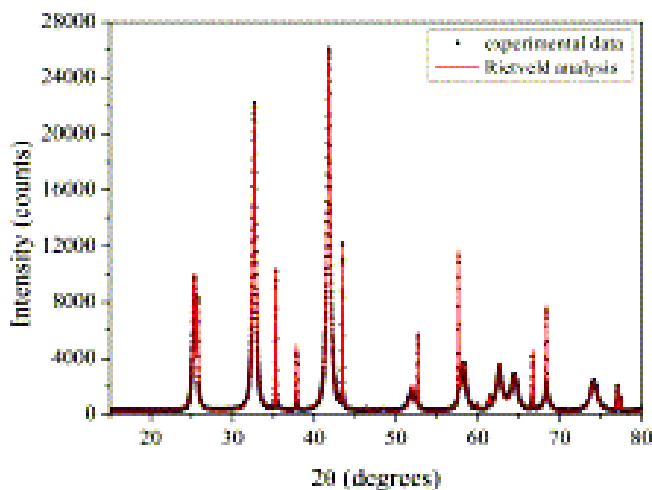
Fig. 2.14. Rietveld analysis of the XRD pattern of the ZrB_2 powder with 180 min of high-energy ball-milling in air plus 30 wt.% of Al_2O_3 powder. The points are the experimental data and the solid line is the Rietveld refinement [20];

The measurements of the powder density performed by helium pycnometry also lend strong credence to the formation of amorphous oxides, as they show that the density decreases from 6.12 g/cm^3 in the as-purchased condition to 5.82 g/cm^3 after 180 min of high-energy ball-milling in air. Using the rule-of-mixture with the values of theoretical density and volume concentrations determined experimentally of ZrB_2 (6.1 g/cm^3, 86.94 wt.%), WC (17.67 g/cm^3, 2.23 wt.%), ZrO_2 (5.86 g/cm^3, 6.91 wt.%) and B_2O_3 (2.46 g/cm^3, 3.93 wt.%), the density of the ball-milled powder was calculated to be 5.826 g/cm^3, in perfect agreement with the experimental measurement.

The as-purchased and ball-milled ZrB_2 powders were investigated by XPS, to confirm the formation of amorphous oxides as deduced from the XRD, IGF and helium pycnometry analyzes. In particular, it was monitored the binding energy of the Zr 3d and B 1s core levels and after the high-energy ball-milling for 180 min in air (Fig. 2.15). One observes that the Zr 3d core level shows the typical 3d5/2 and 3d3/2 spin–orbit split, while the B 1s core level exhibits the typical single peak. However, two Zr 3d5/2–3d3/2 doublets and two B 1s singlets are observed in each powder, which is a clear sign of the existence of two different bonding statuses for the Zr and B atoms. In both the

as-purchased and the ball-milled powders, one set of Zr 3d5/2–3d3/2 doublets plus B 1s singlet is located at binding energies of ~179.2, 181.6, and 188.2 eV, respectively, values which are due to ZrB_2. The other set of doublets plus singlet appears at higher binding energies of ~183.5, 185.9, and 193.1 eV, respectively, which are due to ZrO_2 and B_2O_3. One also observes that the ZrO_2/ZrB_2 and B_2O_3/ZrB_2 peak intensity ratios are greater in the powder subjected to high-energy ball-milling in air. Therefore, XPS has clearly detected the presence of ZrO_2 and B_2O_3 in the as-purchased and ball-milled ZrB_2 powders, and also shows them to be much richer in the ball-milled powder. Also noted in the XPS spectra of the two powders are that the ZrO_2 related peaks are more intense than the ZrB_2 related peaks. This observation, together with the oxygen contents that showed that the oxides are minor components and the fact that XPS is a surface technique, indicate that ZrO_2 and B_2O_3 cover the surface of the ZrB_2 particles. This hypothesis was further tested experimentally in the ball-milled powder by etching the surface with Ar^+ ions to remove material followed by XPS data collection, and also by TEM. And was discovered that the ZrB_2/ZrO_2 and ZrB_2/B_2O_3 peak intensity ratios increase after the etching, a clear sign that the ZrB_2 powder particles are covered by an oxide layer.
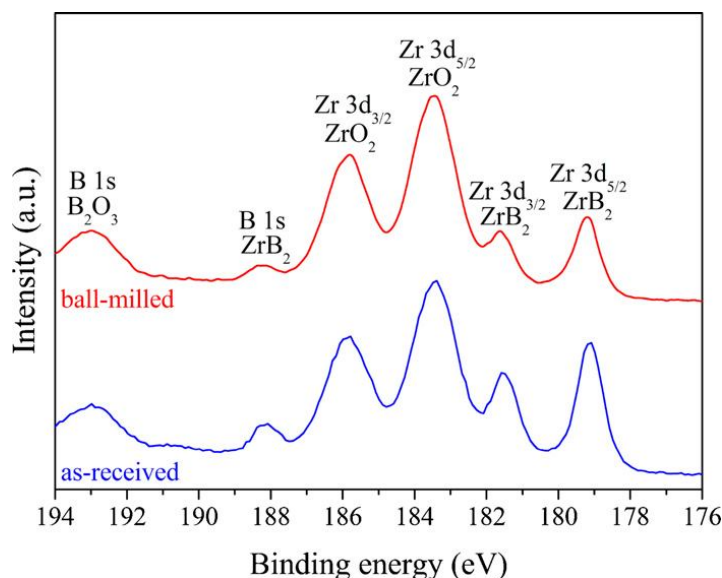
Fig. 2.15. High-resolution XPS spectra of the Zr 3d and B 1s core-levels for the ZrB2 powders before and after high-energy ball-milling for 180 min in air. Also included in the figure is the peak indexing. The spectra have been shifted along the Y-axis to facilitate comparison;

As can be seen in figure 2.16, the direct high-resolution TEM observations also support the presence of an amorphous nano-film at the fringe of the agglomerates.
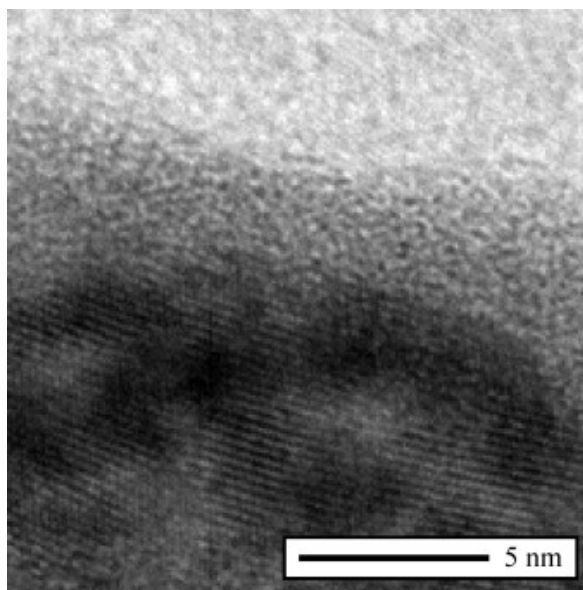
Fig. 2.16. High-resolution TEM bright-field image of the fringe of the ZrB_2 powder particles with 180 min of high-energy ball-milling in air, showing the presence of an amorphous region of nanometre thickness;

This oxide distribution is attributed to two factors: (i) the lower chemical affinity between the oxides and ZrB_2 than between ZrB_2 crystals themselves which would promote cold-welding during the high-energy ball-milling via contacts of the type ZrB_2–ZrB_2; and (ii) the spontaneous surface passivation of ball-milled powder particles when exposed to ambient conditions after the high-energy ball-milling.

Finally, it is worth mentioning that a recent spark-plasma sintering (SPS) study has revealed that the greater oxygen content of this ZrB_2 nano-powder obtained by high-energy ball-milling in air does not hinder its densification. On the contrary, it exhibits improved SPS kinetics relative to powders with larger particles and less oxygen content, which has been attributed to the large inter-particle boundary surface area that can greatly enhance grain-boundary diffusion at lower temperatures. Whether the SPS results can or not be extrapolated to the pressureless sintering (PS) is something that has yet to be investigated experimentally. Either the case, it is reasonable to think that the sinterability of this ZrB_2 nano-powder (by SPS, PS, or hot-pressing) would improve further if the high-energy ball-milling were performed in an inert atmosphere, although the comminution routine would be more tedious and costly [20].

One promising approach for improving densification is the use of rapid heating rates through temperature regimes where grain coarsening occurs. Rapid heating rates (50°C/min) through temperature regimes where coarsening occurred increased the final relative density. Their TGA

31

results showed that rapid heating in vacuum or under H_2 accelerated the volatilization of B_2O_3, leaving less time for particle coarsening. Using this approach, C-rich B_4C ceramics with relative densities greater than 98% were produced by sintering at 2050°C [7]. In other studies the removal or control of the amount of B_2O_3 has led to reductions in grain coarsening, which was attributed to elimination of a rapid diffusion path [31].

Chapter 3

PRODUCTION METHODS

3.1 INTRODUCTION

ZrB_2 ceramics and ZrB_2-based composites have been densified by the various methods, including hot pressing (HP), spark plasma sintering (SPS), reactive hot pressing (RHP), and pressureless sintering (PS). Hot-pressing is the most commonly used densification method for the ZrB2-based ceramics in historic studies. Recently, pressureless sintering, reactive hot pressing, and spark plasma sintering processes evolved as the most common densification methods. This section focuses on these four densification processes, as well as on the effects of additives, such as carbides, nitrides and disilicides, on the densification behaviour of zirconium diborides.

Compositions with added carbides and disilicides displayed significant improvement of densification and made pressureless sintering possible at ≤ 2000 °C. Reactive hot-pressing allows in situ synthesizing and densifying of ZrB_2-based composites. Spark plasma sintering displays a potential and attractive way to densify the ZrB_2 ceramics and ZrB_2-based composites without any additive. [4]

3.1.1   HOT PRESSING

In most cases, ZrB_2-based materials are densified by hot pressing, which is limited to relatively simple geometric shapes. Fabrication of complex components requires expensive and time-consuming diamond machining. Development of pressureless sintering processes would be advantageous as components could be fabricated to near-net shape. [7]

Typically, HP of ZrB_2 required a temperature of 2100 °C or above and moderate pressure (20–30 MPa), or lower temperatures (~1800 °C) and extremely high pressures (>800 MPa) [4]. The low intrinsic sinterability of ZrB_2 has been attributed to the covalent character of the bonding as well as low-volume and grain boundary diffusion rates. [7]

Table 3.1 Starting powder size, hot pressing conditions and final densities of the hot-pressed ZrB_2 ceramics and ZrB_2-based composites with various additives [4];

Compositions (vol%)	Particles size (μm)		Remarks	Hot-pressing conditions	Final density (%)
	ZrB_2	SiC or $MoSi_2$ or $ZrSi_2$			
ZrB_2	20		Ball-milled	2000 °C/20 min/20 MPa	73
ZrB_2	2.1		Ball-milled	2000 °C/60 min/30 MPa	91
ZrB_2	2		Attrition-milled	1900 °C/45 min/32 MPa	99.8
ZrB_2	2		Ball-milled	1650 °C/20 min/60 MPa	71.6
ZrB_2	5–10		Ball-milled	1800 °C/60 min/20 MPa	78
ZrB_2–2.5 wt% Si_3N_4	0.1–8		Ball-milled	1700 °C/15 min/30 MPa	98
ZrB_2–5Si_3N_4	2		Ball-milled	1700 °C/15 min/30 MPa	98
ZrB_2–4.6AlN	0.1–8		Ball-milled	1850 °C/30 min/30 MPa	92
ZrB_2–15SiC–4.5ZrN	d_{90}- = 4–6		Ball-milled	1900 °C/5 min/50 MPa	99
ZrB_2–37.5HfB_2–19.5SiC–3HfN	2		Ball-milled	1900 °C/30 min/50 MPa	>99.9
ZrB_2–5.7SiC	2	1.7	Ball-milled	1650 °C/120 min/60 MPa	81.6
ZrB_2–22.4SiC	2	1.7	Ball-milled	1650 °C/120 min/60 MPa	97.9
ZrB_2–22.4SiC	2	0.04	Ball-milled	1650 °C/120 min/60 MPa	99.6
ZrB_2–30SiC	6	10	Attrition-milled	1900 °C/45 min/32 MPa	97.4
ZrB_2–30SiC	6	0.7	Attrition-milled	1900 °C/45 min/32 MPa	98.7
ZrB_2–16(SiC + C)	5–10	Polycarbosilane (PCS)	Ball-milled	1800 °C/60 min/20 MPa	100
ZrB_2–20$MoSi_2$	2	2.8	Ball-milled	1800 °C/5 min/30 MPa	98.1
ZrB_2–20$MoSi_2$	2.1	3.1	Ball-milled	1800 °C/30 min/30 MPa	99.8
ZrB_2–20$ZrSi_2$	2.1	2.5	Ball-milled	1400 °C/30 min/30 MPa +1550 °C/15 min/30 MPa	99.1
ZrB_2–20$MoSi_2$	20	3–5	Ball-milled	2000 °C/20 min/20 MPa	95

These studies [4] showed that densification of ZrB_2 is a diffusion-controlled rate process. Results of HP studies on commercially available ZrB_2 powders are summarized in Table 3.1, which includes

details of the starting powders, sintering additives, HP conditions, mixing method and final densities.

It has been found that HP of coarse ZrB_2 powder (d ≈ 20 μm) at 2000 °C with a pressure of 20 MPa achieved only a relative density of ~73%, whereas the relative density of ~91% was obtained for a finer ZrB_2 powder (d ≈ 2.1 μm) under the same HP conditions. Furthermore, the attrition-milled ZrB_2 powder, with average particle size of d ≤ 0.5 μm, required HP at 1900 °C and 32 MPa for 45 min to achieve full density [27]. The lower HP temperature was attributed to reduction of starting particle size from microns (d ≈ 2.1 μm) to submicrons (d ≤ 0.5 μm) by attrition-milling [4].

Oxygen impurities (B_2O_3 and ZrO_2) present on the starting powder surfaces have been shown to inhibit densification and to promote grain growth in the non-oxide ceramic systems. At relatively low temperatures (~1750°C) the presence of B_2O_3 as a liquid and/or a vapour is thought to provide a rapid diffusion path along the surface of the particles, which would promote coarsening. Grain coarsening reduces the surface area of the particles and decreases the driving force for sintering. For materials with the AlB_2 crystal structure, coarsening leads to the formation of faceted grains and trapped pores within the large grains. Baik and Becher [31] showed that the grain size of TiB_2 was affected by the initial oxygen content of the precursor powders. When the oxygen content doubled, the average grain size increased by 300%. Investigation of the microstructure showed that samples with higher oxygen contents were more likely to contain pores within grains.[7]

Studies focused on the sintering of B_4C and TiB_2 have shown that fine starting particles, a proper sintering schedule, control of oxygen impurities (content must be less than 0.5 wt% to achieve full density [4]), and some additives can improve sinterability. The effect of particle size on sintering has been demonstrated for TiB_2. Studies performed [7] showed that decreasing particle size by grinding significantly increased the linear shrinkage of TiB_2 during sintering. The increased linear shrinkage was attributed to a decrease in activation energy. The decrease in activation energy was thought to be because of the reduction in particle size and also the formation of defects that were induced by grinding [7].

Recently, metallic additives like Ni, [32] and [28] SiC, Si_3N_4, [33] AlN, HfN o ZrN have been studied to reduce sintering temperature, added to ZrB_2, producing an intergranular secondary phase and/or reducing oxygen content, both of which assists in the densification of ZrB_2. [4] Even with these additions, an external pressure is still required for densification. In addition, these additives drastically reduce the elevated temperature strength ($\sigma_{1200} = 50.5 \, \sigma_{R.T.}$) [7].

Silicon carbide is the most common additive for ZrB_2 or HfB_2 ceramics. The addition of SiC improved the sinterability, inhibited grain growth and increased the oxidation and ablation

resistance of ZrB_2 and HfB_2 ceramics as well. Some topics showed that ZrB_2 with 10 vol% ultra-fine SiC (d90 = 0.8 μm) achieved full density by HP at 1900 °C and 40 MPa for 20 min in vacuum. The attrition-milled ZrB_2–30 vol% SiC mixture powders (d ≈ 0.5 μm) could be hot-pressed at 1900 °C to a relative density exceeding 97%. Furthermore, the addition of 22.4 vol% nano-sized SiC, with average particles sizes ranging from ~ 40 nm to 0.6 μm, sharply reduced the HP temperature necessary to achieve full density to 1650 °C (pressed for 120 min at 60 MPa). The improvement of densification upon addition of SiC was attributed to the formation of intergranular liquid phases during hot-pressing, assisting in densification at lower temperatures. An early study [32] in 4 wt% Ni-containing ZrB_2 showed that the presence of the liquid phase not only favours ZrB_2 particle rearrangement but also enhances mass transfer kinetics. However, the improvement of densification upon addition of ultra-fine SiC is effective only for a uniformly dispersed SiC–ZrB_2 system. The agglomeration of the ultra-fine SiC particles led to reduced improvement in densification of ZrB_2, even with nano-sized SiC particles. Recently, a polycarbosilane (PCS) was used as a source of SiC and C because the pyrolyzed PCS can crystallize and convert to β-SiC and amorphous C at 1000 °C or above. HP of the PCS-coated ZrB_2 powder required a reduced temperature of 1800 °C (pressed for 60 min at 20 MPa) to achieve a full density when SiC content was ≥16 vol%. For comparison, the ZrB_2 powder without PCS coating was highly porous with a relative density of 78% under the same HP conditions.

Nitrides are other effective additives for improving sinterability or enhancing densification of ZrB_2. The main reason for incorporating nitrides as additives is the propensity of nitrides to consume the oxygen-bearing species on the diboride powder surfaces. The reduction of oxygen results in higher boron activity, which is one of the conditions favouring lattice diffusion and, therefore, densification. The addition of ≥2.5 wt% Si_3N_4 results in almost fully dense ZrB_2 (RD: 98%) after compactions at 1700 °C and 30 MPa for 15 min. [33]. Some grain boundary phases, including BN, ZrO_2, $ZrSi_2$, and borosilicate glassy phase, were confirmed to be present in pockets at multiple-grains junctions for the ZrB_2-based ceramics with Si_3N_4, the result of a reaction of an oxide impurity with Si_3N_4. That reaction results in elimination or decrease in the oxide impurity on the ZrB_2 particles surfaces, thereby promoting densification. Similar to Si_3N_4, the primary effect of an AlN additive is the depletion of the ZrB_2 particles from the outer oxide layer that prevents the formation of highly dense compacts. Compared to AlN and Si_3N_4 additives, the ZrN and HfN showed the unexpected advantage of limiting undesirable secondary phases that eventually become detrimental to high temperature stability. It has been reported [4] that HP of 3 vol% HfN–HfB_2–SiC or 4.5 vol% ZrN–ZrB_2–SiC required 1900 °C for 30 min at a pressure of 40 MPa. The resulting composites showed a fine and homogenous microstructure with secondary phases such as M(C, N),

MO$_2$ (M = Zr and/or Hf) and BN. The formation of the secondary phases during sintering was traced back to the interactions among ZrN or HfN, carbon, and oxides such as B$_2$O$_3$ and ZrO$_2$ or HfO$_2$. These interactions accelerated the densification of ZrB$_2$ or HfB$_2$ ceramics by reducing the oxygen content on the starting powder surfaces. The resulting intergranular secondary phases possess higher refractoriness than those made with AlN or Si$_3$N$_4$ additives.

Transition metal disilicides have been found to be an alternative and effective sintering additive because they improve sinterability and increase oxidation resistance of ZrB$_2$ ceramics as well. In the early 1970s, MoSi$_2$ significantly improved sinterability of ZrB$_2$ powder and a relative density exceeding 95% was obtained for ≥20 vol% MoSi$_2$-containing ZrB$_2$ powder at 2000 °C and 20 MPa for 20 min. Recently, it has been reported that HP of the ZrB$_2$-based ceramics with MoSi$_2$ required only a temperature ≤1800 °C. The higher sintering temperature required in the earlier study resulted from larger ZrB$_2$ (d ≈ 20 μm) and MoSi$_2$ (d ≈ 5 μm) particles. More recently, it was found that addition of 10–40 vol% ZrSi$_2$ could further lower the densification temperature of ZrB$_2$ to 1550 °C or below. Furthermore, fully dense ZrB$_2$–ZrSi$_2$ composites with a fine and homogeneous microstructure, using a two-step HP process, which consisted of a first stage at 1400 °C for 30 min and a second stage at 1550 °C for 15 min at a pressure of 30 MPa were obtained. Thus, the disilicides of the transition metals are potential additives for lowering the sintering temperature of the ZrB$_2$-based ceramics. Consequently, it is possible to further lower the sintering temperature of ZrB$_2$-based ceramics by selecting appropriate disilicides of transition metals. Improvement of densification, resulting from addition of disilicides, is attributed to two major causes. One is formation of an intergranular Si–O–B liquid phase between MoSi$_2$ or ZrSi$_2$ and ZrB$_2$ particles due to the interaction of SiO$_2$ and B$_2$O$_3$ that occurs on the surfaces of particles. Another is the ductile deformation of MoSi$_2$ or ZrSi$_2$ particles at high temperature (>800 °C). This deformation could force soft MoSi$_2$ or ZrSi$_2$ particles to fill in the voids left by the ZrB$_2$ skeleton under pressure during sintering, thus improving densification [4].

3.1.2   SPARK PLASMA SINTERING

SPS is one of the most recent advanced processing techniques developed for densifying ceramic materials. Although SPS is similar to HP, in place of indirect heating, the applied electrical field heats the die and the powder compact. One advantage of using SPS is to enhance densification of poorly sinterable ceramics, by simultaneously applying a uniaxial load and a direct or pulsed electric current to a powder compact. Another advantage is that the grain growth of starting

materials is restricted, since a considerable shorter sintering time (within minutes) is needed compared to HP or hot isostatic pressing (HIP), thereby retaining the fine and homogeneous grains.

Table 3.2 Spark plasma sintering conditions, final density, and grain size of ZrB_2 ceramics and ZrB_2 or HfB_2-based composites produced by an SPS process;

Compositions	Heating rate	SPS conditions	Final density (%)	Grain size (μm)
ZrB_2–30ZrC–10SiC (vol%)	100 °C/min	2100 °C/2 min/30 MPa/vacuum	96	~3
HfB_2–30SiC (vol%)	100 °C/min	2100 °C/2 min/30 MPa/vacuum	100	2
ZrB_2–15MoSi$_2$(vol%)	100 °C/min	1750 °C/7 min/30 MPa/vacuum	97.7	~1.4
(15–70)ZrB_2–(15–70)ZrC–(15–50)SiC(mol.%)	~400 °C/min	1950 °C/2 min/50 MPa/Ar	>98	–
26.18ZrB_2–59.87ZrC–13.95SiC(wt%)	~400 °C/min	1900 °C/5 min/30 MPa/Ar	99.9	–
24.17ZrB_2–56.88ZrC–13.25SiC–5AlN(wt%)	~400 °C/min	1850 °C/5 min/30 MPa/Ar	99.5	–
24.17ZrB_2–56.88ZrC–13.25SiC–5AlN(wt%)	~400 °C/min	1900 °C/5 min/30 MPa/Ar	100	–
ZrB_2	~300 °C/min	1900 °C/3 min/50 MPa/vacuum	97.6	5.1
ZrB_2	~300 °C/min	1900 °C/10 min/50 MPa/vacuum	~80	10
ZrB_2	~300 °C/min	1950 °C/3 min/50 MPa/vacuum	98	19
HfB_2–(1–9)MoSi$_2$ (vol%)	100 °C/min	1750 °C/3 min/100 MPa/vacuum	>97	1
HfC–9MoSi$_2$ (vol%)	100 °C/min	1750 °C/3 min/100 MPa/vacuum	99	0.8

Previous investigations of compaction of oxide, nitride, and carbide ceramics produced by SPS have shown that the sintering time, heating rate and sintering temperature are the important factors controlling fine-grained microstructure and densification. In particular, the selection of the sintering temperature is critical for the development of the optical microstructure.

Recent studies have shown that SPS enhanced densification and refined microstructure of ZrB_2-based ceramics can be achieved in very short processing cycles. Table 3.2 summarizes SPS conditions, final density, and grain size of ZrB_2-based ceramics produced by SPS.

It was shown that 60ZrB_2–30ZrC–10SiC (vol%) composition could be sintered to a relative density of ~ 96% at 2100 °C and 30 MPa for 2 min. Grain size measurement indicated that the grain growth (maximum grain size: ~3 μm) was inhibited during SPS. Recently, the various ZrB_2–ZrC–SiC

compositions could be sintered to the fully dense compacts with fine and homogenous microstructure at 1950 °C and 30 MPa for 2 min, by using the SPS technique. This discrepancy in the sintering temperature is probably associated with starting powder size and SPS conditions. In addition, extending soaking time from 3 min to 5 min can produce fully dense ZrB_2–ZrC–SiC composites at a lower temperature (1900 °C). Furthermore, addition of 5 wt% AlN results in complete densification at 1850 °C and 30 MPa for 5 min, but addition of 5 wt% Si_3N_4 still required a temperature of 1900 °C. The discrepancy in densification temperature due to additions of AlN and Si_3N_4 is likely attributable to a lower onset temperature of densification and a faster shrinking rate for the AlN addition as compared to the Si_3N_4 addition. For the ZrB_2–15 vol% $MoSi_2$, however, the density and grain size measurements of the compacts consolidated at 1750 °C showed that SPS was not superior to HP. Soaking time and total sintering time were noticeably shorter for SPS (7–24 min) than for HP (20–140 min).
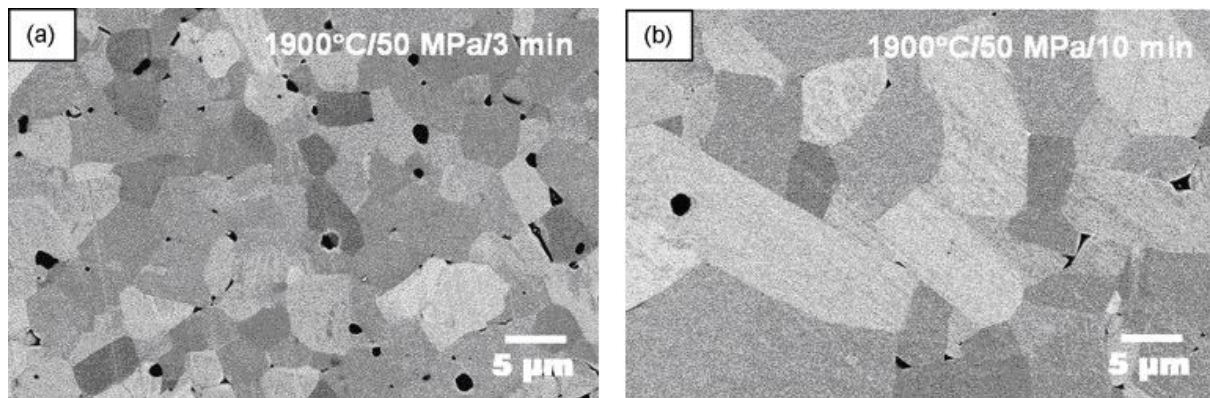
Fig. 3.1 FE-SEM backscattered electron image of the ZrB_2 ceramics consolidated by SPS at 1900 °C for different holding time of (a) 3 min and (b) 10 min with heating rate of ~200 °C/min under a pressure of 50 MPa in vacuum;

Densification and grain size of the sintered ZrB_2 compacts were strongly dependent on the selection of sintering temperature, holding time, as well as the heating rate. It was possible to obtain the almost fully dense ZrB_2 ceramics with a fine and homogeneous microstructure by selecting the appropriate sintering parameters (Fig. 3.1 (a)).

Without sintering additives, full density has, historically, been achieved only by HP at temperatures ≥2100 °C. Densification and grain growth occurred simultaneously during the sintering. As a result, it was difficult to obtain a full density ZrB_2 compact. SPS of ZrB_2 ceramics required a temperature of 1900 °C, a holding time of 3 min, and a heating rate of 200 °C/min or above. Increasing the sintering temperature to 1950 °C or extending the holding time to 10 min or above, as well as

lowering the heating rate below 200 °C/min, led to coarsening of the grain size (typical example, Fig. 4.1(b)). In addition, SPS has been used for applications in other transition metal diborides, such as HfB_2–SiC, TiB_2–WB_2–CrB_2, TiC–TiB_2, HfB_2–$MoSi_2$, and HfC and HfB_2-based composites with $MoSi_2$ additives. The enhanced densification resulting from SPS was attributable to mass transfer processes, which are significantly enhanced in the process, effectively promoting densification. The mechanism in SPS technique that enhanced densification – mainly whether or how an electric discharge is involved in accelerating the densification and grain growth – is still the subject of intense debate. However, we suggest that enhancement is most probably due to (i) an efficient heat transfer; (ii) the use of comparatively high pressure; (iii) the presence of an electrical field (use of DC pulses); and (iv) the presence of local spark discharges generated between the powders under high-energy electrical pulses [4].

3.1.3 REACTIVE HOT-PRESSING

The use of metallic and ceramic additives during HP could reduce temperature of densification and also inhibit grain growth in ZrB_2 ceramics. However, the significant decreases in the strength at temperatures above 1200 °C that result from softening of intergranular amorphous phase at elevated temperatures has been reported for ZrB_2-based composites with SiC [32], [28] and [33] RHP has been identified as a potential route to produce ZrB_2 ceramics with low impurity levels and high density at a lower temperature. There are two processes that occur in RHP, in situ reaction of precursor powders and densification, which must be completed simultaneously during heating and subsequent holding.

Recently, RHP has been used to produce ZrB_2 and/or HfB_2 dense compacts by using Zr and/or Hf and B precursors as well as to fabricate the ZrB_2-based composites with SiC and/or ZrC by using Zr, Si and B_4C precursors. Table 4.3 summarizes RHP sintering conditions, precursors, grain size and final density of the ZrB_2 ceramics and ZrB_2-based ceramics fabricated by RHP.

There was employed slow heating (~1 °C/min) and extended isothermal holds at an extremely low temperature (6 h at 600 °C) to react fine powders of Zr and B without ignition of self-propagating high-temperature synthesis (SHS) reaction. When the samples were heated to 1650 °C in an argon atmosphere, an applied external pressure of 40 MPa produced an almost fully dense, nano-sized ZrB_2 compact. Raising the temperature to 1700 °C increased the density to 99%, however, the ZrB_2 grains were significantly coarsened. The grain size measured in the sample densified at 1800 °C was ~1.5 μm, larger by a factor of ~3 than that at 1650 °C.

Table 3.3 Reactive hot-pressing conditions, precursors, grain size and final density of ZrB_2 or HfB_2 ceramics and ZrB_2 or HfB_2-based composites fabricated by a RHP method;

Materials	Precursors	Remarks	HP or SPS Processing conditions	Final density (%)	Grain size (µm)	
					ZrB_2	SiC
ZrB_2	Zr, B	Attrition-milled	1650 °C/30 min/40 MPa/Ar (HP)	>95	0.5	–
HfB_2	Hf, B	None	1700 °C/10 min/95 MPa/vacuum (SPS)	~98	–	–
HfB_2	HfB_2	None	1900 °C/10 min/95 MPa/vacuum (SPS)	~87	–	–
ZrB_2–SiC	Zr, Si, B_4C	Ball-milled	1900 °C/60 min/30 MPa/Ar (HP)	96.7	3–10	<3
ZrB_2–SiC–ZrC	Zr, Si, B_4C	None	1800 °C/60 min/20 MPa/Ar (HP)	96.8	–	–
ZrB_2–SiC	Zr, Si, B_4C	Ball-milled	1450 °C/3 min/30 MPa/vacuum (SPS)	~98.5	<5	<1
ZrB_2–SiC	Zr, Si, B_4C	Ball-milled	1890 °C/10 min/30 MPa/vacuum (HP)	100	2	1
HfB_2–SiC	Hf, Si, B_4C	Ball-milled	1900 °C/60 min/50 MPa/vacuum (HP)	100	3	1

In contrast, HP of commercially available micron-sized ZrB_2 powders (d $\approx$ 2.1 µm) at 2000 °C and 20 MPa for 60 min achieved only a relative density of ~91%, with an average grain size of 6.1 µm. The improvement of densification by RHP was attributed to the formation of nano-sized ZrB_2 particles during the reactive process because the fine crystalline size should enhance the driving force for densification when the densification is driven by minimization of the surface free energy.

Another application of RHP is to produce ZrB_2-based composites with SiC and/or ZrC, using Zr, Si, and B_4C powders as precursors. It was used RHP to fabricate ZrB_2-beased composites with SiC, by reacting Zr, Si and B_4C at 1800 °C where the following reaction (3.1) is thermodynamically favourable:

$$2Zr + Si + B_4C = 2ZrB_2 + SiC \qquad (3.1)$$

The relative density of ~98% was obtained by RHP of Zr, B and B_4C powder mixtures at 1900 °C and 30 MPa for 60 min. Later, was also successfully consolidated ZrB_2–SiC–ZrC composites (RD: ~97%) by RHP of Zr, Si and B_4C powders at 1800 °C and 20 MPa for 60 min in an argon atmosphere. They found that the reactions for producing ZrB_2, ZrC and SiC were not simultaneously induced during the sintering, but in steps. ZrB_2 and ZrC were first formed by the reaction of B_4C with Zr at a low temperature, then SiC was produced by reaction of Si with ZrC and the residual B_4C at a higher temperature. In addition, it was founded that excess B_4C and Si were necessary in the ZrH_2–B_4C–Si system for obtaining ZrB_2–SiC composites without oxide impurity as well as for avoiding grain coarsening during the sintering process. They showed that RHP produced ZrB_2-based ceramics with 27 vol% SiC in the presence of excess B_4C and Si, with an average ZrB_2 grain size of ~2 μm and a SiC particle size of ~1 μm. For comparison, in a stoichiometric ZrH_2, B_4C and Si mixture, the reaction resulted in 25 vol% SiC-containing ZrB_2, accompanied by traces of ZrC and ZrO_2, as a result of deficiency of available boron in the reaction mixture. The grain size appeared to increase from ~2 μm to ~5 μm for the ZrB_2 and from ~1 μm to ~3.5 μm for the SiC. Similarly, RHP is also used to produce the HfB_2-based composites. It was obtained a fully densified HfB_2–22 vol% SiC–6 vol% HfC at 1900 °C and 50 MPa for 60 min through reaction of a mixture of Hf, B_4C and Si powders.

Recently, RHP has also been utilized to produce HfB_2 by reaction of Hf and B powders at a low temperature, by using SPS. An almost fully densified HfB_2 compact was achieved by reacting Hf and B at 1700 °C and 95 MPa for 10 min in vacuo using SPS, instead of HP. For comparison, HfB_2 ceramics produced from commercially available powder could achieved only ~62% and ~87% densities at 1800 °C with 30–85 MPa for 10 min, and at 1900 °C with 80–95 MPa for 10 min, respectively. The reaction between Hf and B occurred at 1100 °C, while the completion of the reaction extended over a relatively wide temperature range. However, the association of the reaction with densification was absent during the reactive sintering. Densification was observed only at a temperature where the conversion to the diboride was complete. In addition, it has been shown that the reactive sintering of Zr, Si and B_4C precursors could be conducted by SPS. The reactive SPS required a lower temperature of ≥1450 °C with a shorter holding time of 3 min. The resulting composites had a finer and more homogeneous microstructure, compared with that from RHP. Thus, the simultaneous synthesis and consolidation of the Zr, B, or B_4C and Si precursor powders, i.e. reactive sintering, could produce the densified ZrB_2-based composites at a lower temperature by using either HP or SPS, as compared with direct consolidation of commercially available powders [4].

3.1.4 PRESSURELESS SINTERING

In studies that were conducted in the 1970s and earlier, densification of ZrB_2 ceramics was only accomplished by HP. Because of the extreme pressures required for densification, pressureless sintering of ZrB_2 was considered unlikely or impossible until the late 1980s, when studies of pressureless sintering actually began to show results. Compared with HP, the development of a PS process would enable almost-net-shape processing of ceramic parts with complex geometries using standard powder-processing methods, thus reducing processing costs. Various additives have been used to improve densification of ZrB_2. In general, the additives used can be divided into main two groups: liquid phase formers, and reactive agents. Table 3.4 summarizes the PS conditions, agents used, grain size and final density of the resulting ZrB_2 ceramics.

Liquid phase formers include refractory metals, such as Ni, Fe, Co, Cr and Mo, as well as disilicides of transition metals, such as $MoSi_2$ and $ZrSi_2$. Fe and Cr decrease the densification temperature but reduce the strength at elevated temperatures and oxidation resistance. It was used Ni, Co, Fe and Re to produce an almost fully densified ZrB_2 at 2000 °C and 2200 °C in vacuo or in an argon atmosphere [4]. They found that addition of $\geq$ 2 wt% of metals was required to bring about adequate sintering, because formation and continuous action of a liquid phase occurred only at higher contents of added metals. The additions are more efficient for producing adequate sintering in an argon atmosphere than in vacuum because of loss of the added metals in the vacuum from volatilization. Lattice parameter measurements showed a gradual decrease in the crystal lattice dimensions during sintering, resulting from substitution of zirconium atoms in the ZrB_2 lattice by the atoms of the added metals. Obviously, the mode of action of these metallic additives that influence sintering is associated with an appreciable contraction of the ZrB_2 crystal lattice.

Presumably, the contraction of the ZrB_2 crystal lattice affected the surface free energy, and, consequently increased the driving force for densification. A study in TiB_2 with Ni, NiB, and Fe showed that a relative density exceeding 94% was obtained at a temperature $\geq$1500 °C without external pressure, but was accompanied by significantly exaggerated grain growth. The addition of carbon inhibited grain growth, but also significantly increased the porosity. The authors hypothesized that the densification process occurs by redistribution followed by dissolution–reprecipitation in the nickel-rich melt, and that the grain growth was caused by surface diffusion in a titanium-oxide-rich surface layer. In addition, it was found that with Mo additions up to 15 wt% the energy of activation of the densification process drops below 380 kJ/mol from 680 kJ/mol because Mo was incorporated into a ZrB_2 solid solution.

Table 3.4 Pressureless sintering conditions, grain size, and final densities of the pressureless sintered ZrB_2 ceramics with various additives;

Compositions	Remarks	Pressureless sintering conditions	Final density (%)	Grain size (µm)
ZrB_2–20 vol% $MoSi_2$	Ball-milled	1850 °C/30 min/Ar	99.1	2–3
ZrB_2–4 wt% $MoSi_2$	Ball-milled	2250 °C/120 min/Ar	97.7	3–11
ZrB_2–10 vol% $ZrSi_2$	Ball-milled	1650 °C/60 min/Ar	95.7	–
ZrB_2–20–40 vol% $ZrSi_2$	Ball-milled	1650 °C/60 min/Ar	>99	–
ZrB_2–4 wt% B_4C	Attrition-milled	1850 °C/60 min/vacuum	>98	12
ZrB_2–4 wt% B_4C	None	2050 °C/240 min/vacuum	~97	5–6
ZrB_2–4 wt% WC	Attrition-milled	2050 °C/240 min/vacuum	95	–
ZrB_2–2 vol% WC	Attrition-milled	2150 °C/540 min/He	98	9
ZrB_2–1.7 wt% C	Attrition-milled	1900 °C/120 min/Ar	>99	14
ZrB_2–4 wt% B_4C	None	2050 °C/120 min/Ar	94	6
ZrB_2–4 wt% B_4C	Attrition-milled	1850 °C/120 min/Ar	100	8
ZrB_2–4 wt% B_4C–0.5 wt% C	Attrition-milled	1850 °C/120 min/Ar	>99	<4
ZrB_2–2 wt% B_4C–0.5 wt% C	None	1900 °C/120 min/Ar	100	4

As a result, the addition of Mo activates diffusion processes during sintering, effectively promoting densification. This densification behaviour of Mo is also found in ZrB_2–20 wt% SiC mixture powder that could be sintered without pressure to a relative density exceeding 97.7% at 2250 °C for 120 min when 4 wt% Mo was added. Other studies found that the addition of 20 vol% $MoSi_2$ produced the almost fully densified ZrB_2 at 1850 °C for 30 min without external pressure. Furthermore, the addition of $\geq$ 20 vol% $ZrSi_2$ further reduced the densification temperature; the full density, greater than 99,5 g/cm^3 was obtained at 1650 °C for 60 min under vacuum of ~7.0 x 10^{-3} Pa. While more than 30 vol% $ZrSi_2$ decreased the elastic properties. The shear modulus and Young's modulus lowered with increasing $ZrSi_2$ amount because of the lower modulus of $ZrSi_2$ phase than those of ZrB_2 one. One exception was a lower shear modulus and Young's modulus for the composition with less $ZrSi_2$ (10 vol%) than those of 20 vol% and 30 vol%, as a result of the

presence of pores (~ 4 vol.%) because the porosity led to the decrease of both the moduli. It is common for SiO_2 and B_2O_3 films to be present on the surfaces of the starting $ZrSi_2$ and ZrB_2 powder, respectively. It is known that the SiO_2 reacts with B_2O_3 to produce an intergranular liquid phase at a high temperature (below 1500 °C). Improvement of densification due to the presence of intergranular liquid phase is documented in the literature. It could be concluded that the presence of intergranular liquid phase favours the process of grain rearrangement as well as improves the packing density of particles, and removes the oxide species from the surface of HfB_2 particles [17].

Differing from the previously mentioned liquid phase formers, reactive agents act as densification aids by reacting with the oxide impurities present on the surface of starting particles (such as ZrO_2 and B_2O_3) which inhibit densification [4]. Different studied was realized about solid solutions between ZrB_2 and other transition metal borides, which are another possible route to improve densification. The results indicate that ZrB_2 can form solid solutions with Ti, Hf, Nb, Ta, and Mo borides over a wide range of compositions. ZrB_2–B_4C mixtures containing 20–40 vol% B_4C were sintered to ~93% of their theoretical density, although the mechanism of the improved densification was not reported [19].

It was showed [7] that B_4C–ZrB_2 composites could be pressureless sintered via a reaction-based process by adding yttria-stabilized zirconia (YSZ) to B_4C. Additions of 30 wt% YSZ to B_4C produced ZrB2– B_4C composites with relative densities of ~98% after pressureless sintering at 2160°C. The authors suggested that incorporation of Y^{3+} into the ZrB2 lattice increased the diffusion rates within the system and enabled densification.

The main reactive agents used recently include B_4C, [19] and [29] C, [5] and/or WC [7] and [19]. It was found that the addition of 4 wt% B_4C produces almost the fully dense ZrB_2 compact at 1850 °C for 60 min in vacuum for attrition-milled powder, without externally applied pressure [19]. In contrast ZrB_2 containing only 4 wt% WC could be sintered to a relative density of ~95% at 2050 °C for 240 min. Chamberlain et al. [7] also showed that the introduction of WC (~2 vol%) allows sintering ZrB_2 powder to an almost fully densified state at 2150 °C for 180 min. They showed that elimination of oxide impurities on ZrB_2 particles surface by the reactions of B_4C or WC with ZrO_2 was the key to densification. The above-mentioned reactions are thermodynamically favourable at a temperature ≥1200 °C for B_4C, but >1500 °C for WC. As a result, the discrepancy in densification temperature between the two agent-doped ZrB_2 ceramics is likely associated with their different onset temperatures for the reactions.

Moreover, grain size measurement showed that excess B_4C restricts the grain growth during sintering. A similar densification and grain growth inhibition effect of B_4C was also reported in

ZrB$_2$-containing B$_4$C and carbon, either alone or in combination [29]. In addition, the densification effect of B$_4$C depended on the starting ZrB$_2$ powder size [29] ZrB$_2$ with a particle size of ~2 μm allows sintering to a density of ~95% at 2050 °C for 120 min. For comparison, ZrB$_2$ could be achieved with full densification at 1850 °C for 60 min when the particle size was reduced to ~0.5 μm by an attrition milling. Furthermore, the densification is more effective for a combination of B$_4$C and C than for B$_4$C alone. Using a combination of B$_4$C and C, the same ZrB$_2$ powder (~2 μm) could be sintered to almost full density at 1900 °C for 120 min. However, the additional densification effect of carbon does not appear in the reduced particle size ZrB$_2$ powder (~0.5 μm), which could be sintered to a full density at 1850 °C for 60 min using either B$_4$C or a combination of B$_4$C and carbon.

Mishra and Das reported enhanced densification of ZrB$_2$ produced by self-propagating high temperature synthesis with 5 wt% carbon powder as a sintering aid [30]. However, the density of the sintered ceramic was 5.138 g/cm^3, which was only ~92% dense based on a theoretical density of 5.6 g/cm^3 calculated for ZrB$_2$ (6.1 g/cm^3) containing 12.3 vol% (5 wt%) carbon (2.3 g/cm^3). Carbon is known to be an effective sintering aid for other nonoxide ceramics, although its beneficial role is not fully understood [11].

3.2 SINTERING

Sintering may be considered the process by which an assembly of particles, compacted under pressure or simply confined in a container, chemically bond themselves into a coherent body under the influence of an elevated temperature. The driving force for solid state sintering is the excess surface free Energy that occurs by reducing total surface and substitution of solid/gas interface, with the less energetic interface of solid/solid. Sintering is a complex process and for any given material and set of sintering conditions there are likely to be different stages, driving forces and material transport mechanisms associated with the process. Various stages of sintering can be grouped in the following sequence:

1. Initial bonding among particles;
2. Neck growth;
3. Pore channel closure;
4. Pore rounding;
5. Densification or pore shrinkage:
6. Pore coarsening.

An initial stage during which two particles in contact are joined, resulting in a neck joint, by diffusion of atoms across the surface of contact, which then begins to grow, giving rise to a solid interconnected structure in which the pores continue to be interconnected too; at this stage there is a modest increase in the density, which passes from about 60 to 65%. An intermediate stage in which there is a contraction of the open pores and a slow growth of the grains; the density increases considerably to about 90%. A final stage during which the pores are first isolated and then eventually are eliminated and the grains are increased (regularly or abnormal).

Among various mechanisms evaporation and condensation, surface, grain boundary and volume diffusion and plastic deformation mechanisms are prevalent.

3.3 THERMODYNAMIC AND KINETIC CONSIDERATIONS

The kinetic of densification is related with the particles dimension, according to the equation (3.2)

$$d\rho/dt = \gamma_s / d^3 kT [(F_b(\rho)D_b\delta_b / d)] + F_v(\rho)D_v \qquad (3.2)$$

Which γ_s is the surface energy, d the grain dimension, $D_b\delta_b$ the product between the thickness of the grain boundary and the diffusivity of the grain boundary, D_v the bulk diffusivity, F_b e F_v are functions of density ρ.

From this expression it results that, by decreasing the size of the grains with three orders of magnitude (from microns to nanometres), the speed of densification increases by 12 orders of magnitude.

The potential application of lower sintering temperatures involves different advantages, including:

- the lack of development of undesirable phase transformations;
- it is not necessary additives to promote densification;
- the opportunity to combine materials with different melting temperatures, such as metals and ceramics;
- a reduced waste of energy;

The use of high temperatures and long sintering times, may involve the growth of the grains in the microstructure. To prevent this, but preserving the properties of the nanostructure, there are some methods that allow operating a control on the microstructure, including:

- the dispersion in the starting material of a second phase particles, that limit the growth with a pinning process;

- an extremely rapid sintering, but it requires very homogeneous and dense green;

- the use of techniques that provide for the same time at high temperatures and also the intervention of high pressures, such as Spark Plasma Sintering, or by Sinter Forging;

- the use of sintering in two stages, known as Two Step Sintering [9].

Chamberlain et al. [7] also showed that the introduction of WC (~2 vol%) allows sintering ZrB_2 powder to an almost fully densified state at 2150 ºC for 180 min. They showed that elimination of oxide impurities on ZrB_2 particles surface by the reactions of B_4C or WC with ZrO_2 was the key to densification. Recently, Zhu et al.[5] coated a carbon layer surface of ZrB_2 particles using a phenolic resin as the carbon source. They found that the fully densified ZrB_2 compact could be sintered without pressure at 1900 ºC for 120 min, as the carbon content is more than 1.0 wt% in the coated ZrB_2 powders. For comparison, only a relative density of ~70% was obtained for the C-uncoated ZrB_2 powder under the same PS condition [4]. The Gibbs free energy of reaction between Zr and B to form ZrB_2 is −306 kJ/mol at 727 ºC and −280 kJ/mol at 1727 ºC, confirming the possibility of using Reactive Processing for the formation of bulk ZrB_2 [12].

ZrB_2–1.7 wt% C Attrition-milled 1900 ºC/120 min/Ar Final density >99 Grain size 14 µm

Over 1% of C the final density remains the same.

$$ZrO_2 + B_2O_3(l) + 5C = ZrB_2 + 5CO(g) \tag{3.3}$$
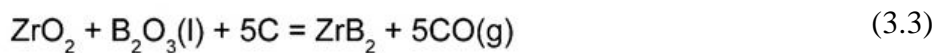
The reaction (3.3) is favourable above 1508 ºC in the standard state ($p_{CO} = 1.013{\times}10^5$ Pa), but becomes favourable at temperatures as low as 1035 ºC under mild vacuum ($p_{CO} = 13$ Pa).

Previous studies have shown that B_2O_3 liquid may evaporate by ~1450°C under mild vacuum. If B_2O_3 loss results in an excess of ZrO_2, based on the stoichiometry of reaction (3.3), then the residual ZrO_2 could react with carbon to form ZrC according to Reaction (3.4):

$$ZrO_2 + 3C = ZrC + 2CO \text{ (g)} \tag{3.4}$$

This reaction is thermodynamically favourable above 1166 ºC under 13 Pa pressure. If the oxides are not removed, they promote coarsening of ZrB_2 and, consequently, inhibit densification at higher temperatures.
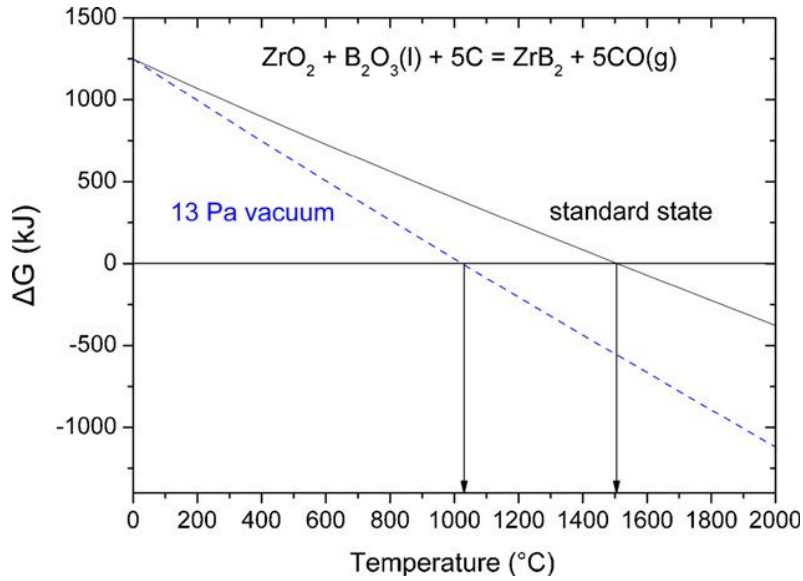
Fig. 3.2 The Gibbs' reaction free energy as a function of temperature for reaction (3.3);

Based on the combination of observations and previous results, the milled ZrB_2 specimens were sintered to near theoretical density due to the combined effects of the sintering aid (carbon) and the reduction of particle size. Abnormal grain growth was observed for the specimen sintered at 1900 °C with 1.0 wt% carbon. For the ZrB_2 ceramics sintered at 1900 °C, the Vickers' hardness decreased from 16.4 to 14.1 GPa when the amount of carbon increased from 1.0 to 3.4 wt%. The decrease in hardness could be attributed to the presence of a carbon-rich phase (shown in Fig. 5). Sakai et al. reported that carbon, heat treated at 1800–2300 °C, exhibited a low hardness with values in the range of 0.44–0.66 GPa. Therefore, the higher content of the softer, carbon-rich phase in the sintered ZrB_2 was regarded as the source of more severe plastic deformation during the indentation process, which resulted in a decreased hardness [5].

Below 1200 K, liquid B_2O_3 forms a continuous layer that wets the ZrO_2 and the underlying ZrB_2. The B_2O_3, layer acts as a barrier to oxygen diffusion resulting in passive oxidation of ZrB_2 and parabolic (diffusion-limited or $t^{1/2}$) oxidation kinetics. At intermediate temperatures (1200–1700 K), the rates of formation and volatilization of B_2O_3 (l) are similar, resulting in para-linear kinetics because of competition between mass gain (ZrO_2 and B_2O_3 formation) and mass loss (B_2O_3 vaporization). Above 1700 K, active oxidation with rapid linear kinetics has been attributed to loss of B_2O_3 (l) by evaporation, which leaves behind a porous, non-protective ZrO_2 (cr) layer.

Based on oxidation studies, the oxidation of ZrB_2 (cr) to ZrO_2 (cr) and B_2O_3 (l) by Eq. (3.5) was used to determine the equilibrium partial pressure of oxygen (p_{O_2}) for oxidation of ZrB_2.

$$ZrB_2 + 5/2\ O_2\ (g) \rightarrow ZrO_2 + B_2O_3\ (l) \qquad\qquad (3.5)$$
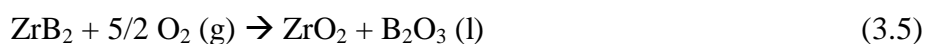
Tabulated data were used to calculate the change in Gibbs' free energy (ΔG^0_{rxn}) for Reaction (3.5) and for reactions that produced volatile species from ZrB_2 (cr) or from ZrO_2 (cr) and B_2O_3 (l). The ΔG^0_{rxn} values were converted to equilibrium constant (K_{eq}) values using Eq. (3.6), and then to equilibrium partial pressures using expressions for the equilibrium constant for each reaction such as the one presented as Eq. (3.7) for Reaction (3.5). Unit activity was assumed for all condensed phases. The results are reported as partial pressures (e.g., no units, assuming an ambient pressure of 1.013 x 10^5 Pa or 1 atm.). At 1800 K, the p_{O_2} calculated for the co-existence of ZrB_2 (cr), ZrO_2 (cr), and B_2O_3 (l) was 4.2 x 10^{-16} (vertical line in Fig. 3.3 (a)).

$$\Delta G^0_{rxn} = - RT \ln K_{eq} \tag{3.6}$$

where R is the ideal gas constant and T is the absolute temperature

$$K_{eq} = \frac{(a_{B_2O_3})(a_{ZrO_2})}{(a_{ZrB_2})(a_{O_2})^{5/2}} = \frac{1}{(pO_2)^{5/2}} \tag{3.7}$$

As p_{O_2} increases, the amount of B_2O_3 (g) should increase since O_2 is a reactant. This relationship can be seen in the portion of Fig. 1 to the left of the ZrB_2/ZrO_2–B_2O_3 line. Above the equilibrium p_{O_2} for Eq. (3.5), the gases are in equilibrium with ZrO_2 (cr) and B_2O_3 (l).
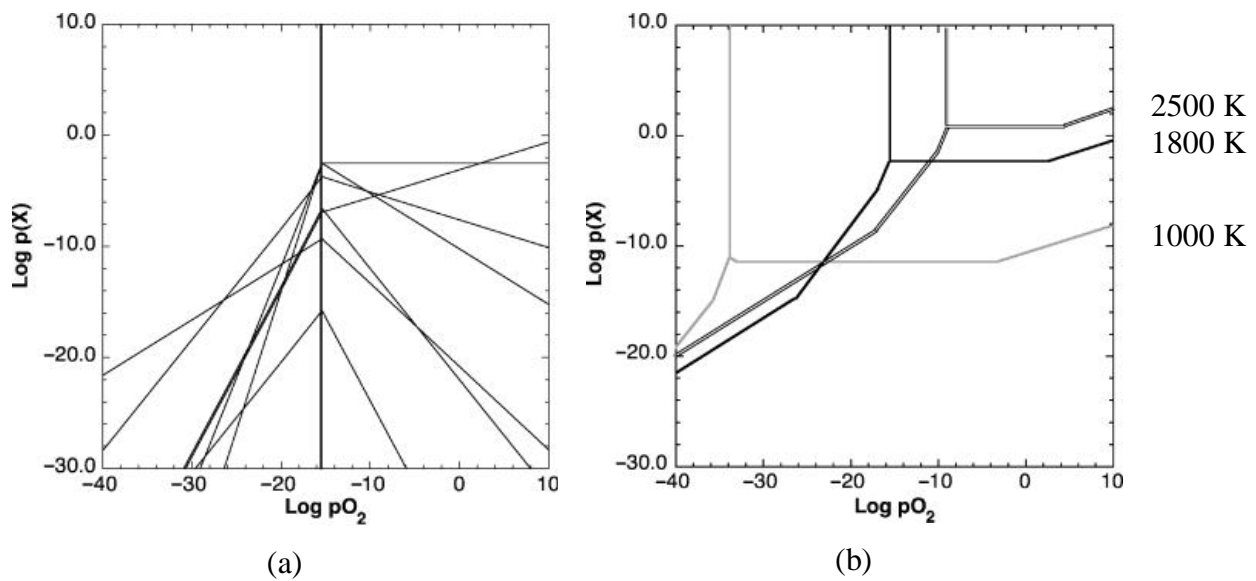

(a) (b)

Fig. 3.3 (a) Partial pressure of B species as a function of oxygen partial pressure at 1800 K, (b)The full volatility diagram for zirconium diboride (ZrB_2) at 1000, 1800, and 2500 K;

In this regime, B_2O_3 (g) forms by direct vaporization of B_2O_3 (l) according to Eq. (3.8).

$$B_2O_3 \text{ (l)} \rightarrow B_2O_3 \text{ (g)} \hspace{5cm} (3.8)$$

Because oxygen is neither consumed nor produced by Eq. (3.8), the partial pressure of B_2O_3 (g) does not vary with p_{O_2} (Fig. 3.3 (a)) in this regime. The pressures of Zr-containing gases were calculated, but not plotted since they were much lower than those of B species. The vapour pressures of all of the gases were calculated to compile a volatility diagram at three different temperature (Fig. 3.3 (b)). The system undergoes four major vapour transitions at 1800 K.

From the volatility calculations, the predominant vapour species at 1800 K in air was B_2O_3 (g) with a pressure of $\sim 10^{-2}$ (344 Pa). Two other species had vapour pressures predicted to be greater than 10^{-10} ($\sim 10^{-5}$ Pa) at 1800 K in air, BO_2 (g) at $\sim 10^{-3}$ (86 Pa), and BO (g) at $\sim 10^{-8}$ ($\sim 10^{-3}$ Pa).

Chapter 4

EXPERIMENTAL METHOD

4.1 MATERIALS AND METHODS

4.1.1   MIXING POWDER

The constituent raw materials must be adequately mixed and must have a sufficiently fine particle size to enable the ceramic mass to sintering at low temperatures. The powders must have a suitable particle size distribution, grain morphology and moisture content to allow an effective compaction during the pressing. It is a well-known fact that bulk ceramic preparation can be performed via a wet or dry process. As compared with the traditional wet powder preparation process, the advantages of the dry process are essentially the following:

- Lower energy costs, especially of heat energy;
- Elimination of the costs of deflocculant and additives to control the rheology of the slip produced by wet grinding;
- Lower machinery and equipment maintenance costs;
- Lower environmental impact of the production process;

The mixing was prepared with commercially available ZrB_2 powder (Grade B, ABCR, Karlsruhe, Germany) had a purity of 99% (metal basis), an average particle size of 2 mm, and a surface area of 0.9 m^2/g.). A percentage of 2 wt% of C was put in form of graphite (Synthetic, Sigma-Aldrich, Madrid, Spain). The first mixture of powder, that was not milled, was put in ethanol used as solvent. Then the solution was mixed mechanically with a magnetic stick on the bottom of the glass for 2 hours. At the third hour the heating was turned on, to evaporate all the ethanol. This process was useful to create a more homogeneous mixture, because is a problem to distribute the graphite in the not-milled powder.

It was used a vacuum bag to change the atmosphere before and after the milling, to limit the bad influence of ZrB_2 oxidation. Oxygen decreased the property of massive specimens, because during sintering, it develops a low density.

The powder was put in a vessel with a partial cover to prevent the possibility of losing powder during the process of change atmosphere, blew by the flux of Argon. The containers were put in a plastic bag, realized to change atmosphere;
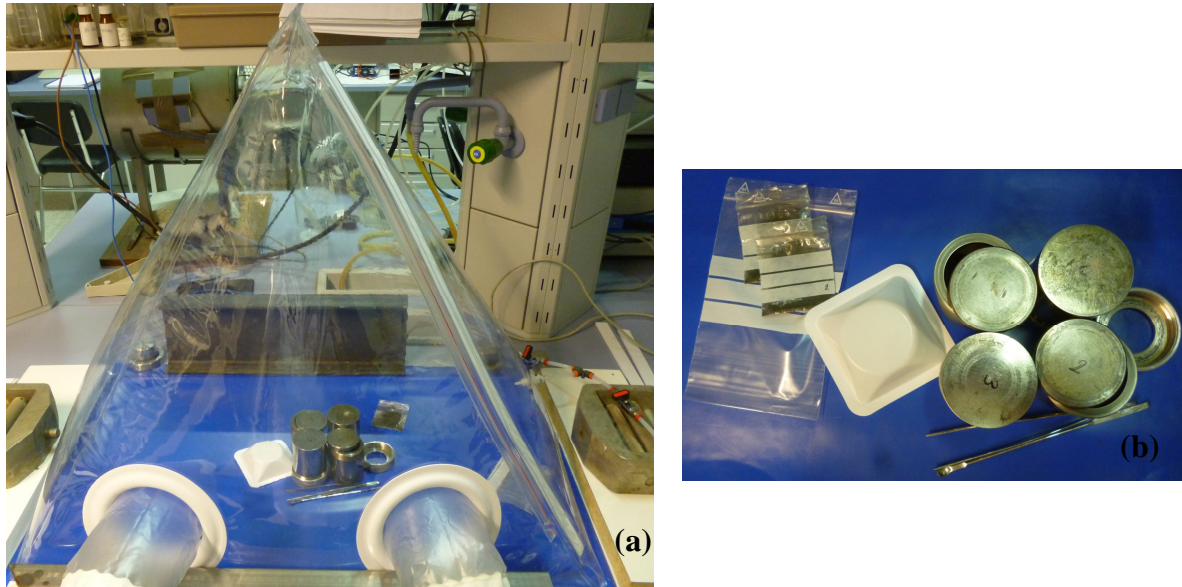

Fig. 4.1 Plastic bag used for the work in Argon atmosphere (a), with disposition of the bottle, tongs, spatulas, bowls and bags to contain the powders (b);

In the side of the bag, there is a valve connected with a circuit of vacuum pump, switched with a bomb of Ar (about 500 bar). The inside bag atmosphere would change in five steps (formed by made vacuum then blowing Ar), so to obtain a control atmosphere with a better purify degree. The best mode of disposition of the bottles, the bins, the instrument to remove the powders and the balls, in the bag was used to remove and change the air inside the bag (figure 4.1 (b)) There were gloves joined to the bag to handle the bottle inside. The bottle were closed inside the bag and than were taken to the milling machine.

The presence of Ar inside the containers is the better way to avoid an oxidation of the particles during the milling, when a higher temperature was reached, because the attrition between balls, and among powder and the inside surface of the bottle. Four vessels was charged, each filled with a charge of 3 grams, to get a final specimen of about 10 grams, and to spare time working in the same steps.

4.1.2 MILLING

Recently, it has been shown that high-energy ball-milling in dry conditions using shaker mills can refine the ZrB_2 powders to the nanoscale [8] and [11], something that conventional ball-milling cannot do. This is because the mechanism of crystal size refinement in ZrB_2 is brittle fracture, where the fracture strength scales inversely with the square root of the crystal size, and the compressive stresses generated during the high-energy ball-milling are high enough (i.e., GPa) to fracture fine particles. This refinement to the nanoscale offers unprecedented opportunities to enhance sintering kinetics immensely, as has been demonstrated lately [20].

The high-energy ball milling of ZrB_2 + 2 wt% of graphite powders was performed using a shaker mill (Spex D8000, Spex CertiPrep, Metuchen, NJ)

High energy ball milling

The 8000D Mixer/Mill is two-clamp laboratory mill for pulverizing hard, brittle samples in the 10-gram range. Functionally described as a shaker mill or a high-energy ball mill. It is capable of rapidly reducing solids to analytical fineness or blending a wide range of powders. With two clamps for increased throughput, also features a variable range electronic, timer, sleek, forced air cooling. The dual clamps of the Mixer/Mill move in balance, reducing vibration and extending the life of the mill's components. A fan keeps the motor and clamp mechanism cool during operation.

All the standard vials for grinding, typically have an internal volume of 50 to 60 ml with a grinding capacity of up to 25 ml and a blending capacity of up to 50 ml.
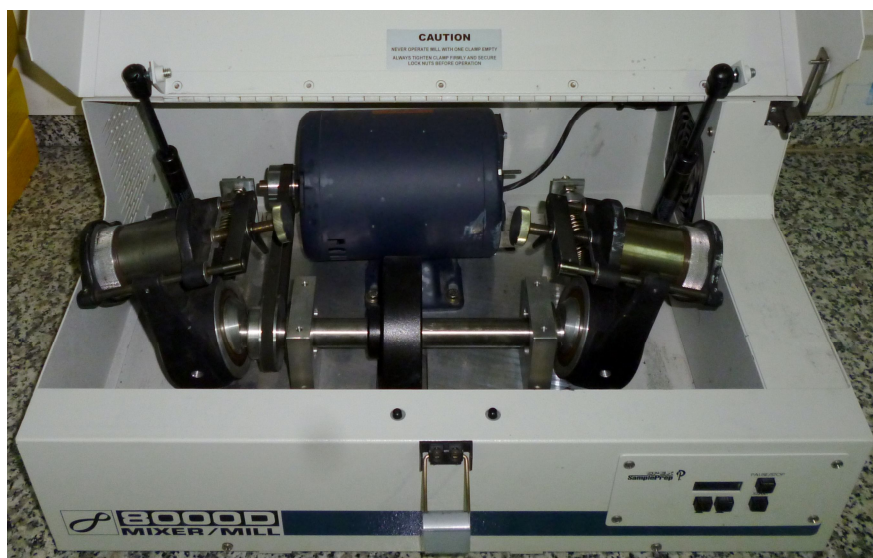

Fig. 4.2 High Energy Ball Milling machine (8000D Mixer/Mill) used for different times of grinding;

It is recommended that vials for this Mixer/Mill be purchased and used in pairs; when only one sample is being ground, the other vial should be clamped in place without sample or ball to maximize the balanced operation of the mill. The electronic timer displays the programmed running time; while the mill is operating, the timer also counts down the amount of time left in the run. The timer is factory-set for a maximum of 100 minutes, but this may be extended to 1000 minutes for special applications, like in this research. There is a safety interlock so that it cannot be operated with the lid open. Each clamp has a lock nut to prevent it from loosening, while the mill is running. The motor is also equipped with a thermal overload protector.

Operated at about 1060 back-and-forth cycles per minute. The milling was carried out in a cylindrical hardened-steel container with WC balls (each loaded with 5 WC/Co balls of 6.7 mm in diameter) in Ar, with different times of milling; respectively $1 \div 5 \div 10 \div 30 \div 60 \div 180$ minutes.

The milling was carried out by shaking the containers in a complex three-dimensional trajectory, under the following conditions: ball-to-powder weight ratio (termed the charge ratio hereafter) of 4, every charge with 3 grams of powder ($ZrB_2 = 2,94$ gr.; $C = 0,06$ gr.;),

The choice of 2 wt% (i.e., 5.12 vol%) graphite was because a previous study [5] has shown that this is the optimal concentration of carbon additive for the pressureless sintering of ball-milled ZrB_2 powders. More C can reduce the hardness. At this concentration, the undesirable surface oxides are removed completely, while grain coarsening during sintering is impeded. [11]
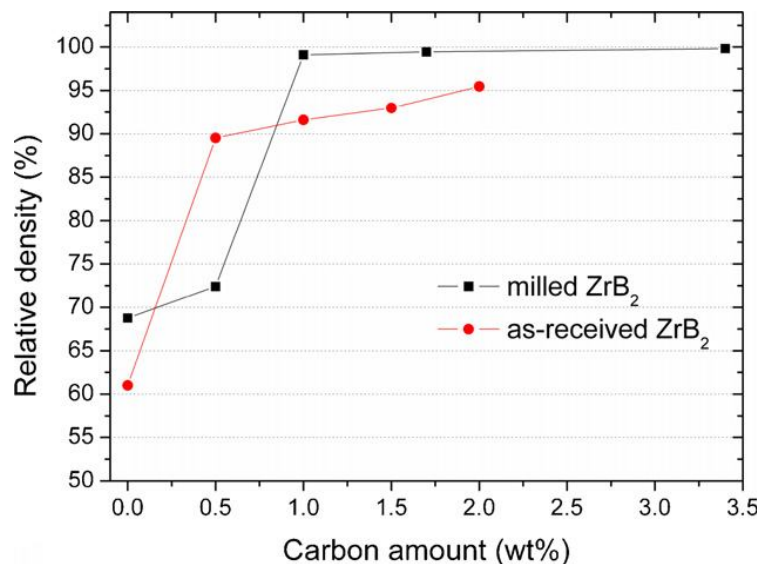

Fig. 4.3 The relative density of as-received and attrition milled ZrB_2 sintered at 1900 °C for 2 h as a function of the amount of carbon added [5];

The first round of milling was used to create a coat of powder on the internal surfaces of the containers and on the balls, moreover to remove possible residual powder of other type.

Every cleaning cycles were performed in proportional times of 1/3 of the relative time test cycle, for the powder dimension until 30'. Meanwhile for longer milling times (60 – 180 min), were realized cleaning cycles of 10 minutes.

Tough every time that the composition or size powder would change, the containers will be cleaned with ethanol (96%) and abrasive paper (P800). Certainly there are impurity cause those continuous cleaning. After grinding time, the extraction of the powder was done always in controlled atmosphere of Ar inside the bag. There was weighted and put in closed plastics bags.

4.1.3 SAMPLE PREPARATION

The preparation of specimens began extracting the powder from the vacuum bag. The biggest problem is the impossibility to produce samples in a controlled atmosphere; because the balances could not disconnected from the electrical line, also the vacuum bag was too little to contain the steel mould to be used in the uniaxial press. That is the reasons that the work executed over the nanopowders (above all smallest powder milled for 180') in Ar environment result not very useful.

Pressing consists of a compression of a powder or granules in a rigid matrix (uniaxial pressing) or in a flexible mould (isostatic pressing). Pressing is certainly the most widely used method for shaping ceramic pieces, because it allows the manufacture of relatively complex parts with tight dimensional tolerances and high productivity. Moreover, the later stages of drying and debinding, crucial in other shaping processes like injection and extrusion, are eliminated or at least simplified here. A broad range of ceramic pieces is produced by the pressing technique: tiles, plates, refractory materials, abrasives, cutting tools, as well as various electroceramic, magnetic and dielectric pieces. Uniaxial pressing in a metal matrix, with one (single effect) or two (double effect) pressing pistons, is used for the production of pieces whose thicknesses is higher than 0.5 mm, with a high surface/thickness ratio and exhibiting reliefs only in the pressing direction. Isostatic pressing in a flexible mould allows the manufacture of complex shapes with reliefs in three directions, as well as elongated shapes like tubes [25].

4.3.4.1 Uniaxial press

The weighted powder (around 6 gr. for specimens of 30', 60' and 180', and 10 gr. for specimens of 0', 1', 5', 10') was put in a tree part composed mould, of stainless steel, with diameter of 25 mm to obtain different heights respectively 4 mm and 7 mm. the reasons of this choice will be explicated in a second time.

The characteristics of the powder affect the filling of the mould, which must be complete, uniform and reproducible. This can be achieved with a good fluidity of powders or granules. The fluidity depends on the surface roughness of the powders, by the presence of sticky liquid on the surface (not in this case), and by the average size of particles. The roughness is lower if the granules are composed of very fine particles and there is no aggregation between large granules and finer granules. Sometimes just 5% of finer particles block the flow. Once introduced in the mould, the mixture is compressed and compacted. The compression of an unsaturated system of particles (that is when, the porosity is not completely filled by a fluid) is supported by the tension at the contact points between the particles, and the pressure P_f supported by the fluid present in the pores. Indicating the applied pressure P_a, the effective tension which acts on the solid is:

$$\sigma = P_a - P_f$$

However this tension must not be confused with the contact tension, σ_c, which acts on the particles in the areas where they touch each other, and that is proportional to the ratio At/Ac (A_t = area of the solid / A_c = effective area of contact) between the body section stressed and by the average of the contact area. In the early stages of compact process, the contact area is only a small fraction of the section on which acts the applied pressure. The stress of contact is therefore very high. The high value of σ_c can cause plastic deformation and/or fractures, which bring the particles to move and change shape, to occupy more efficiently the available volume, decreasing the ratio A_t/A_c and decreasing the contact tension. The compact degree increases with increasing pressure, but this will becomes little relevance to above about 50 MPa. At these pressures becomes important to instead the wear of the moulds. The industrial presses for forming ceramic techniques arrived to 100 MPa.

The uniaxial pressing process was realized with (manual Carver C press, p_{max}=1000 bar) a charge of 100 bar for time 180, 60, 30, 10, and 200 bar for time 5, 1, 0 minutes. It has two-column hydraulic press, it features adjustable daylight until ~45cm, steel construction for rigid precision and includes safety shield for operator protection. The charging time was of 1 minutes, than maintained for 1 minutes for 180, 60, 30, 10 and 2 minutes for 5,1,0 and released very slowly (about 3 minutes) to avoid deformations cause the release of tensions that could provoke fractures.

Fig. 4.4 (a) Uniaxial Carver C press, with mould of stainless steel; (b) phase of weighting of ZrB_2 before mixing;

The main problems that compromise the achievement of high density of the green during the consolidation phase are [9]:

- formation of agglomerates and subsequent formation of porosity;
- an increase of the friction forces between the nanoparticles and therefore difficult to slide inside the mould;
- high reactivity;
- ease of contamination;

It's important to clean the internal surfaces of the mould to prevent attrition with the powder during the extraction and limiting the possibly fractures that could be rise.

Part of the applied load at the time of pressing is transferred to the walls of the mould. The resisting force generated by friction on the walls produces gradients of pressure and density in the compact.

In the case of uniaxial pressing the shear stress average of the walls τ_p depends on the average pressure $\underline{P}$ applied according to the relation 4.1:

$$\tau_p = f\, K_{o/v}\, \underline{P} + A_p \qquad\qquad (4.1)$$

which f is the powder/matrix friction coefficient, $K_{o/v}$ is the ratio between the radial and vertical pressure, A_p is the adhesion force on the walls. The lubricant reduces f if it is present in the right quantity, while an excess ceases to be effective and in fact leads to an increase in the ratio $K_{o/v}$.

The average axial pressure P_h transmitted to the distance h, decreases as the distance from the punch. In the case where the pressure is exerted in one direction only (single action as in this case), it has, of a cylindrical mould of diameter D, it the depth h the axial pressure is

$$P_h = P_a\, exp[-(4f\, K_{o/v}\, H/D)] \qquad\qquad (4.2)$$

With the attainment of the minimum pressure at the opposite side of the cylinder, compared to that where the pressure is applied. Figure 5.27 schematizes the pressure profiles within a compressed piece starting from a non-granulated powder, for which particle mobility is low. The density gradients that result will therefore lead to differential shrinkages during sintering ("diabolo" effect in single effect pressing);
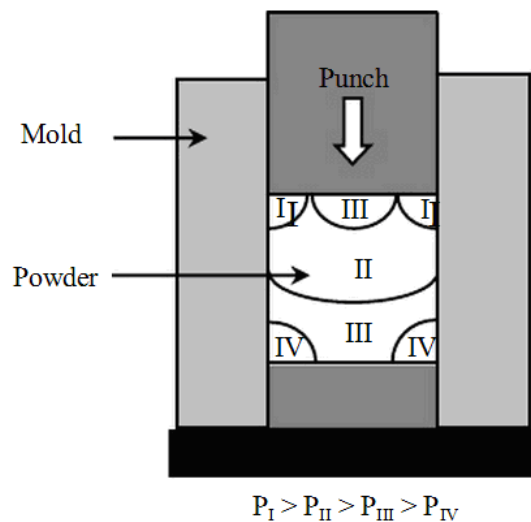

$$P_I > P_{II} > P_{III} > P_{IV}$$

Fig. 4.5 Pressure profile within a compressed piece starting from a non-granulated powder [25];

Pressure gradients result in density gradients and can pose serious problems both in the moulding process that in the subsequent processes. Generally, the problems of pressing are reduced if the density of the mixture in the mould, before pressing, is high. This is achieved with dense particles

or granules, and efficient packing after the filling. With increasing density as a result of compaction, the resistance of the product increases.

After the pressing cycle, the object must be removed from the mould. The elastic energy stored in the green part during compression leads to an expansion of the piece, called springback, at the time of ejection. The extraction is favoured if the elastic return of the product is greater than that of the mould, because it promotes the detachment of the object from the walls.

A considerable reduction of the force necessary for the extraction is given by the presence of lubricants in the mixture and on the walls of the mould, that also reduces the wear of the mould and the surface defects of the product. The defects are almost always generated, from the differential elastic behaviour at the time of extraction, which is in turn due to the pressure gradients in the compact, just discussed, in:

- Non-uniform elastic compression due to a non-uniform filling or presence of compressed air;
- Resistance extraction;
- Different elastic return portion between the extracted part and the part still in the mould;

A low speed was used to extract the specimens from the mould, to allow the green expansion without damaging it. The last process was done in air. Once extracts the green, due to the fragile consistency, it should be handle carefully to involve the samples with many plastic layers under vacuum. The procedure to prepare specimens consist of create little nylon bags, starting to cut and paste nylon sheets, by an induction heating machine. Than put the specimen in these bags. This delicate phase of the process is necessary before employ the isostatic press, because the porosity inside the greens, would be filled with water and the pressure could provoke its fracture. To shun risks of water absorption, the samples were packed with 4 layers of plastic.

4.3.4.2 Isostatic press

This pressing method offers the advantage of leading to a homogenous distribution of the pressure inside the piece and thus is also used to produce pieces requiring a high and very uniform green density (bearing and grinding balls, medical prostheses..). It was used an isostatic press (American Isostatic press, AIP 31260 $p_{max} \approx 400$ MPa). This unit is offered in full thread, pin closure, and breach lock closure.

The specimens were completely immersed into the chamber (7,5 cm diameter x 30,5 cm long) of the press, a security top was placed and was controlled that anyone could emerge from the surface.

After it, was closing the screw-cap and was set the necessary cycle pressure. Then was turned on the compressor and some seconds was taken to wait the completely extraction of the air from the idraulic circuit, afterward the last one was closed with a manual valve. At that moment, the compressor began to increase gradually the pressure until the set value. The analogical manometer detected the variations of pressure. With a manual valve could be exhausts the fluid from the pressure tank to the open circuit, with careful, to avoid fast variations of pressure that would cause damage to the pump. When the samples were extracted, the plastic bags were dried to avoid the damp of the green just product, and opened.

Fig. 4.6 American Isostatic press, AIP 31260;

The specimen could be put inside all together. The control of the pressure was carried out with a compressor with pressure of 350 MPa and time of 1 minutes for the specimens of 180, 60, 30, 10 minutes, instead 200 MPa for the specimens of 5, 1, 0 minutes.

At the end, the particles were cut in four pieces, to put then in a little crucible used in the furnace. (note about the brittleness of the specimens during the cutting: very brittle the 0' moulded. The 1', 5' moulded were just broken. From the 10' moulded and the other specimens, all were resistant.

The first problems were encountered in the creation of test specimens made with milled powders for 10 minutes or less. Unlike these, the specimens formed with powders milled for longer times, were

intact. The problem presented itself after the isostatic pressure. In fact, the powder did not compact enough to allow a sufficient resistance to keep them intact.

The main flaws encountered during pressing are the lamination perpendicular to the pressing direction and the rising of the upper part of the piece in contact with the piston (end capping). They are mainly due to the pressure gradients within the piece, the differential springback between the part outside the matrix and the part still stressed by the matrix during ejection, and the piece/matrix friction. The solutions consist of:

- increasing the ductile behaviour of the granules (plasticizer);
- reducing the piece/matrix friction (lubricant);
- increasing the mechanical strength of the green part (binder) [26].

The impossibility to introduce other component because the mixture has been chosen, the only parameters that remains were the pressure value, time of application, distribution of the powder inside the mould and piece/matrix friction.

Part of the problem has been solved by increasing the amount of powder only for the sample made with powders milled for less than 30 minutes, given the very thin thickness which characterized them, in addition to the lower resistance due to the higher porosity (like it could be seen in the data of relative densities in Table 5.2).

The other specimens (except the powder milled 10 min), did not resist the same pressure cycle, therefore, have been changed the process parameters, increasing the load of the uniaxial press, doubling the time and reducing the pressure in the isostatic, according to experimental tests carried out [5],[7],[12]. In fact equation (4.1) highlights that, the longer and narrower a part is along the pressing direction (high H/D), the less dense it will be. Uniaxial pressing is consequently restricted to the realization of pieces with a high surface/thickness ratio. That should be considerate when has been realized the greens part, with different quantity of powder, in the same mould. In this way only the powder that has not been ground, formed an intact specimens. Maybe due to the lowest packing property of a milled powder (smallest particles) and that the springback increases with the applied pressure [26].

The problem seems to be solved by limiting the friction during the procedure in the uniaxial press, cleaning the inner surface of the mould with isopropanol, after putting the powder which is inevitably deposited on it. Furthermore, it is necessary to distribute the powders inside the mould to form a top horizontal surface, to decrease the radial density gradient which can be created during the compression of the powders.

4.1.4   PRESSURELESS SINTERING

After pressing, many of the powder particles touch one another (Figure 4.7). During the initial sintering stage, necks form along the contact regions between adjacent particles; in addition, a grain boundary forms within each neck, and every interstice between particles becomes a pore (Figure 4.7 b). As sintering progresses, the pores become smaller and more spherical in shape (Figure 4.7 c).
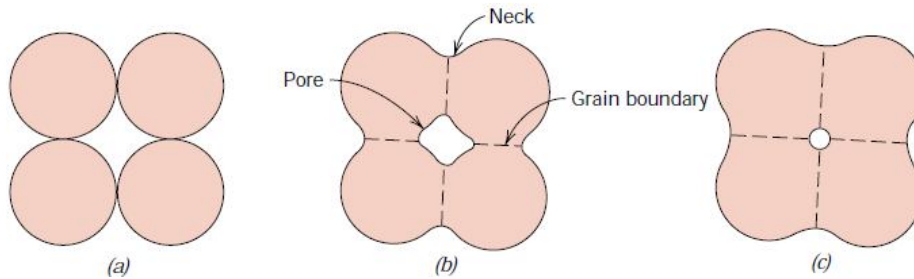

Fig. 4.7 For a powder compact, microstructural changes occur during sintering. (a) Powder particles after pressing; (b) Particle coalescence and pore formation as sintering begins; (c) As sintering proceeds, the pores change size and shape;

The driving force for sintering is the reduction in total particle surface area; surface energies are larger in magnitude than grain boundary energies. Sintering is carried out below the melting temperature so that a liquid phase is normally not present. Mass transport necessary to effect the changes shown in figure 4.7 is accomplished by atomic diffusion from the bulk particles to the neck regions [22].

The sintering of the specimens constituted by submicron powder, was tried in a high temperature furnace (Thermal Technology, Astro FP20-1000-3560) using different thermal cycle (with temperature from 1800°C until 2100°C).

This furnace is suitable for a wide variety of laboratory and small scale production applications, requiring very high temperatures. Temperatures up to 2500 °C may be achieved and can be maintained in ultra-high purity gas under ideal conditions. Typically, a furnace should be selected having a maximum temperature rating 200 °C higher than will be required for the maximum sustained operating temperature. This allows for heating element aging and other factors. Heating element life will be shortened at operating temperatures exceeding 2750°C.

The graphite hot zone includes the graphite furnace, support column and bracket, power supply and water-cooled flexible power leads. The operational specifications for these systems are as follows:

- The hot zone with high-density graphite resistance element, a thermal insulation zone of high-purity graphite felt retained by a solid-wall graphite tube.

- The furnace shell is either heavy-wall, seamless extruded 6061 T6 aluminium with an anodized interior and exterior or stainless steel (water-jacketed). The bulkheads are hard-anodized aluminium or nickel-plated copper (based on model) and the doors are nickel-plated copper. The shell and bulkheads have integral water-cooling passages so to maintain external surface temperatures at 65°C or less. The furnace has four 1 ⅛" - 16 radial and two axial threaded ports. One radial port is equipped with a 16mm diameter viewing port with an anti-fog gas diffuser. All other ports are plugged but will accept the addition of optional sight windows, thermocouples, pyrometers (like this furnace), feedthroughs, and valved adapters. Power connections are at one end of the furnace through radially mounted, water-cooled copper feedthroughs, providing unimpeded access to the bulkheads and doors. Electrical connection between the feedthroughs and the element is made by simple internal clamp connections. The hot zone has straight-through access for convenient loading from either end. Sight hearths in both ends of the furnace serve as thermal baffles and in the vertical position will support the work.

Operating environments are inert or optional dry reducing atmospheres with pressure capabilities to positive 103 kPa and full vacuum. Operating vacuums in the 0.13 range at temperatures to 2000 °C and in the 13 Pa range at 2300 °C can be achieved, but the vacuum pump only reached 75 x 10^3 Pa. At 1750°C a 50 mm long uniform temperature zone with a uniformity tolerance of ±3°C is possible. A uniformity tolerance of ± 8°C is possible over 100 mm. For this reason there was better to put the container of the green part, in the centre of the furnace. Uniformities will improve above 2000°C due to the high thermal radiation flux. Argon or helium is satisfactory as inert operating gases. Since helium is a better thermal conductor than argon or nitrogen, greater heat losses will occur when using helium. This means that more power must be used with helium to achieve a given temperature than with argon or nitrogen.

The power supply consists of an SCR power regulator and step-down load transformer. Power is activated with an On/Off switch that controls a furnace power contactor. A panel meter indicates secondary voltage and current. A safety interlock with warning lamp, audible alarm, and Operate/Reset switch monitors cooling water flow and optional alarm circuits. Power is manually adjustable too, from 0-100% by means of programmable controller (manual mode). Power supply components are housed in a floor console that shares a common 63,5 by 111.5 base with the furnace support column. Automatic temperature control may be achieved with a versatile, high stability, precision PID, set point programming controller.

Optical pyrometers are recommended for use at temperatures above the thermocouple range (up to 2000°C) and are effective from room temperature to 3000°C with controlled atmosphere conditions. A hearth elevator is available to facilitate bottom furnace loading. It permits smooth raising and lowering of the furnace bottom door and work support hearth.
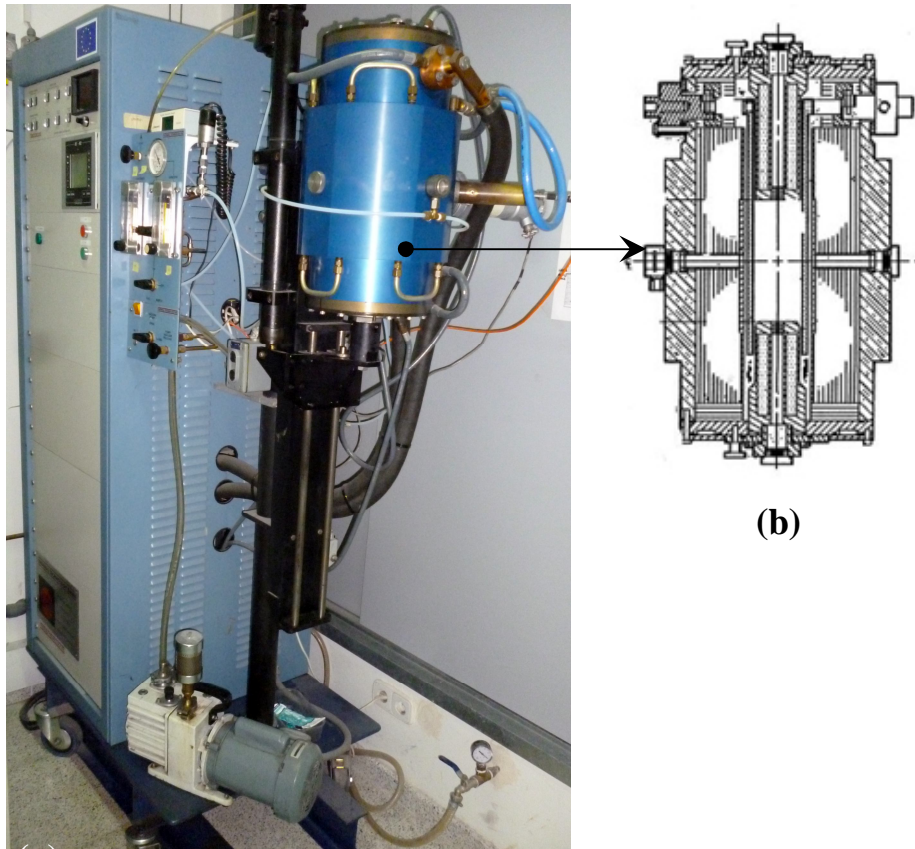

(b)

Fig. 4.8 Thermal Technology, Astro FP20-1000-3560 (a); scheme of the inside hot zone part (b);

The first step to use this furnace in graphite (with a maximum work temperature of 2600°C) is creating a program with temperature/time cycle.

Before heating, it was extract form the single green, 4 specimens. On the bottom of the crucible, there was located a graphite paper, to not contaminate the container. The 7 specimens, constituted by different time milled powder (0 – 1 – 5 – 10 – 30 – 60 – 180 minutes), were placed in a graphite crucible and was annotated their disposition, then was closed the top with a screw-cap. The furnace was prepared, placing a thin layer of grease around the board of the stopper, to ensure the inner atmosphere during the thermal cycle. The crucible was placed inside the furnace, at a height corresponding to the pyrometer, to be sure that the measured temperature would be the right one, in the centre of the crucible. Once sealed the pump, was generated a vacuum up to 750 mbar on the less.

To purge the atmosphere of the furnace was blown in Argon and then was created other time vacuum. This was repeated three times to owing a possible inert atmosphere, because it was not generated a high vacuum. This minimal limit of 750 mbar it is necessary to consent the evacuation of reaction products.

Fig 4.9 Controlled atmosphere system during sintering in the furnace;

The thermal cycle is formed by three steps of heating and maintaining the temperature, until a final uniformly decrease. A first heating is achieved with rate of 10°C/min, until 1450°C that is maintained for one hour. Follows a further increase in temperature that would arrive at 1650°C and it was held up for another hour. Then it changed the pressure, blowing into the furnace inert gas Argon at 4 bar. The control of inert gas flux was kept whit a system of different valves indicated in figure 4.9.

The valve of the vacuum pump has to be closed. Than has been opened the supply gas, with the line Ar valve and the bypass valve, to consent the escape. Another screw to bypass control the escape flux, and the more sensitive two valve regulated the entrance flux. A note about Argon: it

should not be used above 2100°C because of its potential to ionize and sometimes ionization can start as low as 1700°C. The last growing in temperature limit arrived at 1800°C, kept for one hour, after that cooling with a rate of 20°C/min till room temperature.

Other three thermal cycle was carried out, with the same parameters except for the higher temperature that arrived respectively until 1900 - 2000 - 2100°C, maintained for two hours before cooling till room temperature at the same rate.
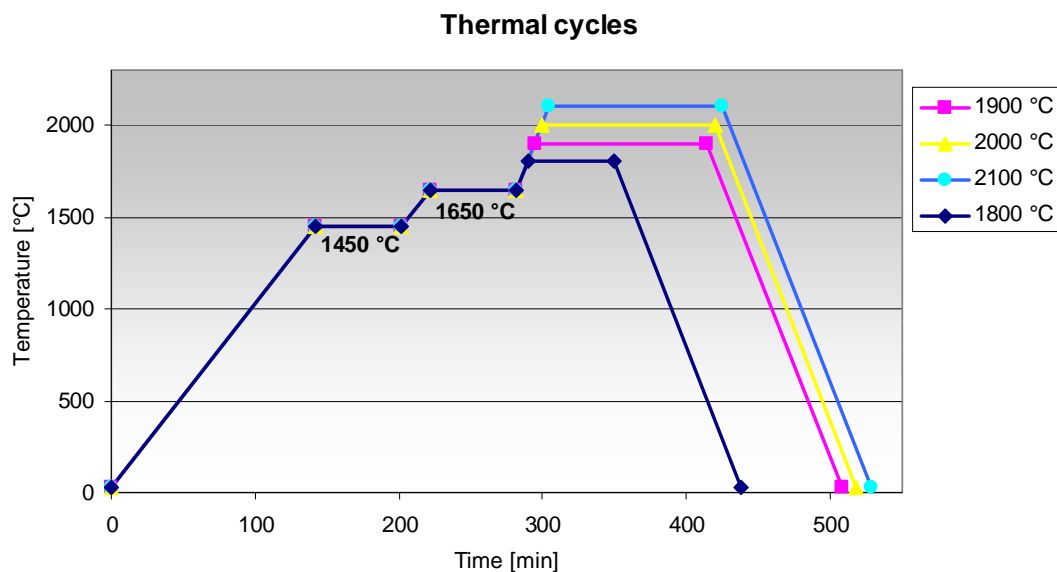
Thermal cycles

Fig. 4.10 Scheme of the used thermal cycles;

This thermal cycle was chosen, because different reasons: the first maintenance at 1450°C is necessary to permit the evaporation of CO from the reaction (4.2);

$$ZrO_2 + B_2O_3(l) + 5C = ZrB_2 + 5CO(g) \qquad (4.2)$$

The pressure adjusts the temperatures at which this reaction is thermodynamically favoured. This temperature has not been determined by observing any change in pressure during heating, because the scale of the manometer was not sufficiently sensitive to these measurements. In different studies [5], it is claimed that for pressures slightly lower than that applied in this study in the furnace (750 mbar) corresponded to a temperature of about 1400 °C. By reacting with carbon, the surface oxides were converted to very fine ZrB_2 particles and CO gas, which was readily removed by the vacuum. Powder compacts were heated in low vacuum up to 1650 °C to promote the volatilization and removal of B_2O_3 from the powder surface below 1750 °C where rapid coarsening

could occur. Moreover other previous studies have shown that B_2O_3 liquid may evaporate by ~1450 °C under mild vacuum [14]. The heating schedule included isothermal hold at 1650 °C, which was used to allow recovery of the pressure of 750 mbar in the furnace [5], [7]. Then the cycle will continue with inert gas Argon, to prevent or at least limiting the surface specimen's oxidation.

Chapter 5

RESULTS

5.1 CHARACTERIZATION

5.1.1 MEASURE OF DENSITY

Bulk density was determined using Archimedes' technique with distilled water as medium. Relative density was calculated by dividing the bulk density by the theoretical density.

It was employed a kit to be applied on the balance normally used for previous measurements.

The kit consists of: (Figure 5.1)

- Balance (Sartorius CP124 S);
- Base;
- Rotary support;
- Upper piece holder;
- Glass with distilled water;
- Thermometer;

Three weights are performed. The specimens was placed in an oven at 100 °C during one hour, (actually the specimens were just extract from the furnace) after the cooling they are placed in the upper jig for weighing. The following is carried out by immersing the piece in distilled water and the container was placed in a bell. There was generated vacuum to boiling the water and allow the complete filling of micropores with water. The job runs for 15' to about 800 bar. The container was placed on the base and was calibrated before the second weighing. Then the specimen was lying on the lower jig always immersed in water. In addiction, the water temperature was measured to obtain

the relative values of density as a function of the temperature. The third weighing in wet conditions was achieved by drying the surface of the specimen with a damp cloth, with the intent to remove only the excess water, but not extracting that present in the pores. Then it was weighted on the upper workpiece.

Once obtained the three weighs it is possible to calculate the density of the sintered specimens with the following relationship (5.1)

$$\rho_A = \frac{W_d \, x \, \rho_{H_2O}(T°)}{W_w - W_i} \qquad\qquad (5.1)$$

With ρ_A = absolute density of the sintered specimen;

W_d = dried specimens weight;

W_w = wet specimens;

W_i = weight of specimens in water;

Table 5.1 Data collected of absolute density with Archimedes' method for specimens sintered at (a) 1800°C, (b) 1900°C, (c) 2000°C, (d) 2100°C;

		0'	1'	5'	10'	30'	60'	180'
Weight [gr]	Dry	2,9211	2,4339	2,6999	2,4551	1,3948	1,6076	1,3905
	Immersion	2,4233	2,0059	2,2420	2,0418	1,1634	1,3413	1,1545
	Wet	3,1287	2,5894	2,8564	2,5808	1,4613	1,6878	1,5056
Temperature [°C]		15,5	15,0	15,5	15,8	16,5	16,5	16,5
Density [gr/cm^3]	$\rho_{o(H2O)}$	0,99905	0,99913	0,99905	0,99900	0,99889	0,99889	0,99889
	ρ_{oA}	4,1371	4,1676	4,3902	4,5504	4,6769	4,6344	3,9560

Table 5.1 (b)

		0'	1'	5'	10'	30'	60'	180'
Weight [gr]	Dry	2,2603	2,0201	2,5591	2,2568	1,5550	1,1415	1,1821
	Immersion	1,8725	1,6723	2,1153	1,8669	1,2915	0,9537	0,9836
	Wet	2,3678	2,1219	2,6573	2,3312	1,6089	1,1962	1,2626
Temperature [°C]		18,5	18,5	19,0	19,0	19,0	19,0	19,0
Density [gr/cm^3]	$\rho_{o(H2O)}$	0,99853	0,99853	0,99843	0,99843	0,99843	0,99843	0,99843
	ρ_{oA}	4,5568	4,4865	4,7142	4,8530	4,8915	4,6998	4,2303

Table 5.1 (c)

		0'	1'	5'	10'	30'	60'	180'
Weight [gr]	Dry	1,5629	1,3822	1,1996	2,3757	1,1384	1,3418	1,1495
	Immersion	1,2899	1,1429	0,9870	1,9640	0,9426	1,1166	0,9588
	Wet	1,6070	1,4201	1,2282	2,4275	1,1626	1,3820	1,1799
Temperature [°C]		19,5	19,5	19,5	19,5	19,5	19,5	19,5
Density [gr/cm^3]	$\rho_{o(H2O)}$	0,99833	0,99833	0,99833	0,99833	0,99833	0,99833	0,99833
	ρ_{oA}	4,9205	4,9780	4,9652	5,1170	5,1659	5,0473	5,1903

Table 5.1 (d)

		0'	1'	5'	10'	30'	60'	180'
Weight [gr]	Dry	1,1487	1,3282	1,5378	2,2547	1,3761	1,3049	1,2571
	Immersion	0,9379	1,0898	1,2532	1,8409	1,1269	1,0835	1,0424
	Wet	1,1594	1,3452	1,5436	2,2608	1,3794	1,3255	1,2612
Temperature [°C]			18,5	18,5	18,5	18,5	19,0	19,0
Density [gr/cm^3]	$\rho_{o(H2O)}$	0,99853	0,99853	0,99853	0,99853	0,99843	0,99843	0,99843
	ρ_{oA}	5,1784	5,1928	5,2877	5,3617	5,4413	5,3837	5,7364

The results obtained from measurements of density with Archimedes' method, shows that the absolute density of the specimens is increasing with the temperature used in the thermal cycles. To calculate the relative density it was compared with the theoretical density of 5,86 gr/cm^3 from other studies [11].

It can be seen in figure 5.2 that for every cycle, we obtain an increase in density, and the trend of the curve itself is maintained, except as regards the specimens of 180'.

Furthermore, after an increase of density, proportional to the grinding time until 30', there is a drop for the sample 180'. It could be due to the oxide layer that was formed on the powder surface, after the milling time, when extracted from the plastic bags to make a specimen by the uniaxial press. The high reactivity of this nano powder generates an amorphous oxides of ZrO_2 and B_2O_3, something located preferentially on the surface of the powder particles [20].

Table 5.2 Relative densities of all the specimens produced in the different thermal cycle;

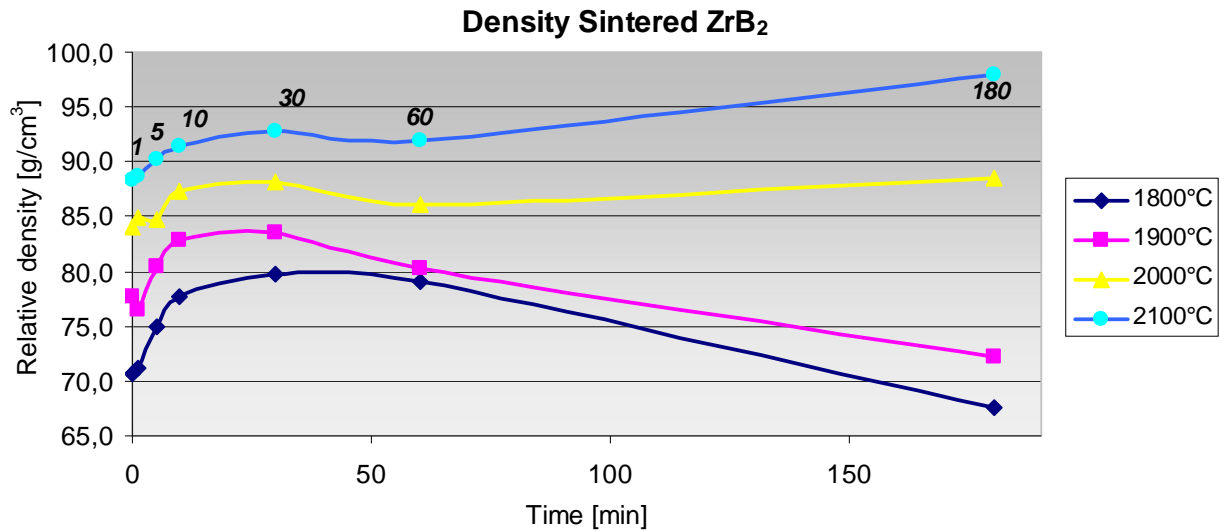| Temperature [°C]	0'	1'	5'	10'	30'	60'	180'
1800	70,6	71,1	74,9	77,7	79,8	79,1	67,5
1900	77,8	76,6	80,4	82,8	83,5	80,2	72,2
2000	84,0	84,9	84,7	87,3	88,2	86,1	88,6
2100	88,4	88,6	90,2	91,5	92,9	91,9	97,9

Fig. 5.2 Graph of absolute density for the specimens sintered at 1800 – 2100°C, as a function of milling time;

Other observations can be extrapolated from the graph in figure 5.3. It can be seen how the trend of the three types of powders changes. There is a linear trends for the 30' samples, while the specimen from 180' approached the reached maximum value. It could be possible to define it better, with a greater number of data, to improve the approximation of the curve. There is a contrasting data that regards the response to the first sintering step (the one which occurs at 1800°C). Only hypotheses can be developed given the lack of data about the concentration of powders. It is known the greater specific surface area of the 180' powders and as already said before, these have a greater reactivity. Therefore, the amount of oxygen (component that decreases the kinetics of diffusion in these conditions) present on the surface of the latter, is greater than the other 30' specimen. The data would be discordant on not grounded powders, if they had been preserved from the atmosphere before being used. In fact, these specimens were made with powders already oxidized, stored in not sealed containers.

The specimens with not milled powder reached only ~88% relative density after sintering at 2100°C, while the specimens ball milled for 180 minutes reached >98% relative density when sintered at the same temperature.

Accelerated electrons in a SEM carry significant amounts of kinetic energy, and this energy is dissipated as a variety of signals produced by electron-sample interactions when the incident electrons are decelerated in the solid sample.
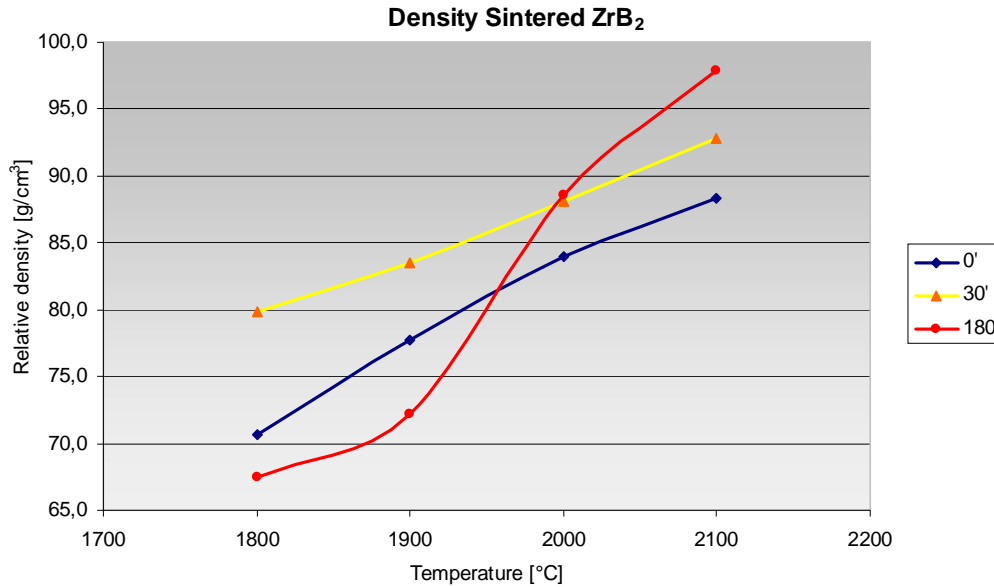
Fig 5.3 The relative density of milled ZrB_2 as a function of sintering temperature of different time milled powders;

5.1.2 SEM ANALYSIS

Microstructures were examined using scanning electron microscopy (S-3600N, Hitachi, Japan) with a voltage of 15 kW and ~80 mA of current intensity.

The scanning electron microscope (SEM) uses a focused beam of high-energy electrons to generate a variety of signals at the surface of solid specimens. The signals that derive from electron-sample interactions reveal information about the sample including external morphology (texture), chemical composition, crystalline structure and orientation of materials in the sample. In most applications, data are collected over a selected area of the surface of the sample, and a 2-dimensional image is generated that displays spatial variations in those properties. Areas ranging from approximately 1 cm to 5 microns in width can be imaged in a scanning mode using conventional SEM techniques (magnification ranging from 20X to approximately 30,000X, spatial resolution of 50 to 100 nm).

These signals include secondary electrons (that produce SEM images), backscattered electrons (BSE), diffracted backscattered electrons (EBSD that are used to determine crystal structures and orientations of minerals), photons (characteristic X-rays that are used for elemental analysis and continuum X-rays), visible light (cathodoluminescence-CL), and heat.

Fig. 5.4 A typical SEM instrument, showing the electron column, sample chamber, EDS detector, electronics console, and visual display monitors;

Secondary electrons and backscattered electrons are commonly used for imaging samples: secondary electrons are most valuable for showing morphology and topography on samples, this was the type of electrons used to show the fracture surface of the specimens. The electron gun at the top region of the SEM generates an electron beam. The gun mounted on the SEM used for the following analysis was a heated tungsten wire type. The gun is made up of a number of components.
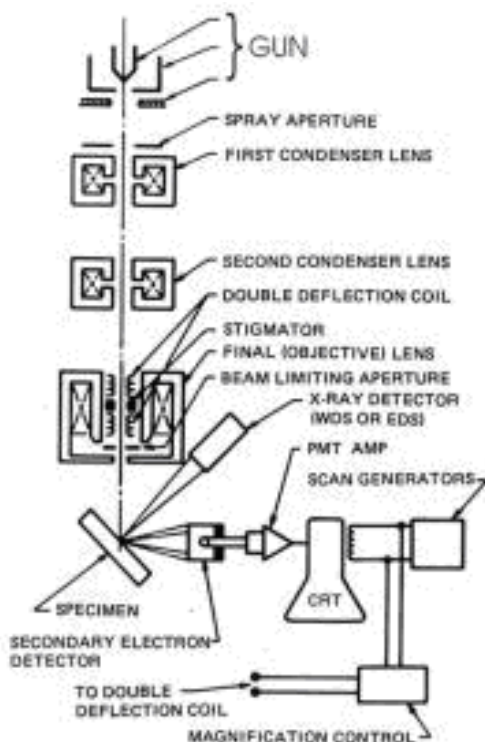
Essential components of all SEM's include the following:

- Electron Source ("Gun")
- Electron Lenses
- Sample Stage
- Detectors for all signals of interest
- Display / Data output devices
- Infrastructure Requirements:
  - Power Supply
  - Vacuum System
  - Cooling system
  - Vibration-free floor
  - Room free of ambient magnetic and electric fields

In the figure 5.5 the filament (also called emitter) is surrounded by the Wehnelt cylinder that closes over the filament assembly and has a small hole in the centre, through which the electrons exit. The electrode pins run to the filament through an insulator disc, and carry the current flow to the filament. An actual assembly, minus Wehnelt cap, is shown in the figure 5.5. Below the cap sits an anode, which, being positive, attracts the electrons away from the filament. If the filament is broken, the beam current will not increase on the SEM because no electrons can be produced.
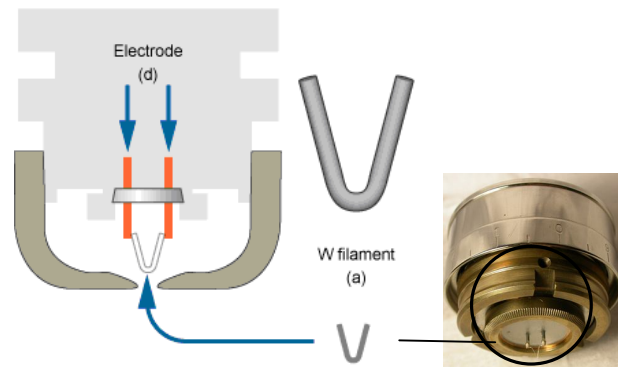
Fig. 5.5 shows the used filament type a) a tungsten (W) wire. The tip of a tungsten wire hairpin filament is about 10 µm in diameter;

Before the analysis at the scanning electron microscope, samples were prepared for SEM by cutting cross-sections perpendicular to the pellet face. It was obtained a fracture surface on the specimens in order to analyze the topography. The extracted assay was bonded via a platinum paste onto a metal support; ZrB_2 is a good conductor due to its structure, which shows hexagonal planes of B, like graphite, with the atoms of Zr interposed between them. It is a solid with high electrical conductivity, due to delocalization of p electrons on the lattice plane of graphite boride. The metal support was mounted on a jig with adjustable height. This allows a workpiece positioning to ensure a fix connection, during the automatic movement of the base under the electron beam, and a security distance from the internal part. After creating the vacuum in the observation chamber, it is possible to adjust the distance from the beam (to change the resolution, especially sensible at high magnifications) and adjust the intensity of the latter, to focus the image. This could be made automatically with the software that arrange the saturation, or could be made setting the different parameters (like the aperture of the beam, gun shift or tilt, stigmator, etc..). SEM's are comparatively easy to operate, with user-friendly "intuitive" interfaces, and rapid data acquisition. At the end it could be captured an image with high resolution, with data in digital formats, which

are highly portable. It have to take care at turning off the microscope, it is important to diminish slowly the voltage, to avoid the burning of the W filament.

5.1.3 OBSERVATIONS

The microscope analysis confirm the hypothetical meaning of the low density of the specimens. The macrostructure is really porous in the firsts specimens sintered at 1800 °C, which could be observed in the figure 5.7, only a begin of first sintering stage.

In the first stage the growth of the neck junction is due to a net transport of material towards the neck, determined by the particular shape of the surface. This is characterized by two radii of curvature, x/2 and P (figure 5.6) The difference pressure between the curved surface of the neck, determined by the value and the sign of P, and the convex surface of the particles (with radius R > 0), is due to the lower vapour pressure of the first surface and a higher concentration of vacancies as the second surface. The neck is thus, a sort of potential hole for atoms, and this motivates the transfer toward that.
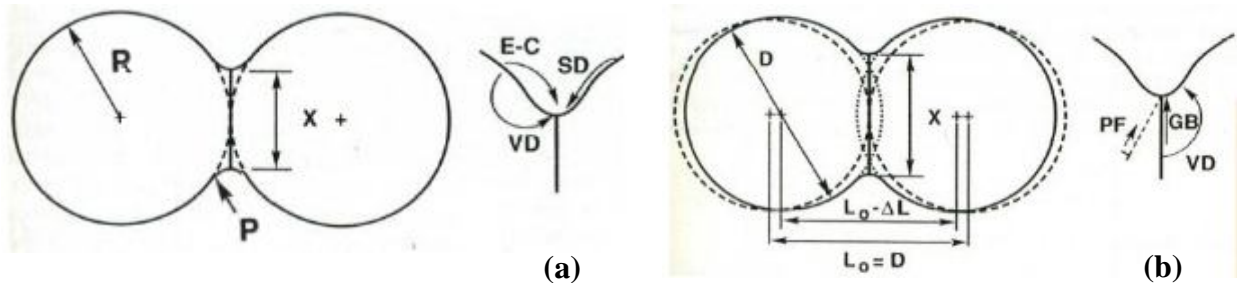

(a)   **(b)**

Fig. 5.6 Scheme of the first stage of sintering between two particles with different diffusion mechanism (a) Evaporation-condensation, surface diffusion, volume diffusion and (b) grain boundaries diffusion, volume diffusion, plastic flow;

Among the different mass transport mechanism, there could be seen some prevalent mode that do not get shrinkage or densification, called surface transport like in figure 5.6 (a). They do not lead to a reduction of porosity, but lead to a change in the shape of the pores and the reinforcement of the bond between the particles, expressed quantitatively with the increase of the ratio x/R. There is an interconnecting solid with edges in some particles except the 0' minute, where there are not edges. This shows the effect of the milling of fragile materials, where does not occur deformations, and in this case the fracture surface is intergranular.

The average size of the particles is lower than 5 μm in the 0' and 10' specimens, and the biggest are in specimen 30', while in the 180' there are the most interconnections and smallest grain sizes. In any case these microstructures will be useless to applications.
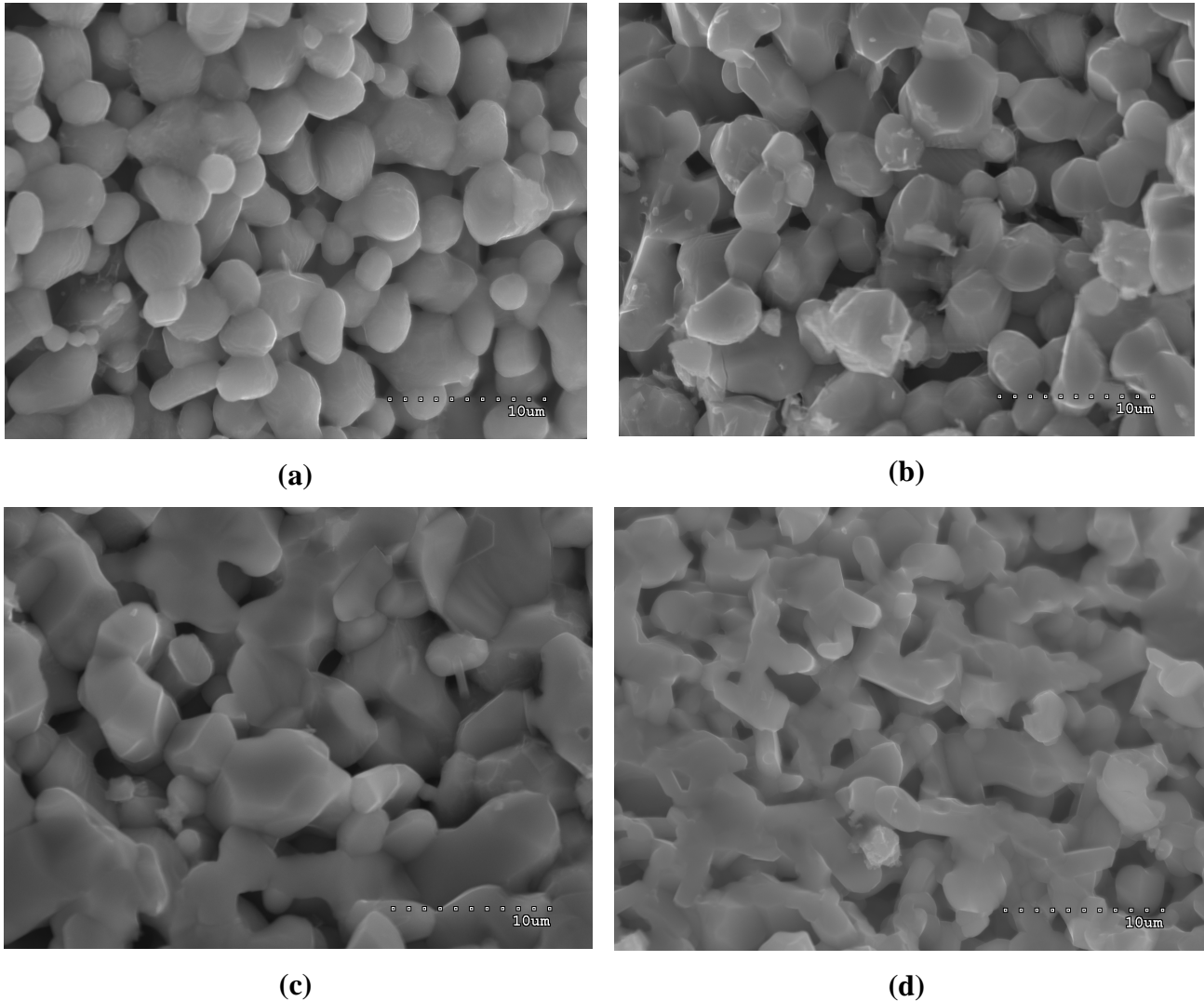

(a)

(b)

(c)

(d)

Fig. 5.7 Imagine obtained from SEM with secondary electrons, at 3500k, 0', 10', 30', 180' specimens respectively all sintered at 1800°C for one hour;

The next stage of the research was to extend the time for two hours and increase the highest temperature respectively till 1900 °C, 2000 °C, 2100 °C and the relative time of the thermal cycle for the duration of heating and warming; to obtain sufficient energy to activate different diffusion mechanisms or at least enhance diffusion, and consent a best sintering. The result of the last processes described could be seen in figure 5.8, where could got a bulk transport with evident densification of the material. New mass diffusion mechanisms were going on like grain boundary

diffusion and/or plastic flow and/or volume diffusion. The measure of density indicate an increase of ~5% from 1800°C to 1900°C, ~16% from 1900°C to 2000°C, ~9% from 2000°C to 2100°C;
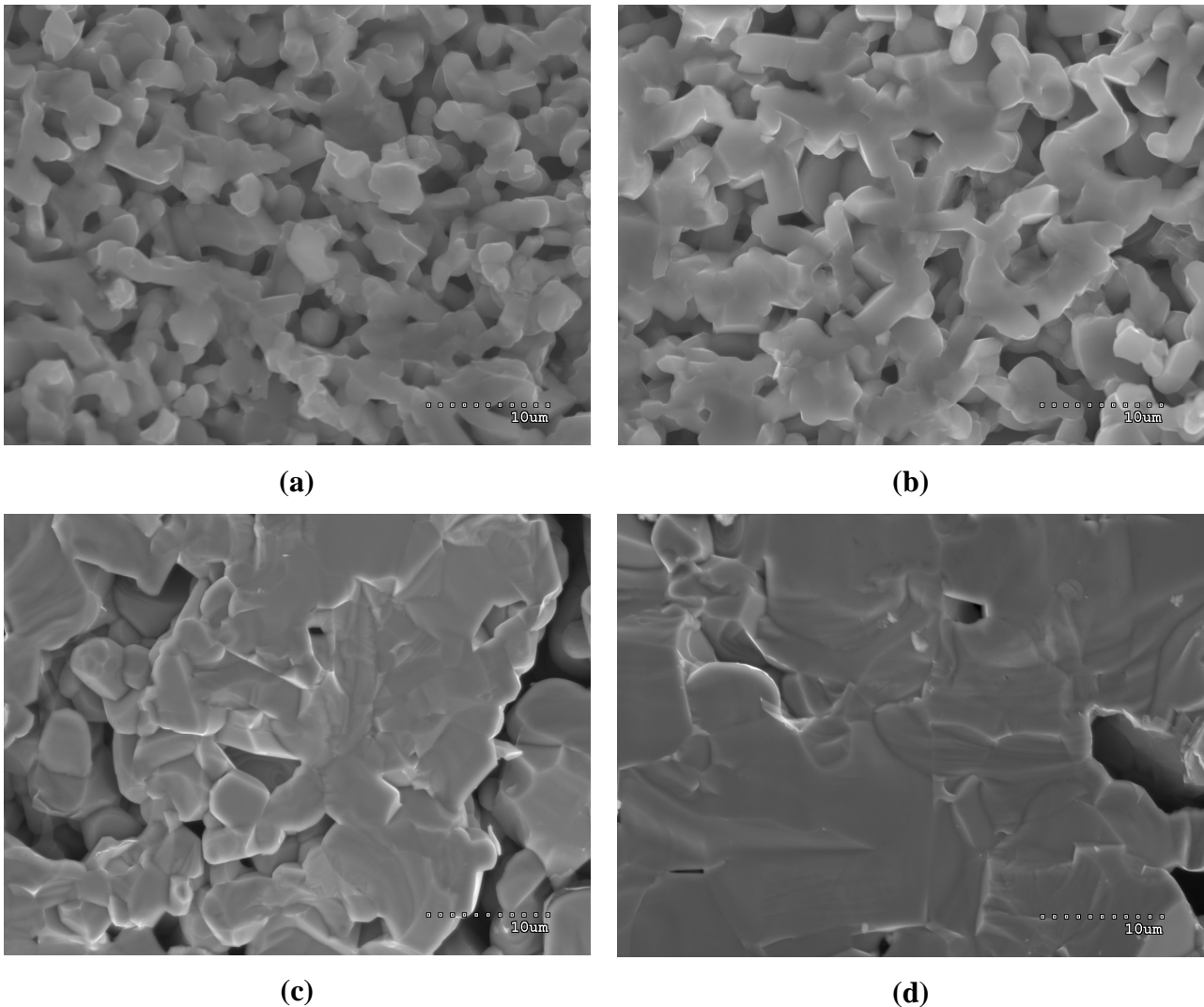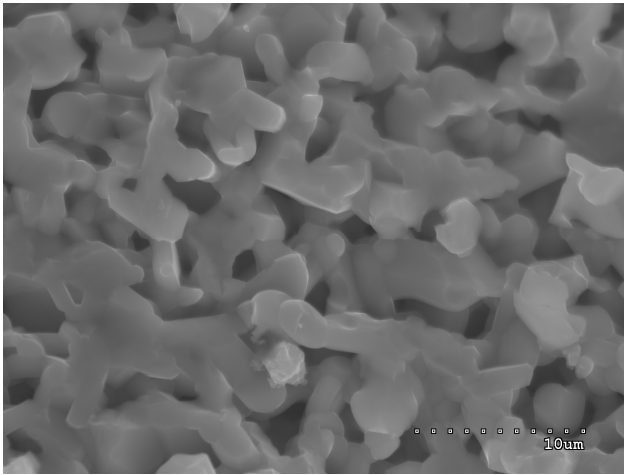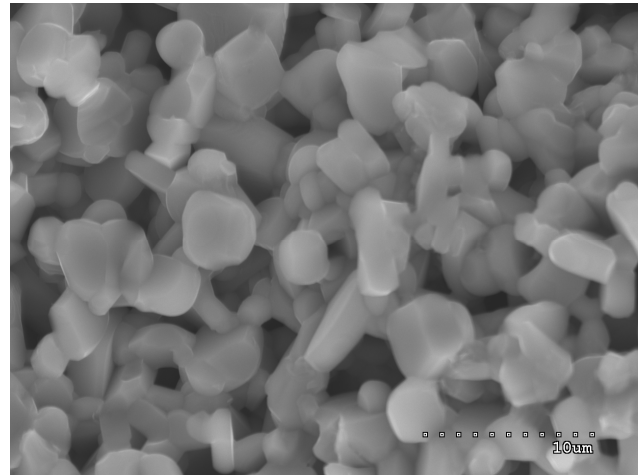

(a)

(b)

(c)

(d)

Fig. 5.8 Imagine obtained from SEM with secondary electrons, at 2700k, 180' specimens (a) one hour at 1800 °C; (b) two hours at 1900 °C; (c) two hours at 2000 °C, (d) two hours at 2100 °C;

In the images in figure 5.9 it could be seen a rounding of the particles from 1800 °C to 1900 °C. An increase of the grains by a maximum of 4 μm from the test at 1900 °C to apparent grains of about 10 μm of test at 2000 °C, up to the drastic reduction of the porosity in the test at 2100 °C. At 1900 °C it seems that the particles did not reach the interconnection phase, but which has been interrupted the sintering process only in the first phase; is interesting to see how it changes the fracture surface after reaching a certain degree of sintering.
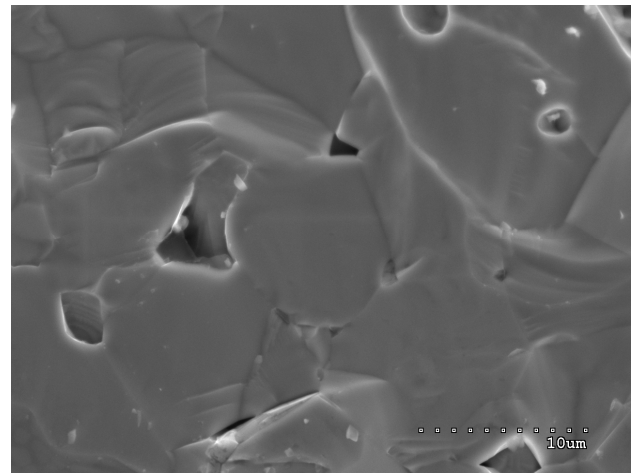
(a)　　　　　　　　　　　　　　　**(b)**

(c)　　　　　　　　　　　　　　　**(d)**
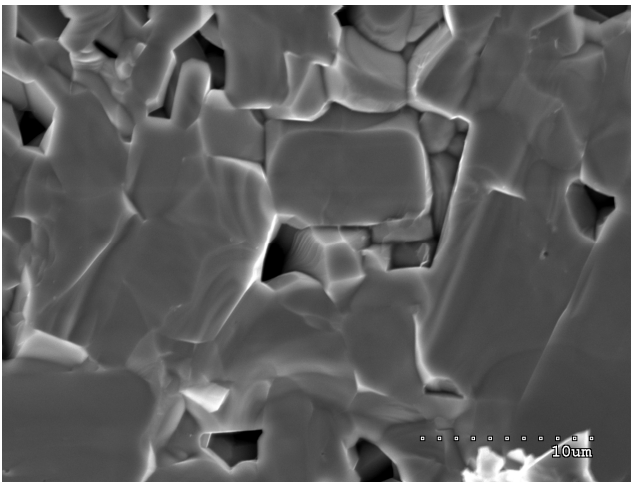
Fig. 5.9 Imagine obtained from SEM with secondary electrons, at 3500k, 180' specimens (a) one hour at 1800 °C; (b) two hours at 1900 °C; (c) two hours at 2000 °C, (d) two hours at 2100 °C;

In the sample sintered at 2100 °C it can be seen the intragranular fracture with evident narrow dislocations on the surface, while there is a typical intergranular fracture, in the figure 5.10 (a) that follows the profile of the grains.

In the ceramic materials with covalent bonds (highly directional), requires narrow dislocations and therefore, high resistance to their motion. In fact, the effort to move the dislocations is close to the ultimate strength for which a material of this type leads at failure in the elastic range, with a linear behaviour and complete absence of plasticity.

Sintering often reveals defects caused during the preceding stages, which are generally optimized with respect to sintering, which perfects them – for example, the granularity of the powders directly impacts on the densification and grain growth, so therefore the success of the powder treatment is

validated by the performances of the sintered part. The time required to obtain a given densification is proportional to the square of the radius of the particles in the case of transport from the surface to the neck and to the cube of the radius in the transport mechanisms that affect all the material volume. Therefore, the more the particles are small, the more rapid is the process of sintering.
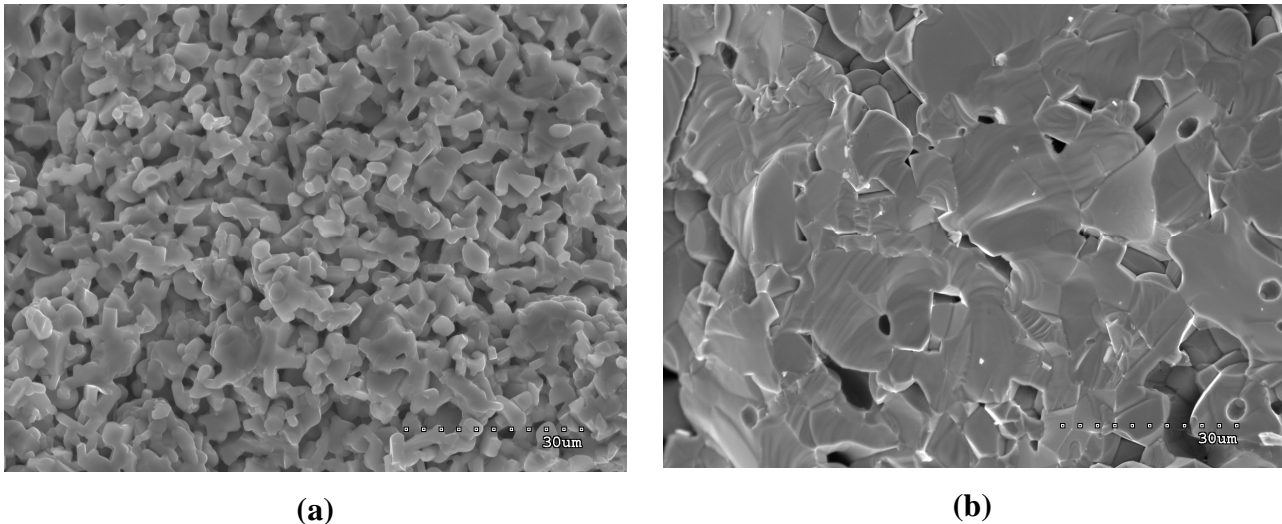

| (a) | (b) |

Fig. 5.10 Imagine obtained from SEM with secondary electrons, at 1200k, 180' specimens (a) two hours at 1900 °C; (b) two hours at 2100 °C;

In the second stage the pores decrease progressively in diameter, with the contribution of matter from the grain boundary towards the walls of the pores (and a reverse flow of vacancies). This process will self-accelerates, since the concentration gradient of vacancies between the grain boundary and the pore increases as the curvature of the pore itself (i.e. with decreasing the radius). However, the process not continues until the disappearance of the pores, because at one point, when the channels have become very long and narrow, the latter become unstable and generate a row of isolated pores, thus entering the last stage (it could happen at the specimen of 180' heated until 2000°C). In the third and final stage the pores are located in the solid matrix, like the 2100°C of 180' thermal cycle, the important mechanisms are the diffusion along the grain boundary and lattice diffusion through the grain boundary from the pore. The total elimination of the pores is not, however, granted. The pores may in fact become thermodynamically stable depending on whether the walls, concave or convex, (always for a matter of pressure gradient) and then by the number of grains surrounding the pore. The more the latter will be high, the greater the probability that the pore will swell and vice versa.

Chapter 6

CONCLUSIONS

Some considerations can be made concerning the response at high energy ball milling of the powders. The crystallite size refinement occurs with a repeated mechanism of brittle fracture, followed by cold welding that could be observed from experimental observations like the rapid refinement in the early stages of high energy ball milling, and the presence of a limiting crystallite size. Submicrometer porous agglomerates, contain nanometre-sized single crystals and nanopores. Also the final crystal size is limited, due to the fracture strength of ZrB_2 particles and the compressive stress generated by the balls collision.

Furthermore the powder takes faceted shape in the early stages of milling, observed in comparison of the not milled powder that has rounded geometry. In the interior of the crystals are not lattice microstrains, so the high energy ball milling rules out severe plastic deformation. In the late stages of milling, there are resistant agglomerates containing primary nano-particles. It is known that the size of agglomerates is determined by combined effect of the fracture rate and the cold-welding rate. The cold-welding rate increases, due to the increasing number of particles. As a result, the size of agglomerates increases and finally stabilizes until the ball-milling time beyond 10 min [11].

The measurement of the oxygen content in the milled powders in air, via high energy ball milling indicate that there is the double amount of oxygen, compared to other more conventional milling methods [7]. The X-ray analysis, including detailed Rietveld refinements, show that the oxygen retained does not form solid solutions, but amorphous oxides. The X-ray Photoemission Spectroscopy indicate that these oxides are amorphous ZrO_2 and B_2O_3 and that are located preferentially on the surface of the powder particles [20].

It was evaluated the efficacy of 2 wt% graphite as process control agent, for the comminution of ZrB_2, and can be drawn that it is not alter by graphite additions. The problem is that the refinement mechanism formed during ball milling, agglomerates comprising in single-crystal nanoparticles of 10 nm in average diameter.

In the first step of grinding, the process of powders refinement is slower in the presence of graphite, this is because the graphite may exert a lubricating action during the contact between particles of the powder and during the contact between the balls. However, the graphite does not affect the final average size of the crystals, since these are mainly due to the fracture strength of ZrB_2 and the compressive stress in the areas of collision.

Graphite is an effective process control agent for the milling of ZrB_2 which promotes the formation of finer particles (i.e. 50 vs. 120 nm) and evens out the average size of agglomerates (i.e., 122 vs. 143 nm) because the lubricant effect, reduces the cold welding of the first nano-particles and exposes the larger agglomerates to compression during the impact between themselves and between balls [21].

Satisfactory results were achieved from this study, with the higher relative density of 98% of the sintered nanopowder. The time required to obtain a certain densification is proportional to the square of the radius of the particles in the case of transport from the surface to the neck and to the cube of the radius in the transport mechanisms that affect all the material volume. However, the more small are the particles, the more rapid is the sintering process. From the expression (3.2) results that reducing the size of the grains of three orders of magnitude, the speed of densification increases by 12 orders of magnitude [9]. The effect of the extreme small size and large surface area, promotes on one hand the sintering process; but in the other hand, promotes the oxidation process and the possibility of contamination of the powders and secondly, in a significant way, the formation of agglomerates (because of the easy formation of bonds between particles of size truly reduced, by virtue of their high reactivity).

With the grinding of the powders in a controlled atmosphere has been halved the concentration of oxygen which binds to the surface during high energy ball milling. Obviously the next step of realization of the specimens from nanopowders, can be improved by realizing them also in a controlled atmosphere given the high reactivity of the massive product is lower compared to specimens made with powders of large size and lower percentage of oxygen.

Surely it is necessary to adjust the pressure during the use of uniaxial and the isostatic press. According to studies [7] the creation of specimens, is carried out by applying a pressure 6 times higher than 50 MPa used in this experimentation, while the isostatic pressure used was less than approximately 50-75 MPa. It has been noted that when slightly approaching this combination (applying 60 MPa on the uniaxial press and 200 MPa on the isostatic press), the green remained intact instead breaking in more points. It has been to remember that according the relationship (4.1) the longer and narrower a part is along the pressing direction (high H/D), the less dense it will be. And that influence the production of greens part, with different quantity of powder, using the same mould.

Without internal tension in the green, the product will be more homogeneous cause the decrease of density gradient after sintering.

An important factor, concerns the pressure used in the furnace. It could be seen that with a pressure of 13 Pa, instead of 75000 Pa, it would be able to lower the temperature of reaction to remove the

oxides of about 1100°C, according to thermodynamic theories about free energy. This would certainly give a contribution to diminish the sintering temperature/time, removing the element that has more influence on the diffusion kinetic: oxygen.

A problem to be solved is the lack of homogeneity of porosity between the nearest area to the surface and the core of the massive material. As is known, this is due to different factors:

- Uneven compression of the material in the press;

- Distribution of heat in the sintering furnace;

- Removal of reaction (oxides) products during sintering;

For the development of this experimental research, now that the first step of the massive production has been realized profitable, it would be necessary, as well as solve the problem listed above: a more detailed characterization of the sintered product with density of 98%, with an evaluation of purity degree to check especially the effectiveness of the additives for the removal of the oxygen present.

Based on the results, it could be adjust the additive amount or to change the distribution using an epoxy resin to pyrolyze, with the aim of homogenize the powder mixture. An evaluation of the oxidation resistance, (considering the type of porosity, interconnected or not), and at least a hardness test to evaluate the mechanical strength to start comparing the different existing production process.

The research is a constantly development, so many ways could be taken to improve and as always, it must be considered the cost factor, weighted with criteria, the most profitable way in terms of evolution of the project.

BIBLIOGRAPHY

[1] K. Upadhya, J. Yang, and W. Hoffman, *Materials for Ultrahigh Temperature Structural Applications*, Am. Ceram. Soc. Bull., 76 [12] 51–6 (1997).

[2] R. S. Averback, H.J. Hofler, R. Tao, *Processing of nanograined materials*. Materials Science and Engineering A, 166, 169-177, 1993.

[3] Wolfgang M. Sigmund et Al. *Novel Powder-Processing Methods for Advanced Ceramics*; J. Am. Ceram. Soc., 83 [7] 1557–74 (2000).

[4] Shu-Qi Guo. *Densification of ZrB$_2$-based composites and their mechanical and physical properties: A review*. Composites and Coatings Center, National Institute for Materials Science. (2008).

[5] Sumin Zhu, William G. Fahrenholtz, Gregory E. Hilmas, Shi C. Zhang. *Pressureless sintering of carbon-coated zirconium diboride powders*. Materials Science and Engineering A 459 (2007) 167–171.

[6] V. Milman, B. Winkler and M. J. Probert. *Stiffness and thermal expansion of ZrB$_2$: an ab initio study*. Journal of physics: Condensed matter. 17 (2005) 2233–2241.

[7] Adam L. Chamberlain, William G. Fahrenholtz, and Gregory E. Hilmas. *Pressureless Sintering of Zirconium Diboride.* J. Am. Ceram. Soc., 89 [2] 450–456 (2006).

[8] V. Zamora, A.L. Ortiz, F. Guiberteau, M. Nygren, L.L. Shawc. *On the crystallite size refinement of ZrB2 by high-energy ball-milling in the presence of SiC*. Journal of the European Ceramic Society 31 (2011) 2407–2414.

[9] F. Prete, A. Motori. *Sintesi e caratterizzazione di nano polveri composite Allumina-Zirconia*. Dottorato di ricerca in ingegneria dei materiali, Università di Bologna. (2010).

[10] C. Jariwala, A. Chainani et Al. *Comparative study of the electronic structure of MgB$_2$ and ZrB$_2$*. Physical review B 68, 174506 (2003).

[11] Carlos A. Galán, Angel L. Ortiz, Fernando Guiberteau, Leon L. Shaw. High-*Energy Ball Milling of ZrB$_2$ in the Presence of Graphite*. J. Am. Ceram. Soc., 93 [10] 3072–3075 (2010).

[12] M. Brochu, B.D. Gauntt, L. Boyer, R.E. Loehman. *Pressureless reactive sintering of ZrB$_2$ ceramic*. Journal of the European Ceramic Society 29 (2009) 1493–1499.

[13] Hongzhi Fu, Ying Lu, Wenfang Liu, Tao Gao. *Pressure effects on elastic and thermodynamic properties of ZrB$_2$*. J Mater Sci (2009) 44:5618–5626.

[14] William G. Fahrenholtz. *The ZrB$_2$ Volatility Diagram.* J. Am. Ceram. Soc., 88 [12] 3509–3512 (2005).

[15] Hui Li & Co. *Crystal structure and elastic properties of ZrB compared with ZrB₂: A first-principles study*. Computational Materials Science 49 (2010) 814–819.

[16] R. Telle, L.S. Sigl, K. Takagi, R. Riedel (Ed.). *Handbook of Ceramic Hard Materials*, Wiley-VCH, Weinheim, Germany, 2000, pp. 802–945.

[17] Guo, S. Q., Kagawa,Y., Nishimura, T. andTanaka, H., *Pressureless-sintering and physical properties of ZrB₂-based composites with ZrSi₂ additive*. Scripta Mater., (2008) 58(7), 579–582.

[18] P. Greil, *Advanced materials progress report on Advanced engineering ceramics*. Progress report. Adv Mater. (2002), 14, N°10, May 17.

[19] S. C. Zhang, G. E. Hilmas, and W. G. Fahrenholtz, *Pressureless Densification of Zirconium Diboride with Boron Carbide Additions*. Department of Materials Science and Engineering, University of Missouri-Rolla, Rolla, Missouri 65409.

[20] Angel L. Ortiz, Victor Zamora, Fernando Rodriguez-Rojas, *A study of the oxidation of ZrB₂ powders during high-energy ball-milling in air*. Department of Mechanical, Energy, and Materials Engineering, University of Extremadura, 06006 Badajoz, Spain. 21 November 2011.

[21] M.L.Muolo, L.Morbelli, E.Ferrera, M.Bassoli, C.Bottino and A.Passerone, *Interfacial Morfology and Wetting in the ZrB₂/Ag-X (X=Cu, Ti, Zr) System*. Proc. 6th International Conference on Joining Ceramics, Glass and Metal, pg.238-245, 30 Sept-1Oct 2002, Munich, Germany.

[22] W. D. Callister. *Synthesis, Fabrication, and Processing of Material*. S-148, Fundamentals of Materials Science and Engineering, Chapter 14.

[23] E. Rudy, St. Windisch, *Ternary phase equilibria in transition metal-boron-carbon-silicon systems*. Part II, Volume XIII, Phase Diagrams of the system Zr-B-C.

[24] H. Gleiter, *Nanostructured materials: state of the art and perspectives*, Nanostructured Materials, 6, 3-14, 1995.

[25] P. Boch, A. Leriche. *Sintering and microstructure of ceramics*. Ceramic materials, Chapter 3.1.

[26] T. Chartier. *Pressing*. Ceramic materials, Chapter 5.5.

[27] Adam L. Chamberlain, William G. Fahrenholtz, et Al. *High-Strength Zirconium Diboride-Based Ceramics*. J. Am. Ceram. Soc., 87 [6] 1170–1172 (2004).

[28] J.J. Meléndez-Martinez, A. Dominguez-Rodriguez, F. Monteverde, el Al. *Characterisation and high temperature mechanical properties of zirconium boride-based materials*. Journal of the European Ceramic Society 22 (2002) 2543–2549.

[29] William G. Fahrenholtz, Gregory E. Hilmas, Shi C. Zhang, and Sumin Zhu. *Pressureless Sintering of Zirconium Diboride: Particle Size and Additive Effects*. J. Am. Ceram. Soc., 91 [5] 1398–1404 (2008).

[30] S.K. Mishra, S.K. Das, *Sintering and microstructural behaviour of SHS produced zirconium diboride powder with the addition of C and TiC*. Materials Letters 59 (2005) 3467 – 3470.

[31] S. Baik and P. F. Becher, *Effect of Oxygen Contamination on Densification of TiB$_2$*, J. Am. Ceram. Soc., 70 [8] 527–30 (1987).

[32] F. Monteverde, A. Bellosi, S. Guicciardi, *Processing and properties of zirconium diboride-based composites*. Journal of the European Ceramic Society 22 (2002) 279–288.

[33] F. Monteverde, S. Guicciardi, A. Bellosi, *Advances in microstructure and mechanical properties of zirconium diboride based ceramics*. Materials Science and Engineering A346 (2003) 310-319.